Modules for THz heterodyne array receivers

Huy Duy Do

THÈSE DE DOCTORAT

DE L'UNIVERSITÉ PSL

Préparée à l'Observatoire de Paris

Dans le cadre d'une cotutelle avec Centre national d'études spatiales

Modules pour réseaux de récepteurs hétérodynes THz

Modules for THz heterodyne array receivers

Soutenue par

Huy Duy DO

Le 29 09 2022

Ecole doctorale n° 127

Astronomie et astrophysique d'Île-de-France

Spécialité

Instrumentation pour l'Astronomie

Composition du jury :

Mme. Dominique, BOCKELEE Dr, LESIA	*Présidente*
M.François, PAJOT Dr, IRAP	*Rapporteur*
Mme. Christine, LETROU Prof, Télécom SudParis	*Rapporteuse*
M. Patrick, MOUNAIX Dr, IMS-Université de Bordeaux	*Examinateur*
M. Jérôme, PUECH Dr, CNES	*Membre invité*
Mme. Yan, DELORME Dr, LERMA	*Directrice de thèse*

ACKNOWLEDGEMENTS

This thesis is done with the contribution of a lot of people. My life is so blessed to have the chance to meet, work, or be friends with them.

First and foremost, I would like to express my deepest gratitude to my supervisor, Dr. Yan Delorme, for her continuous support throughout three years. This thesis contains theoretical and experimental parts, both of which seem challenging. But she always stands by me, with her patience and endless support, to help me overcome difficult problems. I have learned a lot since I started working with her. I am really grateful for her mentorship and guidance.

I would like to thank Grégory Gay for his enthusiasm in helping me set up the quasi-optical measurement and for always giving proper instructions in simulations. His experience saves me a lot of time and energy.

It is my great pleasure to have François Pajot and Christine Letrou as reporters on my jury. I also thank Dominique Bockelée, Patrick Mounaix, Jérôme Puech, for accepting my invitations to become a part of the jury.

I would like to thank LERMA colleagues who support my work: Thibaut Vacelet for always being available to help me solder the HEB block; Alexandre Féret for his valuable comments when working with the HEB block; Tarikakan Demirturk for his IT support.

It would be a big mistake if I did not mention technical specialists at Altair Engineering Inc, especially Eddy Jehamy. He is always the person I knocked on once I got the technical problems with FEKO simulation, since the beginning days of my study.

Many thanks to Martina Wiedner for her support, even since I have not started my thesis at l'Observatoire de Paris. She was the person helping me to prepare my presentation for the PhD's competition at ED 127.

I could not forget Maryvonne Gerin and Laurent Pagani for keeping an eye on my works, through the organization of *comité de suivi* at LERMA.

My special thanks to Gérard Beaudin for his assistance during this thesis. I have benefited a lot from his valuable comments and helpful discussions. Thanks again for his warm heart!

I sincerely thank Filipe Aires and Catherine Prigent for their encouragement, which helped me overcome the tough times during my thesis.

I very much appreciate Michèle Bá Trung for her kindness over three years. She not only helps me with the technical part but also gives me precious life advices.

Special thanks to Đinh Thị Lan Anh. She always cheers me up when I feel down and lack inspiration. Thanks so much for always being by my side and supporting me, whatever happens.

This research is cofinanced by CNES (Centre National d'études Spatiales) and LERMA (Laboratoire d'Etudes du Rayonnement et de la Matière en Astrophysique et Atmosphères) at l'Observatoire de Paris-PSL. The thesis is registered in ED127 (Ecole Doctorale Astronomie et Astrophysique d'Ile de France). I would like to thank Jean-Michel Krieg at LERMA for his management works. Many thanks to Jérôme Puech and Christophe Goldstein at CNES for looking after me during this thesis.

Most importantly, I want to give my gratitude to my family. They are always my constant source of energy. This thesis is dedicated to them.

RÉSUMÉ

Les fréquences THz contiennent beaucoup d'informations utiles pour révéler la formation de la galaxie et l'évolution des étoiles. Pour détecter le spectre avec une sensibilité élevée et une très haute résolution, nous devons utiliser un récepteur hétérodyne. Pour les fréquences supérieures à 1 THz, le mélangeur à bolomètre à électrons chauds (HEB) est le meilleur candidat car il a la sensibilité la plus élevée parmi d'autres types de mélangeurs et théoriquement aucune limite de fréquence supérieure. L'une des demandes urgentes pour les futurs télescopes nécessitant des mélangeurs HEB est la construction de réseaux de récepteurs dans le but d'améliorer la cohérence des données acquises et d'augmenter la vitesse de cartographie. Il n'y a actuellement que quelques réseaux de récepteurs avec un petit nombre de pixels fonctionnant au-dessus de 1 THz. Ainsi, cela nécessite encore beaucoup d'investigation.

Cette thèse se concentre sur deux aspects principaux. Le premier consiste à étudier l'élément de distribution de l'oscillateur local (OL) pour le réseau de mélangeurs en utilisant un réseau de phase global. Le deuxième est de caractériser l'impédance en fréquence intermédiaire (FI) du mélangeur HEB dans ses conditions de travail.

Le premier aspect vise à trouver un moyen efficace de diviser un faisceau OL à quatre faisceaux secondaires pour alimenter une matrice de mélangeur à 1,3 THz. J'ai d'abord simulé et mesuré un diviseur à quatre faisceaux, puis analysé ces données et conclu les travaux de conception. La simulation et la mesure montrent un bon accord.

Le deuxième aspect vise à mieux comprendre le mécanisme physique du HEB afin de préparer l'intégration du circuit FI pour la construction du réseau de mélangeurs. Ce travail est réalisé par la combinaison de mesure et de simulation électromagnétique tridimensionnelle du bloc HEB. J'ai extrait

l’impédance FI du mélangeur HEB à différents points de polarisation et différents niveaux de pompage OL à température cryogénique.

Mots-clés : THz, mélangeur HEB, réseau de récepteur hétérodyne, réseau de phase, impédance FI.

ABSTRACT

THz frequencies contain a lot of helpful information to reveal the formation of the galaxy and the evolution of the stars. To detect the spectral with high sensitivity and very high resolution, we need to use a heterodyne receiver. For the frequencies above 1 THz, the hot-electron-bolometer (HEB) mixer is the best candidate since it has the highest sensitivity among other kinds of mixers and theoretically no upper-frequency limit. One of the urgent demands for future telescopes requiring HEB mixers is building array receivers with the aim of improving the consistency of acquired data and increasing the mapping speed. There are currently only a few receiver arrays with a small number of pixels working above 1 THz. Thus, it still requires a lot of investigation.

This thesis focuses on two main aspects. The first is to investigate the local oscillator (LO) distribution element for the receiver array using the global phase grating. The second is to study the intermediate frequency (IF) impedance of the HEB mixer under its working conditions.

The first aspect aims to find an efficient way to divide the one single beam of the LO source to four sub-beams to feed a mixer array at 1.3 THz. I first simulated and measured a four-beam phase grating, then analyzed these data and concluded the design work. The simulation and measurement show a good agreement.

The second aspect aims to better understand the physical mechanism of the HEB and to prepare the integration of the IF circuit for the miniaturization of the current receiver. This work is done by the combination between measurements and three-dimensional electromagnetic simulation of the HEB block. I extracted the IF impedance of the HEB mixer at different bias points and local oscillator pumping levels at cryogenic temperature.

Keywords: THz, HEB mixer, heterodyne array receivers, phase grating, IF impedance.

TABLE OF CONTENTS

ABBREVIATIONS

2D	Two Dimensional
3D	Three Dimensional
AMC	Amplifier-Multiplier Chain
DSB	Double Side Band
DUT	Device Under Test
EM	Electromagnetic
FFT	Fast Fourier Transform
HDPE	High-Density Polyethylene
HEB	Hot-Electron-Bolometer
IF	Intermediate Frequency
iFFT	Inverse Fast Fourier Transform
LNA	Low Noise Amplifier
LO	Local Oscillator
NSGR	Nebosis, Semenov, Gousev, and Renk model
PA	Power Amplifier
QCL	Quantum Cascade Laser
RF	Radio Frequency
S11	Reflection coefficient
SEM	Scanning Electron Microscope
SSB	Single Side Band
VNA	Vector Network Analyzer

Chapter 1. Introduction

1.1 Radio astronomy

For thousands of years, when observing the vast universe, humans always have been obsessed with the question of the universe's origins: how it formed, has grown, and even when it will collapse?

In the beginning, we only rely on our eyes to observe the sky (as shown in Figure 1-1a). Then, humans invented the optical telescope for better observation. The size of the optical telescopes has progressively increased, from the small telescope of Galileo in 1609 (shown in Figure 1-1b) to the giant ground telescope as the Extremely Large Telescope (shown in Figure 1-1c) which is to be inaugurated in Chile in 2027.

(a) (b) (c)

Figure 1-1. a) Modern humans observe a wandering star (Credit picture: https://astronomy.com)

b) Telescope of Galileo (Credit picture: Scala/Art Resource, New York)

c) Rendering image of Extremely Large Telescope in Chile

Even with huge optical telescopes, the observations in the visible band are not enough to satisfy our curiosities and not be able to answer all the

questions. Fortunately, besides the visible range, the astronomical sources (planets, nebulas, galaxies., etc.) also emit different electromagnetic spectra from microwave, millimetre-wave, terahertz (THz), infrared, ultraviolet range, or even gamma-rays. The frequency and wavelength of electromagnetic waves are shown in Figure 1-2.

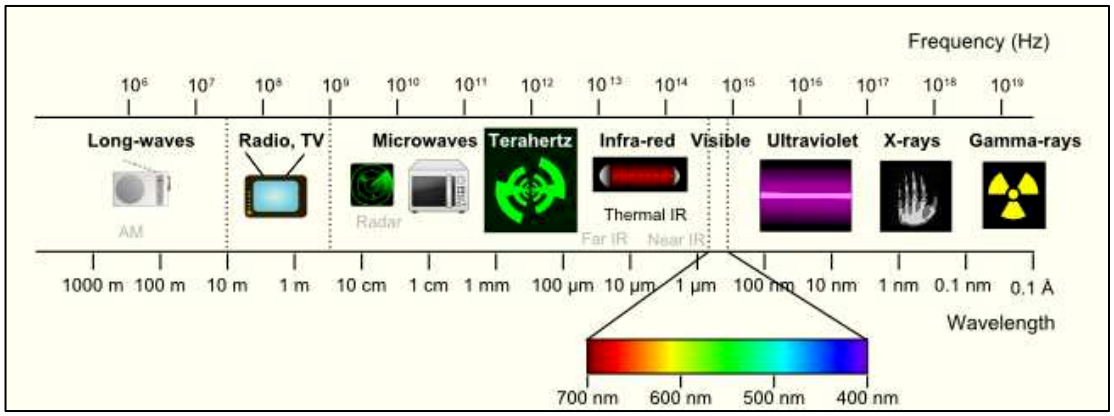

Figure 1-2. Spectral windows (Credit photo: https://terasense.com).

The era of radio astronomy started when the first radio telescope was built in Grote Reber's backyard in 1937. Many ground and space telescopes have been constructed at different frequency ranges, from radio to gamma-rays. For example, in the low frequencies, we have LOFAR interferometer (one of the LOFAR stations is shown in Figure 1-3a) working from 10 MHz to 300 MHz; SKA is underdevelopment and will operate at the frequencies from 70 MHz to 10 GHz. In the mm, submm to THz range, there are ground-based observatories, such as the NOEMA interferometer (shown in Figure 1-3b), and the ALMA interferometer. For the THz-IR, space-borne are used as SOFIA, HERSCHEL (shown in Figure 1-3c), James Webb., etc.

(a)

(b)

(c)

Figure 1-3.

a) One of the LOFAR stations located in Nançay, France (Credit picture: https://www.obs-nancay.fr/)

b) NOEMA interferometer (Credit picture: https://www.iram-institute.org/)

c) Herschel Space Observatory (Credit picture: https://www.esa.int/)

This thesis focuses on the THz band, which covers the electromagnetic waves between 0.3 THz to 3 THz or even more expansive, from 0.1 THz to 10 THz (30 μm to 3 mm), followed by different definitions. It is the radiation lying between the microwave and infrared rays. Almost 50% of the total luminosity and 98% of the photons emitted exist in the THz band since the Big Bang [1]. The cold objects in the universe, such as the dust and gas clouds, emit most of their radiation in this frequency range. Several essential

spectra lines in the THz field can be counted as ionized nitrogen [NII] (1.4 THz), ionized carbon [CII] (1.9 THz), hydrogen deuteride [HD] (2.7 THz), and neutral oxygen [OI] (4.7 THz). These spectrums play an integral role in astronomy and cosmology, which give us helpful information about the beginning of the universe, the formation of the stars, and the evolution of galaxies.

Unfortunately, this frequency range, called the THz gap, lies between two well-developed domains in microwave and infrared light. Still, it is barely explored because of the lack of powerful THz sources and detectors. The THz range also did not give much attention to astronomers in the old days because the water vapour in the atmosphere strongly absorbs it. Thus, to build the telescopes observing THz waves, we need to put them at a very high-altitude place or in space; both are challenges. For the reasons above, it still requires many efforts to explore this frequency region.

1.2 Detection techniques

To detect the THz signal, the detectors in radio telescopes are based on two kinds of detection: direct (incoherent) and heterodyne (coherent or indirect). I will introduce them briefly in this section, focusing more on the THz heterodyne detection.

1.2.1 Direct detection

In the case of direct detection, a DC voltage or a current proportional to the amount of the collected signal is produced by the detector. So, it could not keep the phase information of the signal, but only record the intensity fluctuation. We can use a direct detector to get spectral resolution, but we first need to filter the signals in front of the detector. The spectral resolution, in this

case, is not high (i.e. $\Delta\upsilon/\upsilon \sim 10^{-4}$). One of the advantages of this detector is that its structure is relatively simple and easy to design in a large format array.

1.2.2 Heterodyne detection

To detect the THz signal with high sensitivity and very high spectral resolution (with $\Delta\upsilon/\upsilon \sim 10^{-6}$ to 10^{-8}), it is necessary to use the receiver based on heterodyne detection (coherent detection). A heterodyne detector can detect both amplitude and phase of the input signal.

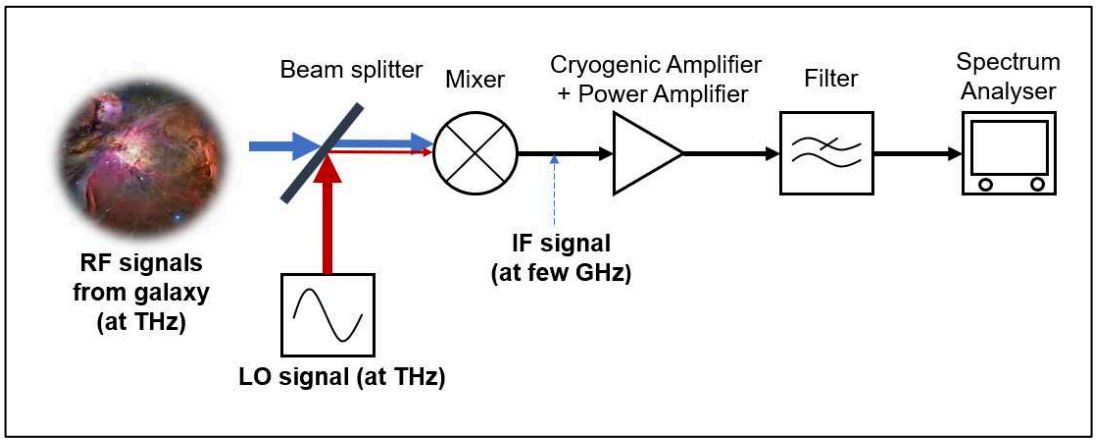

Figure 1-4. Schematic of a THz heterodyne receiver.

As shown in Figure 1-4, in the case of a THz heterodyne receiver, radio frequency (RF) signals collected from the sky are overlaid with the Local Oscillator (LO) signal by a beam splitter. The LO signal is a monochromatic signal which has a frequency close to one of the RF signals. Two signals are combined at the mixer—the heart of the system—to form an intermediate frequency (IF) signal at a few GHz. The IF signal is then amplified by the low noise amplifier (LNA) and Power Amplifier (PA) before being filtered and further analyzed. This mechanism can preserve both the amplitude and phase of the input signal. It also allows processing IF signals easily with available electronic systems. However, heterodyne detector is more complex to manufacture than direct detector.

1.3 THz heterodyne receivers

In this section, I first introduce the essential components of a THz heterodyne receiver, such as the mixer and the local oscillator source. Then, the advantages of the array receiver compared to the single receiver are considered. It will be the motivation for my thesis.

1.3.1 Mixers

There are three essential kinds of mixer used in the THz heterodyne detection: Schottky diode, superconductor-insulator-superconductor (SIS) junction, and hot-electron-bolometer (HEB). They take advantage of the high non-linear current-voltage (I-V) characteristics to mix RF and LO signals.

1.3.1.1 Schottky diode mixer

Schottky diode is a junction formed between a metal and a semiconductor. The non-linear I-V curve is achieved due to the Schottky barrier between the metal and the semiconductor. A Schottky diode can work at room temperature, over the wide frequency range up to several THz. But it requires a high LO power (~ milliwatt) and has lower sensitivity compared to other kinds of mixers (e.g. SIS, HEB).

1.3.1.2 Superconductor-Insulator-Superconductor mixer

SIS junction contains two superconductors, with a very thin layer of oxide insulator (at the order of nm) inserted between them. The non-linear I-V characteristic of the SIS mixer is created by photon-assisted quasiparticle tunneling effects, where quasiparticles cross the SIS barrier [2][3]. SIS junction is the most sensitive mixer below 1 THz. It also requires a low LO power (< microwatts). However, the critical problem with SIS junction is that its

performance is degraded above the gap frequency v_g of the material (i.e. around 700 GHz for Niobium), with

$$v_g = \frac{E_g}{h} \qquad \textit{Equation 1}$$

where E_g is the superconductor energy gap, and h is the Planck's constant.

SIS must work below the critical temperature (around several K). Another problem with SIS junction is that it contains an intrinsic capacitance C. Therefore, we need to add a low-loss tuning circuit to avoid the capacitive shunting of the input signal. At the higher frequency above 1 THz, the tuning circuit's losses become considerable and reduce the mixer's performance.

1.3.1.3 HEB mixer

HEB is just a very thin superconducting microbridge at a few nm made from superconducting materials (e.g. Nb, NbN, NbTiN). The non-linear I-V characteristic is based on the resistivity of this thin film, which depends strongly on temperature close to the critical temperature of the used superconductors (around a few K). HEB mixer has high sensitivity and requires very low LO power (~ nanowatts). Moreover, it does not face the problem of the gap frequency as an SIS mixer. As a result, HEB has theoretically no upper-frequency limit. For sensitive application requirements, SIS mixers are typically used from 0.2 to 1 THz, and HEB covers the range from 1 to 5 THz [4]. However, the disadvantage of an HEB compared to a Schottky diode mixer is it still requires a low temperature to work on. The detail about the HEB mixer used in our work will be presented in Chapter IV.

1.3.2 Local Oscillator sources

Along with the mixer, the LO is also a main component in a THz heterodyne receiver. It produces a monochromatic signal, which is then mixed with the RF signal to generate the IF signal. The most challenging is to find an efficient LO which has enough power to pump mixers at the THz frequency.

There are a lot of LO sources, such as FIR gas laser, quantum cascade laser, backward wave oscillator, and amplifier multiplier chain. Here we introduce two common kinds of LO: amplifier-multiplier chain and quantum cascade laser.

1.3.2.1 Amplifier-multiplier chain

Amplifier-multiplier chain (AMC) is widely used for applications under 3 THz. An input signal at several tens of GHz is amplified and multiplied across the chain (which combines several amplifiers and multipliers) to achieve the desired THz frequency at the output. The output signal is radiated through the horn, usually with a Gaussian beam form. The power reduces after passing each multiplier stage. The higher the frequency is, the lower the power of the output signal we can obtain. The output power can reduce from several tens of μW at 1 THz to a few μW at frequencies above 2 THz. The output frequency can be tuned around 10 % to 20 %, allowing it to work in multiple frequencies.

1.3.2.2 Quantum cascade laser

Quantum cascade laser (QCL) is a kind of semiconductor laser. First introduced in 1994 [5], QCL gains significant leaps and matures enough to work in the wide frequency ranges from mid to far-infrared ranges. It is used for frequencies above 2 THz, where it can generate several mW of the output power. But one of the disadvantages of the QCL is it primarily works at cryogenic temperature (at around 10 K – 70 K), although there are several efforts to make it work at room temperature [6]. It is unstable. Its output beam is not really following the Gaussian distribution, so it is not easy to match its beam profile with the mixer input. The working frequency of QCL is difficult to tune. Thus, QCL can only work at a specific frequency. The size of QCL is small (at the order of mm). Therefore, it is suitable to integrate into a heterodyne receiver to form a compact block.

1.3.3 THz heterodyne receiver arrays

1.3.3.1 THz heterodyne receiver arrays

THz heterodyne receiver arrays have recently become more popular because they have more advantages than the single-pixel receiver [7]. With receiver array, we can observe several regions of the sky simultaneously, increasing the consistency of the mapping region, and boosting the mapping speed.

Here are some examples of THz heterodyne receiver arrays [7] which have been or will be developed as SuperCAM (8 x 8 pixels, working at 345 GHz using SIS mixers) [8], CHAMP+ (4 x 4 pixels, working at 660-850 GHz using SIS mixers) [9], upGREAT (2 x 7 pixels, working at 1830 – 2070 GHz using HEB mixers) [10], [11], STO-2 (2 x 2 pixels, working at 1.46 THz and 1.9 THz using HEB mixers) [12], GUSTO (8-pixel, working at 1.4, 1.9 and 4.7 THz using HEB mixers) [13].

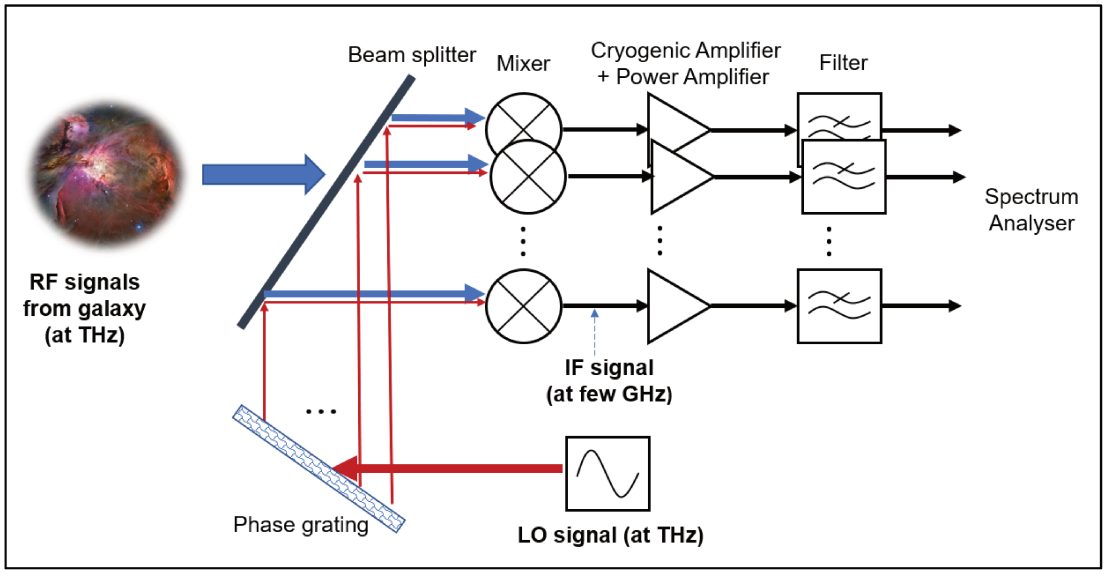

Figure 1-5. Schematic of a THz heterodyne receiver array

Among projects operating at frequencies above 1 THz, a few are arrays. Each array just contains a small number of pixels. The reason is that the complexity of a heterodyne receiver array increases along with the pixel

number. As mentioned in section 1.2 and Figure 1-5, the heterodyne receiver is more complex than the direct one because it needs to couple LO and RF signals into mixer to generate IF signal; and requires IF chain to amplify, filter, and analyze this IF signal. Several factors should be considered and more efforts are needed when building a THz receiver array. The most important is to know how to distribute the LO power to each mixer. It's also essential to be able to extract the IF output power in an optimal way in order to build multiple IF chains with minimum losses and in the most compact way.

1.3.3.2 Local Oscillator distribution

Each mixer in a multi-pixel receiver must be fed by LO beam. Using one LO source per mixer pixel is not economical, and the receiver system will become cumbersome. One solution is to divide the beam of a single LO source into multiple beams to feed the mixer pixels. We can do it by using a waveguide splitter or a phase grating.

The waveguide is challenging to manufacture at frequencies above 1 THz. It requires a considerable effort to ensure a good accuracy in mechanical fabrication. At higher frequencies, the losses of the waveguide are worse.

The phase grating is easier to fabricate compared to the waveguide. We also can use it for a wide range of frequencies. The working principle of the phase grating is based on the variation of its surface to modify the spatial phases of the incident beam, leading to creating the output beams by destructive or constructive interference. Phase grating will be further studied in Chapter 3.

1.4 Objective of this thesis

While receiver arrays have more advantages than single receivers, it is still facing difficult technical problems. The work of my thesis is aimed to investigate the aspects that can play a key role in building future receiver arrays.

My work concerns two main aspects. The first is to study the LO's beam divider, or more specific, the global phase grating. The second is to investigate the IF characteristics of the HEB mixer under its working condition.

My thesis will be organized as follows:

Chapter 2 concentrates on the working principle and theoretical characteristics of the HEB mixer.

Chapter 3 focuses on the simulation and measurement of a quasi-optical coupling system at 1.3 THz, where the main component is a beam divider. This beam divider is aimed to divide one single LO source into four sub-beams to feed a four-pixel receiver array. I simulated the 2 x 2 beam divider designed previously in our laboratory. Then, I took part in the characterization of this phase grating. Finally, I compared the measured and simulated results before giving the conclusion. Besides, I improved the code so up to sixteen output beams can be generated from one single input beam.

Chapter 4 is dedicated to investigating the IF characteristics of the HEB mixer. It is an essential parameter to deeply understand the working principle of the HEB mixer. It is also a crucial step leading toward integrating the HEB mixer and the matching circuit into a compact block later, making us closer to building a single compact array receiver. In this chapter, I characterized the impedance of the HEB mixer at cryogenic temperature by combining the measurements and 3D EM simulation.

In chapter 5, I conclude my works during this thesis. Several ideas for future works are proposed.

Chapter 2. Superconducting HEB mixer

As mentioned in Chapter 1, the impedance of a hot-electron-bolometer (HEB) under working conditions will be extracted for building the matching circuit between HEB mixer and cryogenic LNA. Before measuring and extracting the HEB's impedance, understanding the working principle and physical mechanism of an HEB is very important.

In this chapter, I first present the working principle of HEB mixer. The HEB—a bolometer itself— will follow the working mechanism of a bolometer. Thus, the mixing principle of the bolometer will be described. Then, two HEB's physical models are investigated: NSGR (proposed by Nebosis, Semenov, Gousev, and Renk) and hot spot models. More attention is drawn to the NSGR model because it gives us the frequency-dependent IF impedance of HEB mixer under working conditions. Besides, the noise of the mixer is also studied in this chapter.

2.1 Bolometer

A bolometer is a sensitive device able to detect electromagnetic radiations. It is made from a material whose resistance varies with the temperature. The absorbed radiation heats the bolometer, and a thermometer records the temperature change. The bolometer was invented in 1878 by the American scientist Samuel Pierpont Langley. It has recently been widely used in radio telescopes (e.g. Herschel, Planck and SOFIA) to detect the RF signal from THz to far-infrared frequency.

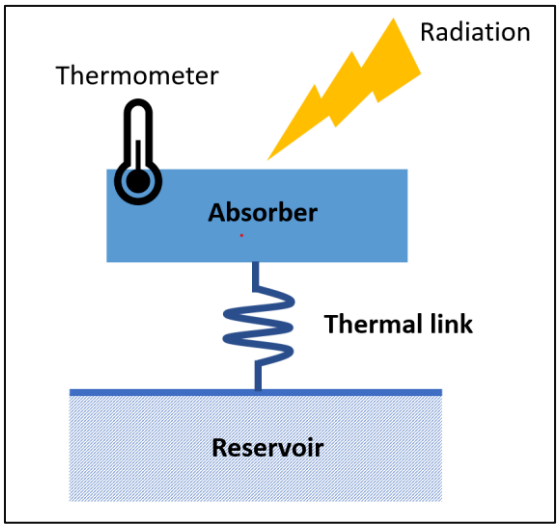

Figure 2-1. Thermal block diagram of a bolometer

As shown in Figure 2-1, a bolometer generally contains three parts: the absorber, the thermal link, and the reservoir. The absorber is connected to a thermal reservoir by a weak thermal link. The changing of absorber temperature is detected by the thermometer attached to the absorber.

2.2 Mixing in a bolometer

Figure 1-4 shows a single heterodyne receiver working in the THz frequency range. The local oscillator (LO) generates a monochromatic signal (f_{LO}), which has a frequency close to the RF signal (f_{RF}). The voltage of the RF signal is $V_{RF}cos(\omega_{RF}t)$. For the LO signal, it is $V_{LO}cos(\omega_{LO}t)$.
At the bolometer, two signals are mixed together. The voltage at the bolometer is

$$V(t) = V_{LO}cos(\omega_{LO}t) + V_{RF}cos(\omega_{RF}t) \qquad \textit{Equation 2}$$

If the bolometer's resistance is R_0, the power that is dissipated by the bolometer over time will be

$$P(t) = \frac{V(t)^2}{R_0} = \frac{[V_{LO}cos(\omega_{LO}t) + V_{RF}cos(\omega_{RF}t)]^2}{R_0} \qquad \textit{Equation 3}$$

$$= \frac{1}{R_0}\left[\frac{V_{LO}^2}{2} + \frac{V_{RF}^2}{2} + \frac{V_{LO}^2 cos(2\omega_{LO}t)}{2} + \frac{V_{RF}^2 cos(2\omega_{RF}t)}{2} + V_{LO}V_{RF}cos[(\omega_{RF} + \omega_{LO})t] + V_{LO}V_{RF}cos[(\omega_{RF} - \omega_{LO})t]\right]$$

In fact, we could suppress the frequency terms of $2\omega_{\mathrm{LO}}$, $2\omega_{\mathrm{RF}}$, and $(\omega_{\mathrm{RF}} + \omega_{\mathrm{LO}})$ because these frequencies are too high for the device to follow. In addition, the RF signal power is too small compared to the LO power, so the term $\frac{V_{RF}^2}{2}$ could be ignored. We have

$$P(t) = \frac{1}{R_0}\left[\frac{V_{LO}^2}{2} + V_{LO}V_{RF}cos[(\omega_{RF} - \omega_{LO})t]\right] \qquad \textit{Equation 4}$$

It should be noted that the average absorbed power of the LO signal is $P_{LO} = \frac{V_{LO}^2}{2R_0}$ and the one of the RF signal is $P_{RF} = \frac{V_{RF}^2}{2R_0}$. In the end, the power that the detector can detect is

$$P(t) = P_{LO} + \sqrt{P_{LO}P_{RF}}cos(\omega_{IF}t) \qquad \textit{Equation 5}$$

As we see, two signals are mixed at the mixer (which has a non-linear current-voltage characteristic) to create the IF signal with $f_{IF} = |f_{RF} - f_{LO}|$. The f_{IF} can be produced in two ways, using an RF signal with $f_{RF} = f_{LO} + f_{IF}$ — which is called the upper side band (USB), or $f_{RF} = f_{LO} - f_{IF}$ — which is called the lower side band (LSB). The receiver system that accepts both side band frequencies is called double side band (DSB) receiver.

When studying only one side band, the noise from another side band can reduce the signal-to-noise ratio of the heterodyne detector. The solution is to put a band pass filter at the input of the receiver to only keep the frequency from one sideband and get rid of the frequency from another side band; or use a sideband-separating configuration, where 90 ° hybrids are used at the input of the RF signal and the output of the IF signal.

A low pass filter is often added between the IF amplifier and the spectrum analyzer to only allow the IF signal to pass through and stop the higher frequency harmonics.

2.3 Working principle of a HEB mixer

2.3.1 Heating process in superconducting HEB mixers

Hot-electron-bolometer (HEB), as its name, is a kind of bolometer. An illustration of a superconducting HEB mixer is shown in Figure 2-2 [14].

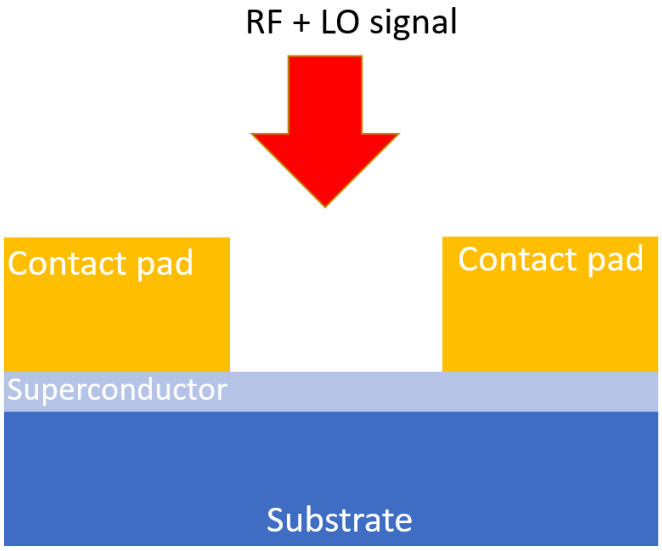

Figure 2-2. Side view of a superconducting HEB mixer

An HEB mixer includes a superconducting thin film (e.g. Nb, NbN, or MgB_2) deposited on a substrate (e.g. silicon, sapphire). In our case, the film is made from NbN, and the substrate is silicon. The film's thickness is just about several nm. Two ends of the thin film are covered by two contact pads made from gold. They are two electrodes of the antenna to couple RF and LO to the thin film.

HEB needs to be cooled down to the superconducting state to operate as a mixer. When superconductors are cooled to the temperatures under the critical temperature T_c, their electrical resistor will become zero. This phenomenon is called superconductivity. For most materials, the T_c is between absolute zero and 10 K. For instance, the T_c of Nb is 9.25 K, of Pb is 7.2 K. We also use the term cryogenic temperature when working with HEB. In terms of the Kelvin scale, the cryogenic region is often below approximately 120 K (- 153 °C).

When working as a mixer, the bolometer is cooled down to the temperature below its critical temperature T_c. It should be coupled with a LO signal and DC biased. Due to the LO and DC effect, electrons in the bridge are heated up to a temperature close to T_c. The hot spot is then formed by the absorption of the LO and DC. At these operating points, the resistance of the bolometer is very sensitive. Every small power change of the radiation (by absorbing RF signal) can change the resistivity of the device and be detected by the changing of the I-V curve. This superconducting thin film plays the role of both absorber and thermometer of the bolometer shown in Figure 2-1.

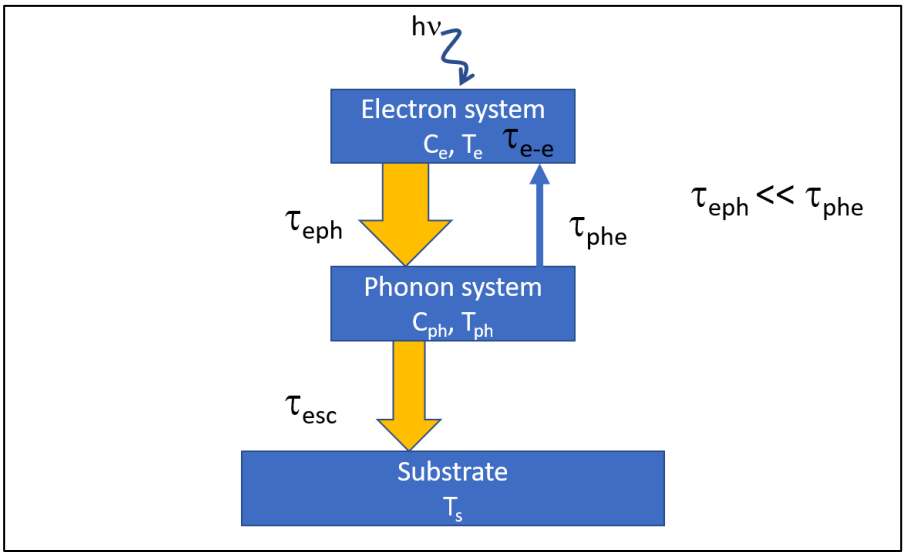

Figure 2-3. Schematic showing the thermal energy transfer in an HEB [14].

The thermal model of hot-electrons is illustrated in Figure 2-3, according to the study in [14]. Two separated subsystems can be considered to exist in the thin film: electrons with the temperature T_e and heat capacity C_e; phonons with the temperature T_{ph} and heat capacity C_{ph}. In the substrate, the phonon subsystem has the temperature T_s. As denoted in Figure 2-3, τ_{e-e} is electron-electron interaction time, τ_{eph} is electron-phonon interaction time, τ_{phe} is phonon-electron interaction time, τ_{esc} is the escaped time of the phonon from superconductor into the substrate.

At room temperature, the density of the phonons is high. Thus, electrons and phonons can interact efficiently in a short time, as shown by the short τ_{eph}. So, R_{eph} is small. When the mixer is cooled down to the temperature lower than the critical temperature T_c, the phonon density in the microbridge quickly decreases. This leads to a longer interaction time between electron and phonon, referring to the more considerable thermal resistance R_{eph}. In this case, the electron's temperature is higher than the phonon's temperature, which leads to the hot-electron effect.

Below the superconducting transition temperature, electrons do not exist freely but are coupled to form Copper pairs. Radiations with energy above the gap energy can break the Copper pairs into quasi-particles. The energy larger than the energy gap excites these quasi-particles to create the hot electrons. Because the electron-electron interaction time is shorter than the required time for the energy to leave the bridge, thus the energy is quickly distributed to other electrons, creating many hot electrons [14]-[16].

2.3.2 Resistance versus temperature and current versus voltage curves of an ideal superconducting HEB mixer

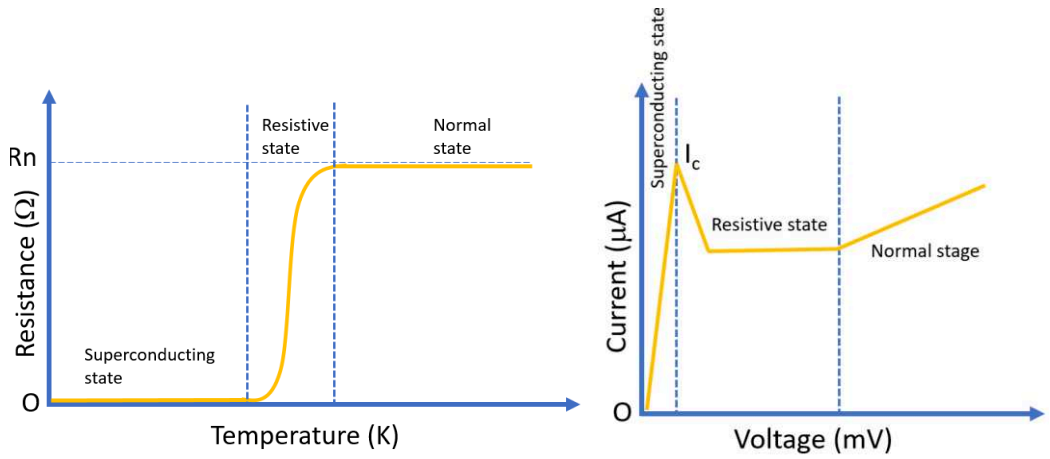

(a) (b)

Figure 2-4. a) Resistance versus temperature (R-T) curve of an ideal superconducting HEB mixer. b) Current versus voltage (I-V) curves of an ideal superconducting HEB mixer [16], [17].

Three states of HEB resistance versus temperature are shown in Figure 2-4a [16], [17]. First, the HEB is cooled down to the superconducting state. Then, it is driven to the resistive state—the state between the superconducting state and normal state—usually by the DC bias. It is also the state the superconducting HEB mixer operates, where the HEB's resistance depends strongly on the change in the temperature. When the DC increases to a threshold, the HEB will become a normal resistor with a fixed value.

The current versus voltage (I-V) curve of an HEB following three states is shown in Figure 2-4b [16], [17]. At the superconducting state, because the HEB's resistor is zero, a slight change of the voltage leads to a high current rise until its maximum value I_c. Then, the current decreases since the microbridge absorbs the DC power, generating an unstable region of the I-V curve. Increasing the bias voltage makes the mixer gradually become a resistor with a constant value at the normal state.

2.3.3 Cooling mechanism in HEB mixers

There are two ways to cool down hot electrons in the film: phonon-cooled, and diffusion-cooled. Phonon-cooled means that the heat is dissipated by the phonons via the substrate. Diffusion-cooled implies that the hot electrons can dissipate the heat throughout the end of the microbridge via the contact pads [14][15]. When the microbridge is short enough, the diffusion-cooled is dominated. Meanwhile, in the case of the very thin (e.g. 3~5 nm thickness of an NbN film) and relatively long microbridge (e.g. 200 nm length of an NbN film), the phonon-cooled plays the dominant role.

This study uses a mixer that follows the phonon-cooled mechanism. In this concept, the microbridge's hot electrons interact with phonons, scattering the heat to the substrate. The formulas defining the thermal time constants will be presented later in this chapter.

The diffusion-cooled concept was first introduced in 1993 [18]. To be a diffusion-cooled bolometer, the device length L of the HEB should be smaller than the thermal diffusion length $L_{th} = \sqrt{D\tau_{eph}}$, with D the electron diffusion constant. The thermal time constant then depends on the length of the microbridge L_b and the electron diffusion constant D [19], which is given by

$$\tau_D = \frac{L_b^2}{\pi^2 D} \qquad \textit{Equation 6}$$

When the length of the bridge increases, we need to consider phonon contribution to the electron relaxation [19].

Although the diffusion-cooled mixer shows a lower noise temperature and requires less LO power, it does not have good electrical and mechanical stability. These make it challenging to evaluate the performance of the mixer. Thus, the current trend is more focusing on the phonon-cooled mixer [15], [18].

2.4 Models of superconducting HEB mixers

The physical mechanism of an HEB mixer has been investigated and explained by several models. This thesis refers to two models: the NSGR model [20] and the hot-spot model [21]. In the NSGR model, the HEB is considered as a lumped component. The temperature distribution of the mixer along the microbridge is uniform. The same power amount of RF (LO) and DC signal will make an equal change in the resistance of the bolometer. In other words, as long as the total absorbed power is kept the same, the electron temperature and resistance of the HEB device are maintained, and the absorbed power of LO and DC are exchangeable. The bolometer is considered as a variable resistor since the value of the resistor changes based on the amount of the absorbed power. At frequencies lower than the quasi-particle band gap, this model tends to work well in estimating the RF power absorbed by the bolometer. It also shows an acceptable prediction regarding the mixer conversion gain versus IF frequency and equivalent noise temperature when the HEB mixer works close to the optimal points.

However, the lumped model could not precisely predict the amount of RF power absorbed by the bolometer at higher frequencies (above the quasi-particle bandgap). At these frequencies, although the RF power is still absorbed

uniformly by the bolometer's entire microbridge, the DC power can only be absorbed in the bolometer region called the hot spot. The hot-spot model supposes that there is a hot spot formed at the center of the microbridge thanks to the combination of the LO signal and DC bias. The hot electron temperature varies along the microbridge; the hot spot is the zone with electron temperatures higher than the critical temperature of the superconductor material. When an RF signal illuminates the mixer (with the frequency slightly different from the LO signal), it will adjust the length of the hot spot in the microbridge, which then changes the resistivity of the bolometer. In the hot-spot model, there are separated heating capacities for RF and DC, instead of considering them as the same self-heating coefficient C in the lumped component.

In this chapter, I will introduce both of them. However, hot-spot model does not provide a closed-form expression of impedance Z [22], so we use the lumped model to calculate the impedance of HEB.

2.4.1 NSGR model

In the beginning, the lumped model was applied to explain the conversion loss and noise factor of the bulk InSb mixer, which has small bandwidth (< 100 MHz) [23]. A previous study [24] is based on the lumped model to calculate several parameters of the mixer made from the Niobium films and $YBa_2Cu_3O_{7-\sigma}$: impedance of the mixer at the intermediate frequency, noise temperature, conversion efficiency, fluctuation sensitivity, etc. The Standard model was developed in [17]. This model uses only a single time constant τ_θ (electron temperature relaxation time) to express the frequency-dependent IF impedance of an HEB made from NbN. Its expanded version is the NSGR model [20]—which uses three-time constants τ_1, τ_2, τ_3—to look in detail at the physical mechanism involved in the energy relaxation of the NbN HEB. So, this thesis will use the NSGR model to fit the measured impedance of the NbN HEB mixer under working conditions. The theory of the NSGR

model, including the prediction of the conversion gain, noise temperature, and especially the impedance [20], [22], [25], [26], will be introduced in the following section.

2.4.1.1 IF impedance of HEB mixer at operating points

As discussed in section 2.3.1, the film of HEB contains electron and phonon subsystem, while the substrate includes the phonon subsystem [20]. The energy, from the DC bias or RF (LO) radiation, is absorbed by the electron in the microbridge. This energy is transferred to phonon via electron-phonon interaction (τ_{eph}) and then the substrate by phonons escaped from the microbridge. The formulas describing the working principle of the NSGR model can be found in [20], [25], [26]. Here I briefly introduce these formulas.

The energy flow through the whole linear system ($|T_e - T_0| \ll T_0$) is described by the heat balance equations

$$\begin{cases} c_e \dfrac{\partial T_e}{\partial \mathrm{T}} = P_{dc} + \alpha P_{lo} e^{i\omega t} - c_e \dfrac{T_e - T_{ph}}{\tau_{eph}} \\ c_{ph} \dfrac{\partial T_{ph}}{\partial \mathrm{t}} = c_e \dfrac{T_e - T_{ph}}{\tau_{eph}} - c_p \dfrac{T_{ph} - T_0}{\tau_{esc}} \end{cases} \qquad \textit{Equation 7}$$

where c_e is the temperature dependent electron heat capacity; c_{ph} is the temperature dependent phonon heat capacity; α is the optical coupling coefficient; T_e, T_{ph}, and T_0 are respectively the electron, phonon, and substrate temperature. It should be noted that the energy transfer through the contact pads is neglected. The impedance of the mixer is given by

$$Z = \frac{dU}{dI} = \frac{d}{dI}[I.R(I,T_e)] = R(I,Te) + I\frac{\partial R}{\partial I} + I\frac{\partial R}{\partial T_e}\frac{\partial T_e}{\partial I} \qquad \textit{Equation 8}$$

where T_c is the critical temperature of the superconducting material. Based on the isothermal voltage-current characteristic in [27], the film resistance is modeled as

$$R(I,T_e) \approx \frac{R_n(T_e)}{2}\left((1 + \zeta(T_e) - \frac{[1-\zeta(T_e)]^3}{[1 + I/I_0 - \zeta(T_e)]^2}\right) \qquad \textit{Equation 9}$$

with

$$\zeta(T_e) = \left(1 + \exp\left(4\frac{T_c - T_e}{\Delta T_c}\right)\right)^{-1} \quad \textit{Equation 10}$$

The frequency-dependent HEB output impedance, Z_ω, can be calculated by assuming that a slight fluctuation of the current $dI = \delta I exp(j\omega t)$ can change the electron temperature $dT_e = \delta T_e \exp[j(\omega t + \varphi_1)]$, which leads to the change in the phonon temperature $dT_{ph} = \delta T_{ph} \exp[j(\omega t + \varphi_2)]$.

Substitute $dI, dT_e,$ and dT_{ph} to the heat balanced equations for the linear system in Equation 7, we have the frequency-dependent HEB output impedance:

$$Z(\omega) = R_0 \frac{\psi(\omega) + C}{\psi(\omega) - C} \quad \textit{Equation 11}$$

where R_0=V_0/I_0 is the DC resistance at the operating point of the mixer; C is the self-heating parameter; $\psi(\omega)$ represents the time-dependent modulation of the electron temperature, with ω the IF radial frequency.

The self-heating parameter C is given by

$$C = \frac{I^2}{V}\frac{\partial R}{\partial T_e}\left(\frac{\tau_{eph}}{c_e} + \frac{\tau_{esc}}{c_{ph}}\right) \quad \textit{Equation 12}$$

The function $\psi(\omega)$ can be described as [27]

$$\psi(\omega) = \frac{(1 + i\omega\tau_1)(1 + i\omega\tau_2)}{1 + i\omega\tau_3} \quad \textit{Equation 13}$$

As we can see, $\psi(\omega)$ depends on three time constants τ_1, τ_2, τ_3.

The value of τ_1, τ_2, and τ_3 can be calculated based on

$$\tau_2^{-1}, \tau_1^{-1} = \frac{\Omega}{2}\left(1 \pm \sqrt{1 - \frac{4\tau_{eph}^{-1}\tau_{esc}^{-1}}{\Omega^2}}\right) \quad \textit{Equation 14}$$

$$\tau_3^{-1} = \frac{C_e}{C_{ph}}\tau_{eph}^{-1} + \tau_{esc}^{-1} \qquad \textit{Equation 15}$$

with $\Omega = \left(1 + \frac{C_e}{C_{ph}}\right)\tau_{eph}^{-1} + \tau_{esc}^{-1}$.

The electron-phonon interaction time τ_{eph} is calculated based on the empirical relation [28]

$$\tau_{eph} = 500T_e^{-1.6} \approx 500T^{-1.6} \qquad \textit{Equation 16}$$

The same empirical relation is also applied to the heat transfer rate from phonons in the films to the phonons in the substrate. The phonon escape time τ_{esc} is calculated as

$$\tau_{esc} = 10.5d \ \text{(ps/nm)} \qquad \textit{Equation 17}$$

where d is the thickness of the NbN film, which is usually several nm.

The ratio of the electron to phonon heat capacity in NbN is given by formulas in the paper [28]. In case the electron temperature is approximately equal to the phonon temperature, we can deduce it to

$$\frac{C_e}{C_{ph}} = 18.77T_e/T_{ph}^3 \approx 18.77T^{-2} \qquad \textit{Equation 18}$$

The relationships between the electron temperatures and the time constants are shown in Figure 2-5, following Equation 14-Equation 18.

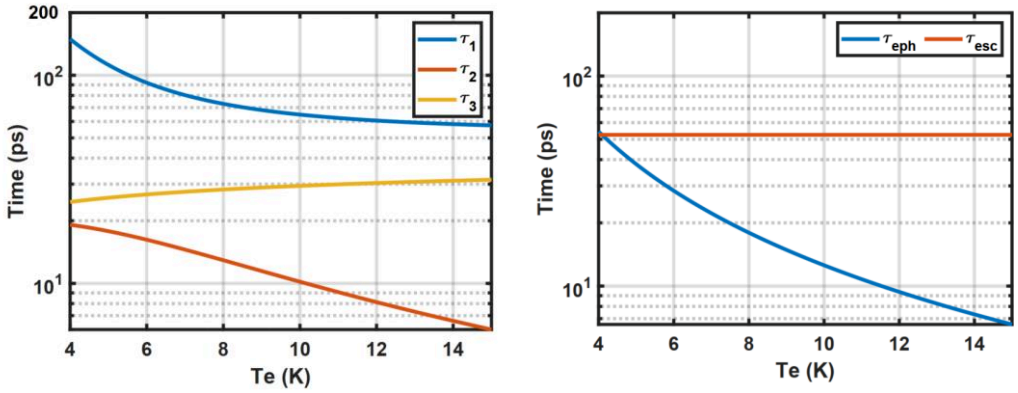

(a) (b)

Figure 2-5. Relationship between the electron temperature and the time constants. The thickness of the NbN superconductor thin film is considered as 5 nm. a) Time constant τ_1, τ_2, τ_3 calculated from Equation 14-Equation 18 b) τ_{eph} and τ_{esc} calculated from Equation 17-Equation 18

The theoretical IF impedance deduced from the Equation 11-Equation 18**,** with a 5 nm thick NbN film at the critical temperature of 8.5 K [16], under different bias voltage and LO pump levels (taken from [29]) is shown in Figure 2-6 to Figure 2-8. The calculated impedances (real and imaginary parts) change very quickly depending on the frequency range from 0 – 2 GHz. After that, the real parts gradually reduce while the imaginary parts gradually increase.

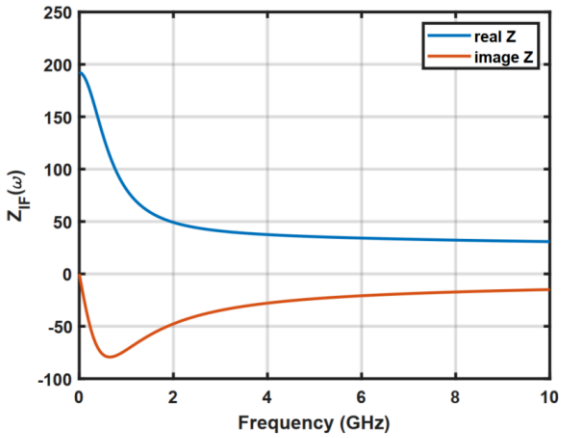

Figure 2-6. IF impedance at an under pumped LO level with DC bias = 1 mV

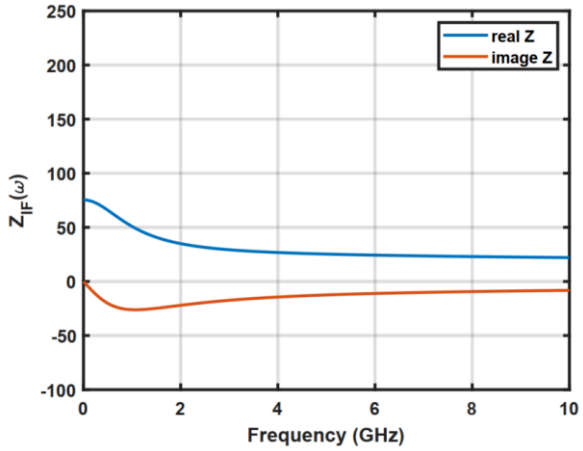

Figure 2-7. IF impedance at an optimal pumping LO level with DC bias = 0.5 mV

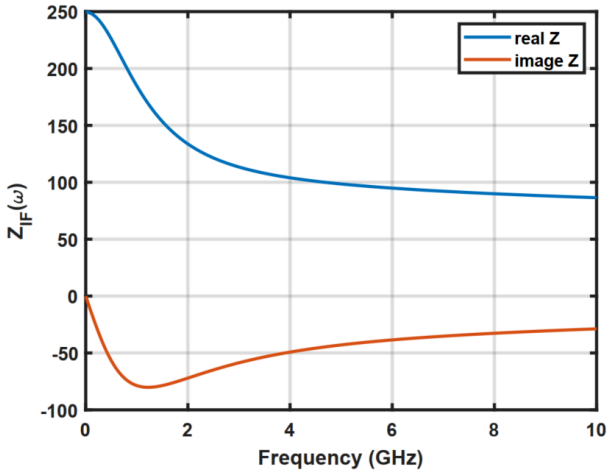

Figure 2-8. IF impedance at an over pumped LO with DC bias = 0.5 mV

2.4.1.2 Conversion gain of mixer

The conversion gain of a mixer is defined as the ratio between the output power (at IF frequency) over the input power (at RF frequency). To derive the conversion gain of the mixer, first, we need to obtain the responsivity of the HEB. The responsivity describes the change in voltage across HEB caused by the power absorbed by the HEB.

Let's consider equivalent impedance Z_l of a circuit (load) connected to the mixer output. The electro-thermal feedback between the mixer and the load is considered. So, the frequency-dependent responsivity, according to [20], [25], is calculated as

$$S(\omega) = \frac{dV_l}{dP} = \frac{\alpha}{\chi . I} \frac{Z_l}{R_0 + Z_l} \frac{C}{\left(\psi(\omega) + \Gamma_{if} C\right)} \qquad \textit{Equation 19}$$

with

$$\Gamma_{if} = \frac{R_0 - Z_l}{R_0 + Z_l} \qquad \textit{Equation 20}$$

where α is the RF coupling factor; I is the signal current through the load (and HEB device). Equation 19 refers to the lumped element model, so we need to modify the NSGR model to be appropriate to the LO and DC power induced temperature profile in the NbN microbridge, in combination with the hot-spot model. χ , as mentioned in [30], is the power exchange function which has the value changing based on the hot-spot length. In the high bias power, the hot-spot length is considered as the length of the bolometer, χ approximately equal to 1. At the low DC bias and low LO power, the size of the hot spot is reduced, χ can be up to 3.

The complex conversion gain of the mixer is

$$\eta(\omega) = \frac{2S(\omega)^2}{Z_l} P_{lo} \qquad \textit{Equation 21}$$

where P_{lo} is the LO power absorbed by the HEB mixer, and is estimated by the isothermal technique [31].

Substitute Equation 19 to Equation 21, with the assumption that all the signal current that goes through the device is the DC bias current with $P_{dc} = R_0 I^2$, the magnitude of the conversion gain is

$$\eta(\omega) = \frac{2\alpha^2 P_{lo}}{\chi^2 P_{dc}} \left| \frac{R_0 Z_l}{(R_0+Z_l)^2} \frac{C^2}{\left[\psi(\omega)+\Gamma_{if} C\right]^2} \right| \qquad \textit{Equation 22}$$

2.4.2 Hot-spot model

Hot-spot model has been developed in recent years because it can describe and predict more accurately the mixing performance of HEB mixer. Here we present the one-dimensional hot-spot model in the case of the substrate-based HEB (or high thickness of the substrate). The membrane-based HEB will not be studied here because it is not the kind of HEB we use in this work.

As shown in Figure 2-2, an HEB mixer has a thin film staying between the substrate and contact pads. The superimposed DC and LO power heats the thin film. A hot spot will be formed at the centre of the superconducting thin film, which is confined by the substrate and two contact pads. In fact, the thin film parts under the contact pads still keep superconducting properties because it is cooled down by the metal contacts. The overlapping of a small RF signal (which has a frequency slightly different from the LO signal) will modulate the dissipated power, changes the hot-spot length, and, consequently, changes the device's resistance. The mixing process of HEB is provided by the oscillation of the hot-spot length at intermediate frequency [21].

Let us consider a heat flow process of the electron and phonon subsystem in the small segment of the microbridge strip, as shown in Figure 2-9. $P_{heating}$ is the total heating power, λ_e the electron thermal conductance, T_e

the electron temperature, λ_p the phonon thermal conductance, T_p the phonon temperature, $P_{e\to p}$ is the power transferred from electrons to phonons, $P_{p\to e}$ is the power transfer from phonons to electrons, $P_{p\to s}$ is the power transferred from phonons to substrate.

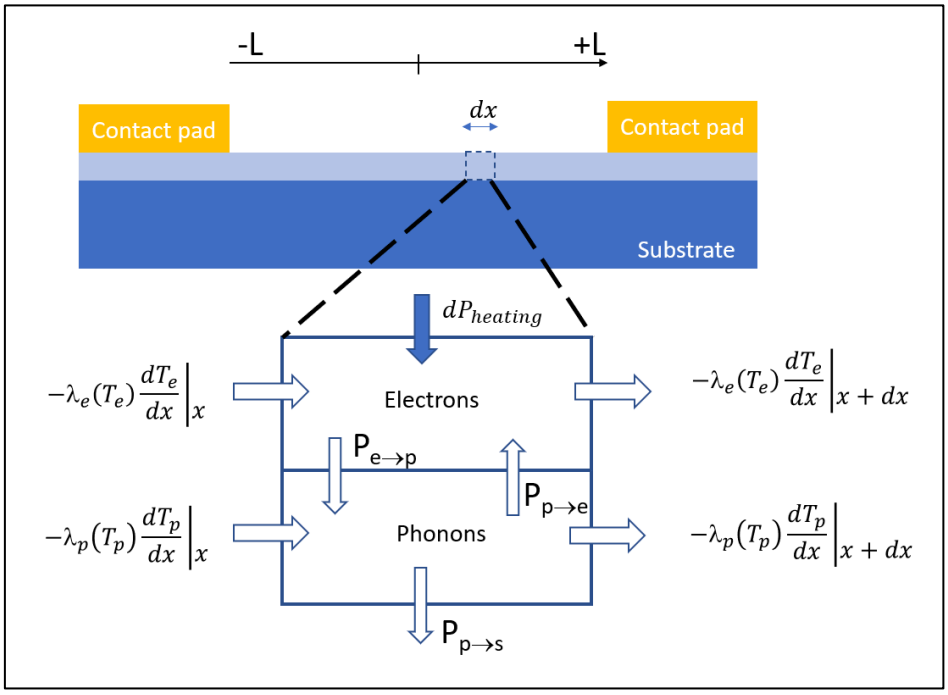

Figure 2-9. Heat flow of electrons and phonons in a small segment with the length dx of a bolometer

The thermal conduction of phonons is neglected because it is small compared to the loss caused by the phonon's escape to the substrate. In the steady state, the electron temperature does not vary in time. According to Figure 2-9, the simplified heat balance equations in the steady state are

$$\begin{cases} -\frac{d}{dx}\left(\lambda_e \frac{dT_e}{dx}\right) + P_{e\to p} - P_{p\to e} = P_{heating} \\ P_{p\to s} = P_{e\to p} - P_{p\to e} \end{cases} \qquad \textit{Equation 23}$$

$P_{heating}$, which includes the heating due to average RF power and bias current, is described by

$$P_{heating} = \frac{P_{LO} + P_S}{2L} + \frac{I_0^2 \rho(T_e)}{S} \qquad \textit{Equation 24}$$

where I_0 is the bias current; 2L is the length of the bolometer strip; S is the cross-section area of dx; $\rho(T_e)$ is the local resistivity, which depends on the local electron temperature.

$$P_{e\to p} - P_{p\to e} = \sigma_e(T_e^{3.6} - T_p^{3.6}) \qquad \textit{Equation 25}$$

where the coefficient number of 3.6 is specific for NbN material (the superconducting material of the HEB we use in the experiment later). $\sigma_e = c_e S/(3.6T_e^{2.6}\tau_{eph})$ is the electron phonon coupling efficiency.

$$P_{p\to s} = \sigma_p(T_p^4 - T_s^4) \qquad \textit{Equation 26}$$

with $\sigma_p = c_p S/(4T_p^3\tau_{esc})$.

Substitute Equation 24-Equation 26 to Equation 23, and neglect the RF signal power P_S because it is too weak compared to the LO power, we get

$$\begin{cases} \frac{d}{dx}\left(\lambda_e \frac{dT_e}{dx}\right) - \sigma_e\left(T_e^{3.6} - T_p^{3.6}\right) + \frac{P_{LO}}{2L} + \frac{I_0^2 \rho(T_e)}{S} = 0 \\ \sigma_p\left(T_p^4 - T_s^4\right) - \sigma_e\left(T_e^{3.6} - T_p^{3.6}\right) = 0 \end{cases} \qquad \textit{Equation 27}$$

Solve two equations for electron temperature T_e, we get the I-V curves, the noise temperature, and the mixer gain for a substrate-based HEB mixer [32].

Figure 2-10 illustrates the electron temperature along the length of the superconducting bridge [32]. We can see that a hot spot is formed at the centre of the superconducting bridge. The temperature is highest at the centre of the hot spot, and then gradually reduces when the point moves away from the centre.

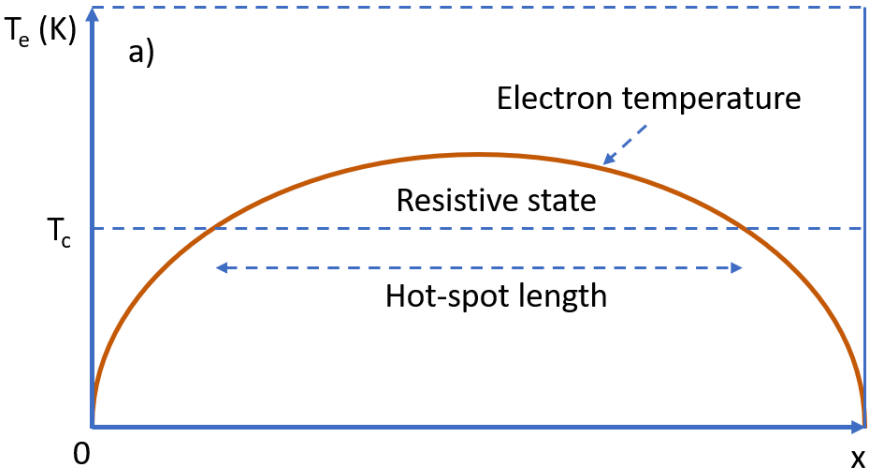

Figure 2-10. Electron temperature along the length of the superconducting bridge [32].

Figure 2-11 shows the I-V curves corresponding to different LO power levels: Unpumped - no LO power is applied, Under pumped – applied LO power is not enough for optimal mixing of the HEB, Optimal pumped - applied LO power allows an optimal mixing, Over pumped - too much LO power is applied leading the HEB to its normal state.

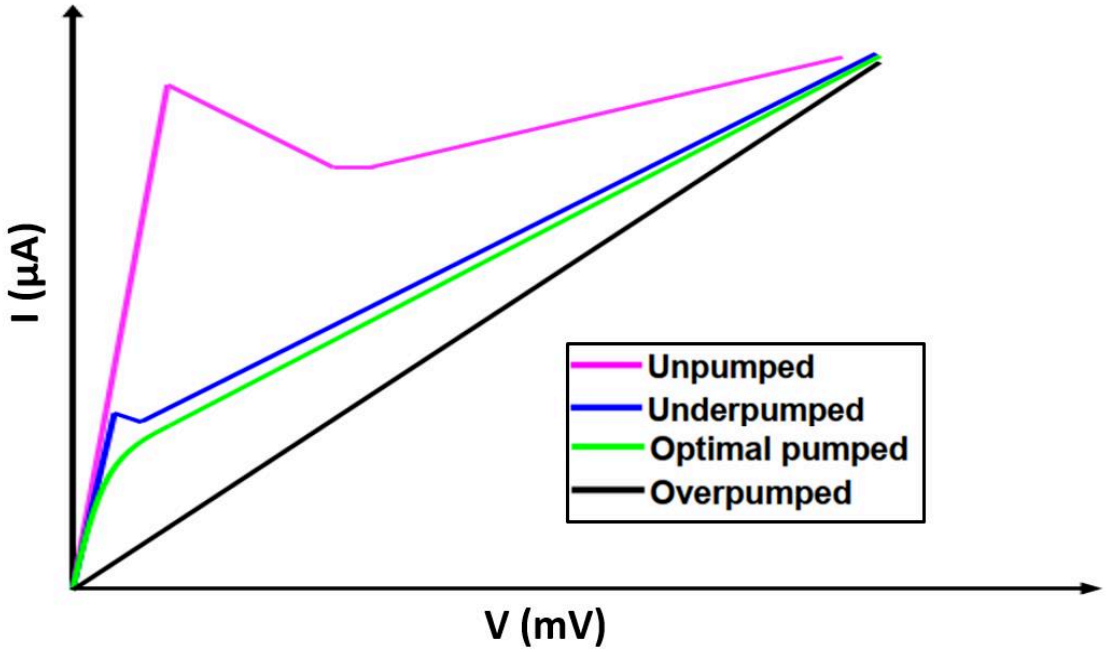

Figure 2-11. Typical I-V curves corresponding to different LO pumping levels.

We can see in Figure 2-11 that with the increase of absorbed LO power, the HEB mixer moves from its intrinsic superconducting state to mixing state, and then normal state.

2.5 Noise in HEB mixers

HEB mixers have two dominant noise sources: Johnson noise and thermal fluctuation noise. Besides, quantum noise must be taken into account at the higher THz frequency ranges.

2.5.1 Johnson noise

Johnson noise is the noise emitted by the thermal agitations of charge carriers. The double side band (DSB) equivalent noise temperature of the Johnson noise at the input of the HEB mixer can be described as [16], [33]

$$T_{Jn}^{in} = \frac{R_0 T_e}{I_0^2 C_{RF}^2 P_{LO}} (1 + \omega_{IF}^2 \tau_{mix}^2)^2 \qquad \textit{Equation 28}$$

Where R_0 is the resistance of the bolometer at temperature T_e; I_0 is the bias current; P_{LO} is the absorbed LO power at the bolometer; τ_{mix} is the mixing time constants; C_{RF} is the frequency-dependent heating capacity. C_{RF} can be calculated as

$$C_{RF}(\omega) = \frac{C_{RF}(\omega = 0)}{1 + j\omega\tau_0} \qquad \textit{Equation 29}$$

where τ_0 is the electron relaxation time.

As seen in Equation 29, the Johnson noise depends on the intermediate frequency, which increases at higher frequencies.

2.5.2 Thermal fluctuation noise

The thermal noise is caused by temperature fluctuations in the bolometer, or the resulted resistance fluctuations. The DC current change and the resistance change will cause the instability of the voltage. When HEB works at the optimal pumping levels, thermal noise contributes a dominant part. The DSB equivalent noise temperature of the thermal fluctuation noise at the input of the HEB mixer can be given by [16], [33]

$$T_{FL}^{in} = \frac{2T_e^2 \tau_\theta}{c_e V C_{RF}^2 P_{LO}} \left(\frac{\partial R}{\partial T}\right)^2 \frac{1 + \omega_{IF}^2 \tau_{mix}^2}{1 + \omega_{IF}^2 \tau_{th}^2} \qquad \textit{Equation 30}$$

where C_e is the electron heat capacity, V is the bolometer volume, R is bolometer resistance. τ_{mix} and τ_{th} are the mixing and electron temperature time constants, respectively. τ_{mix} and τ_{th} have close values, so the contribution of the thermal fluctuation to the noise temperature does not depend on the IF frequency. Moreover, looking at Equation 29 and Equation 30, while the equivalent noise temperature of the Johnson noise is proportional to electron temperature T_e, the thermal fluctuation noise is proportional to T_e^2. This

demonstrates that, when HEB working at optimal pumping levels, the thermal fluctuation noise plays the dominant part [16], [33].

2.5.3 Quantum noise

Quantum noise arises from the Heisenberg uncertainty principle. The minimum noise temperature of a single side band (SSB) is $\frac{hf}{k_B}$, where f is the working frequency of the receiver, k_B is the Boltzmann constant. In the case of DSB, this value equals to $\frac{hf}{2k_B}$. The higher frequency, the more contribution of the quantum noise to the noise temperature [16], [33]. An estimation in [20] shows that quantum noise is responsible for approximately 30 % of the total noise temperature of the DSB receiver when the frequency goes up to 4.3 THz.

2.5.4 Gain bandwidth and noise bandwidth

The gain bandwidth is defined as the IF frequency when the conversion gain reduces two times (or 3 dB) from its maximum. Meanwhile, the noise bandwidth is defined as the point where the noise temperature increases two times from its minimum. The relationship between gain and noise bandwidth can be given by

$$f_{noise} = f_{gain}\sqrt{\frac{T_{TFn}^{out} + T_{Jn}^{out} + T_{IF}}{T_{Jn}^{out} + T_{IF}}} \qquad \textit{Equation 31}$$

With T_{Jn}^{out} and T_{TFn}^{out} are the Johnson output noise temperature and thermal fluctuation noise at the output of the mixer, respectively. T_{IF} is the noise temperature of the IF chain [16], [33].

In theory, the IF gain bandwidth of a HEB can be up to 10 GHz [34]. In practice, IF gain bandwidth is around several GHz. For example, the gain bandwidth in [29] is approximately 4 GHz in experiment at the optimal pumping level. The gain bandwidth can be increased by reducing the phonon escape time τ_{esc} [34]. To do it, we need to make the superconducting film

thinner (as shown in Equation 17). But the thickness of the thin film is difficult to control (around 5 nm). Moreover, when making the superconductor thinner, the critical temperature of the film will be reduced, which increases the electron-phonon interaction time τ_{eph} (as shown in Equation 16). Another way to reduce the phonon escape time (and then increase the gain bandwidth) is to use the buffer layer (e.g. MgO) between the superconducting film and the substrate.

Chapter 3. Beam divider at 1.3 THz

3.1 Introduction

Multi-pixel heterodyne receivers have demonstrated undeniable advantages over single-pixel ones since they provide the possibility to observe multi regions of the sky simultaneously, thereby reducing the observation time and increasing the consistency of mapping data. As a result, the demand for receiver array is growing, with several projects already launched [10], [35] or under preparation [36]. In a receiver array, each receiver contains a mixer, which needs to be fed by a LO. To provide LO power to all mixers of an array, the most efficient way is to divide one LO source into several beams. There are two common methods to split the beam: waveguide splitting and phase grating. This study concerns the latter one and is based on the concept developed in our lab (LERMA) [37], [38].

This chapter presents the development of a system based on a global phase grating to divide a single beam source at 1.3 THz into four output beams to feed a 2 x 2 pixel HEB mixer array which is under development at our laboratory. The THz source is provided by an Amplifier-Multiplier Chain (AMC) by VDI (Virginia Diodes, Inc) [39]. The objective of this work is also to provide an intermediate step towards building LO feeding systems for larger mixer arrays and at higher frequencies.

This phase grating was designed and fabricated at the beginning of my thesis. My work concerns in particular the analysis of the beam properties with the help of the MATLAB code and a 3D EM software [40]. I took part in

the testing phase and compared the measured characteristics of the output beam with the simulated ones. I also proposed a new version of the phase grating design code to increase the number of the output beam from four to sixteen.

3.2 Design principle

3.2.1 Gaussian beam optics

In conventional optics, the size of the optical components (e.g. mirrors, lens) is large enough compared to the wavelength. Thus, the light propagation can be described using geometric light rays and considered independent of the wavelength.

Quasi-optical region stays between electronics and conventional optics, ranging from far-infrared to terahertz and even mm-wave frequencies. In contrast to conventional optics, quasi-optics investigates the propagation of electromagnetic radiation where the wavelength is comparable to the size of the optical components and the diffraction can be a big problem [41]–[43].

Gaussian beam optics [41]–[43] is commonly used to describe the propagation where the beam width is comparable to the wavelength and its profile follows the Gaussian distribution. In practice, feedhorns are widely used in the THz research field, and they radiate beams with amplitude distributions very close to the Gaussian function. It is the case of the AMC THz source used in this work [39]. It thus is helpful to understand the formulas of the Gaussian beam and Gaussian propagation to design and simulate the quasi-optical system.

The history of Gaussian beam propagation can go back to the 1960's, when scientists tried to develop a practical concept to describe the behaviour of the laser beam propagation [43]. Goldsmith described Gaussian beam optics in

his book [43]. Here I quickly introduce the essential equations below. To summarise, the E-field distribution of the Gaussian beam along the optical axis (Z-axis) is [43]:

$$\frac{E(r,z)}{E_0} = \frac{\omega_0}{\omega(z)}.exp\left[-\left(\frac{r}{\omega(z)}\right)^2\right]. \qquad \textit{Equation 32}$$
$$.exp\left\{-i\left[kz - arctan\left(\frac{z}{z_R}\right)\right]\right\}.exp\left(-i\frac{kr^2}{2R(z)}\right)$$

Where E_0 is the vector of the electric filed at r = 0 and z = 0.

The term $\frac{\omega_0}{\omega(z)}.exp\left[-\left(\frac{r}{\omega(z)}\right)^2\right]$ as the amplitude factor.

The term $exp\left\{-i\left[kz - arctan\left(\frac{z}{z_R}\right)\right]\right\}$ as the longitudinal phase factor.

The term $exp\left(-i\frac{kr^2}{2R(z)}\right)$ as the radial phase factor.

Where ω_0 is the beam waist radius at the plane z = 0; r is the radial distance from a point in the plane perpendicular to the optical axis to the optical axis; $\omega(z)$ is the beam radius in the plane perpendicular to the z-axis where the intensity reduces $1/e^2$ compared to the highest value of the Gaussian beam in the same plane; R(z) is the radius of curvature of phase front at z. k is the wave number. These parameters are shown in Figure 3-1.

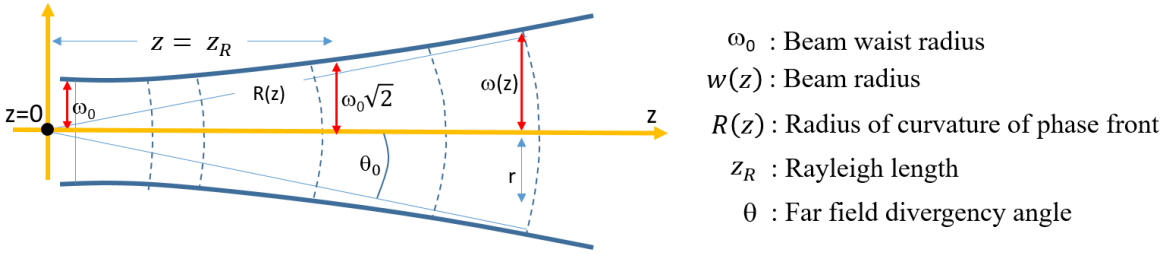

Figure 3-1. Gaussian propagation along the optical axis.

The beam radius of the Gaussian beam at the distance z can be written:

$$\omega(z) = \omega_0 \sqrt{1 + \left(\frac{z}{z_R}\right)^2}$$ *Equation 33*

The radius of curvature of the phase front is given by:

$$R(z) = z\left[1 + \left(\frac{z_R}{z}\right)^2\right]$$ *Equation 34*

Rayleigh length defines the distance where the Gaussian beam propagates without significant growth–meaning that it remains essentially collimated, or the radius of the beam waist is $\omega_0\sqrt{2}$. The distance z_R of Rayleigh length is:

$$z_R = \frac{\pi\omega_0^2}{\lambda}$$ *Equation 35*

After z_R, the beam will grow dramatically.

The far-field divergence angle in the paraxial case is:

$$\theta_0 \approx tan\theta_0 = \lim_{z\to\infty} \frac{w(z)}{z} = \lim_{z\to\infty} \frac{w_0\sqrt{1+\left(\frac{z}{z_R}\right)^2}}{z} = \frac{w_0}{z_R} = \frac{\lambda}{\pi\omega_0}$$ *Equation 36*

Let's consider a plane that is perpendicular to the optical axis. The radiation of this plane also follows the Gaussian distribution, with the highest amplitude point on the optical axis.

The distribution of Electric field E and Intensity I of the Gaussian beam at the distance r from the optical axis is given by:

$$\frac{|E(r,z)|}{|E(0,z)|} = exp\left[-\left(\frac{r}{\omega}\right)^2\right]$$ *Equation 37*

and

$$\frac{|I(r,z)|}{|I(0,z)|} = exp\left[-2\left(\frac{r}{\omega}\right)^2\right]$$ *Equation 38*

At a distance $r = \omega$, we have $\frac{|E(r,z)|}{|E(0,z)|} = \frac{1}{e}$ and $\frac{|I(r,z)|}{|I(0,z)|} = \frac{1}{e^2}$ (13.53 % or -8.7 dB).

We also have $I = \frac{P}{A}$, where P is the power through an area A, so

$$\frac{|P(r,z)|}{|P(0,z)|} = exp\left[-2\left(\frac{r}{\omega}\right)^2\right] \qquad \textit{Equation 39}$$

Fractional power ($FP(r)$) in a circular area with a radius r is:

$$FP(r) = \frac{\int_0^r P(r).2\pi r.dr}{\int_0^{+\infty} P(r).2\pi r.dr} = 1\text{- } exp\left[-2\left(\frac{r}{\omega}\right)^2\right] \qquad \textit{Equation 40}$$

Thus, the amount of the power in a circle with the radius $r = \omega$ is 86.5 % of the total power in the plane, and becomes 99.97 % (or almost 100 %) when the radius $r = 2\omega$.

3.2.2 Phase grating

A phase grating is a structure that can generate output beams with phase variations from the incident beam. In reflective phase grating, the variation of the height of the local surface of the optical substrate creates the reflected rays containing spatially phase change [44], [45]. Constructive interferences will form new output beams, as shown in Figure 3-2. This mechanism is applied to generate multi-LO beams for multi-pixel receivers.

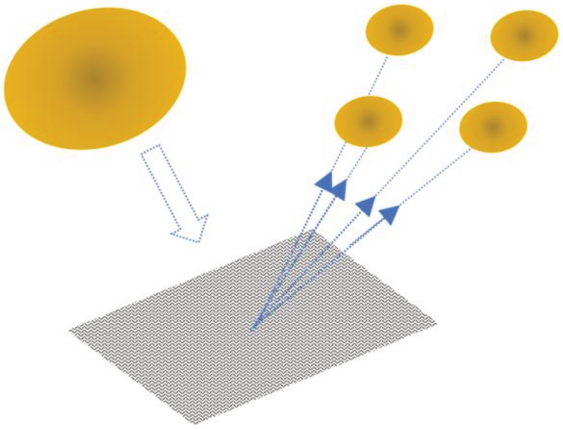

Figure 3-2. Reflective phase grating

3.2.2.1 Stepped and Fourier phase grating

The two most common phase gratings are stepped grating and Fourier grating. For stepped grating, the most straightforward shape is Dammann grating. It is a two-level phase grating in which the discrete variation of the level of the height of the substrate varies between two values (usually of -1 and 1), generating two-phase modulation of 0 and π. The constructive and destructive phase combination could generate several sub-beams from one LO source. The theory of Dammann grating has been developed by several scientists [46]–[48]. The stepped grating has the similar working mechanism as the Dammann grating. It contains more than 2 step levels, making it more flexible to create more discrete phase modulation, increasing the grating efficiency.

Unlike stepped phase gratings, which only contain several discrete phase shift levels, Fourier gratings can be with continuous phase modulation thanks to the smooth grating structure. The continuity of phase variation will usually produce sub-beams with higher efficiency than discrete ones. This phase grating concept was first introduced in 2001 by U. Graf and S. Heyminck [49].

Both Dammann and Fourier gratings have some limitations. Their surface structures must be periodic. The Dammann gratings usually have a lower efficiency than Fourier gratings. Fourier gratings could not have sharp edges—although the sharp edges would be helpful in some cases if the desired beam patterns are complex.

3.2.2.2 Global phase grating

In order to overcome the limitations of the gratins described above, a new concept called Global phase grating has been developed at LERMA [37], [38]. In this model, there are no limitations about grating's surface structure: it can be periodic or not and can contain or not sharp edges. The flexibility on the structure design allows to produce almost any complex far-field patterns and to better adapt to the requirement of output beams.

The Global phase grating algorithm and the calculation steps are illustrated in Figure 3-3 [37].

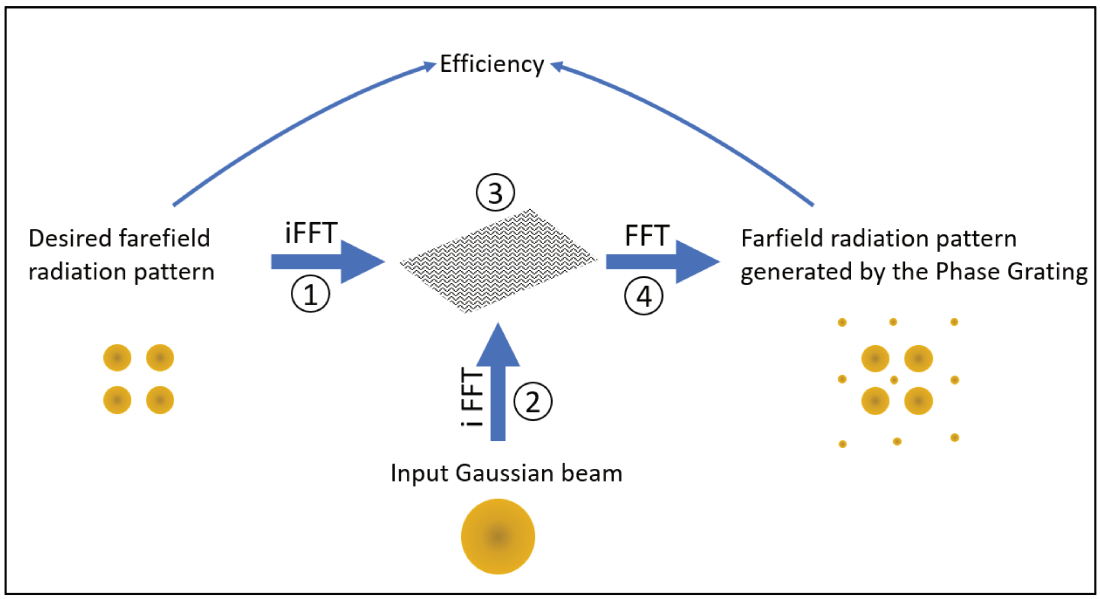

Figure 3-3. Calculation algorithm to generate the phase grating's surface

The initial conditions are chosen before starting the calculation. They are: the working frequency, the size of the Gaussian input beam, the distance

between the phase grating and the output plane, the distance between each pixel, and the incident angle of the Gaussian input beam. Then the calculation program written on MATLAB will perform the following steps:

(1) The desired far-field beam pattern, which contains several Gaussian output beams at desired positions (in spatial coordinates), is mapped onto the aperture plane using an inverse FFT.
(2) The input Gaussian beam is mapped onto the aperture plane by an inverse FFT.
(3) At the aperture field, the phase profile of the Global phase grating is determined as the phase difference of the input and output Gaussian beams. Phase grating is generated by coupling this phase profile to the amplitude distribution of the Gaussian input beam.
(4) The far-field radiation beam pattern of the phase grating is generated by an FFT.

3.3 Design of the LO feeding system using Global phase grating at 1.3 THz

3.3.1 Overview of the LO feeding system and design tools

The objective of this work is to build a quasi-optical system to feed a four-pixel HEB mixer array with a single beam LO source at 1.3 THz. The mixer array is currently under development at our lab. It contains an array of four HEB mixers in a square form and the distance between pixels is 16 mm. The THz source provided by an AMC from VDI is emitted by a diagonal horn. The feeding system should be able to divide the signal beam from the LO source into four beams and then focus them on each pixel of the mixer array which is inside a cryostat under normal operating condition.

The schematic of the system to be designed is shown in Figure 3-4. It contains the horn of the THz source, a phase grating and an elliptical mirror.

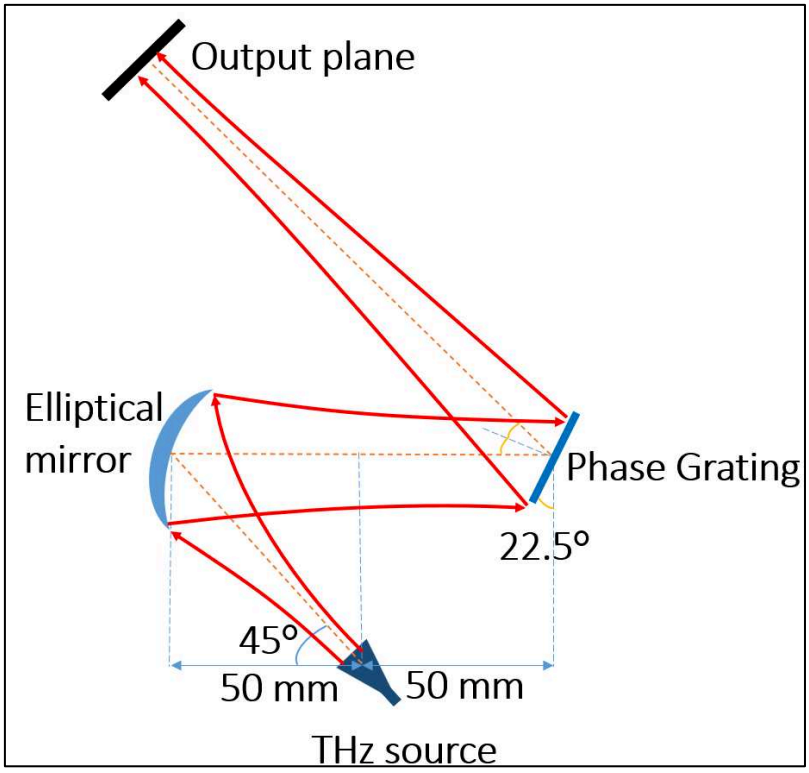

Figure 3-4. Schematic of the LO feeding system.

The THz source stays at the first focal point of the elliptical mirror. The beam emitted by the source reaches the phase grating after being reflected by the elliptical mirror which will focus the divided beams on its second focal plane where will be located the mixer array. The dotted line represents the optical axis, while the red lines show the boundary of the beam propagation.

Taking into account of the mixer array measurement setup including a cryostat, the distance from the center of the phase grating to the output plane is about 300 mm – 410 mm. The incident angle of the beam divider is set at 22.5 °.

Different design tools are used for the design of this LO feeding system. The Global phase grating surface geometry is obtained by running a

MATLAB calculation program developed at LERMA. The focusing mirror is defined by the dedicated mirror equations. The 3D EM simulation is extensively used to verify the designed grating and then to simulate the EM wave propagation in the whole optical system, from the THz to the output plane.

The 3D electromagnetic software we used for modelling is FEKO [40]. This program is based on the solution method where Integral Equations are solved by the Method of Moments (MoM), which is suitable for analysing the coupling and radiation. FEKO also features Multilevel Fast Multimode Method (MLFMM), which helps to shorten the simulation time in the free space MoM. It also equips other high-frequency asymptotic techniques, such as Large Element - Physical Optics (LE-PO) and Ray-Launching Geometrics (RL-GO), ideal for our applications when we need to work with electrically massive scattering structures [50].

3.3.2 Calculation of the grating's profile and far-field pattern

The phase grating that we chose for our feeding system is a reflective grating with a single input beam and four output beams as illustrated in Figure 3-5. The concept is based on the Global phase grating. The working frequency is chosen at 1.3 THz.

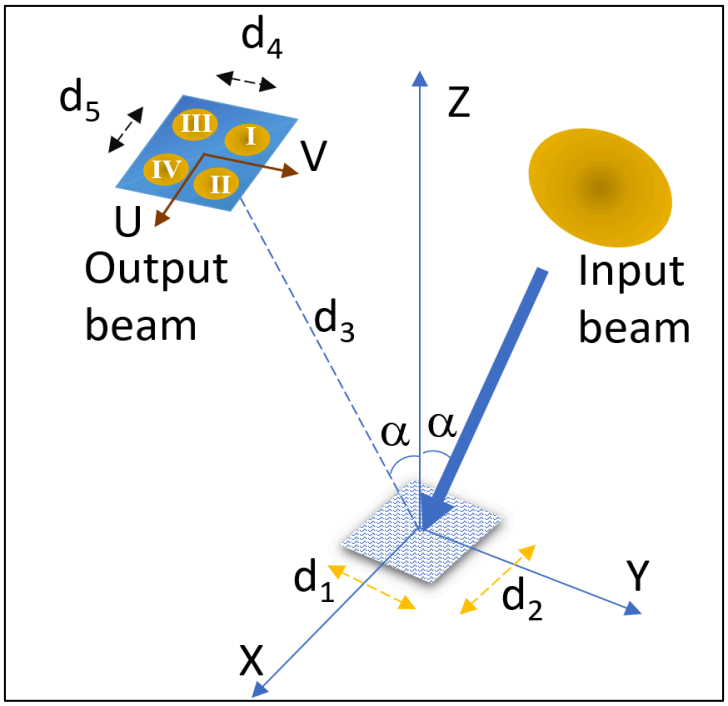

Figure 3-5. Schematic showing the input parameters to generate the phase grating. Four output pixels are denoted as I, II, III, and IV.

The distance between two adjacent beams is 16 mm along with U (or X) and V (or Y) axis (distances d_4 and d_5). The optical length from the centre point of the phase grating to the resulting plane is around 300 mm (distance d_3). This distance is determined following the arrangement of the quasi-optical coupling test bench and the position of the receiver array we will make later. The incident angle from the Gaussian input beam to the normal vector of the plane containing the phase grating is 22.5 ° (angle α). The size of the phase grating (d_1 x d_2) is chosen as 20 mm x 20 mm for practical reasons. Considering the oblique incident beam in the YZ plane with an angle α = 22.5 °, d_1 is scaled with a factor of 1/cos(α). So the designed grating size is 20 mm x 21.6 mm.

The above parameters are entered in the MATLAB program, for generating the geometry of the Global phase grating in Figure 3-6.

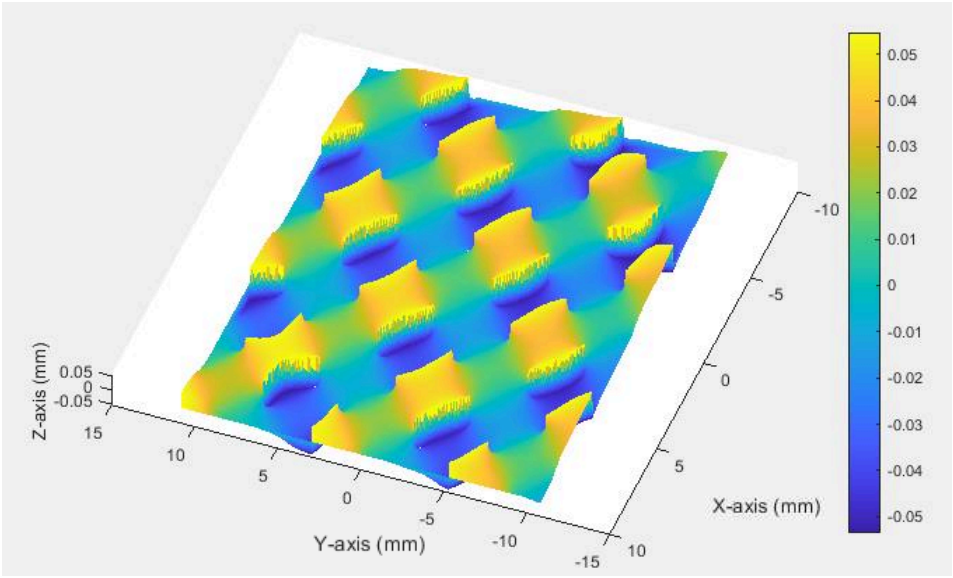

Figure 3-6. Surface of the 2 x 2 phase grating with the size of 20 mm x 21.6 mm

At the output plane, 2 x 2 output beams should be formed, with a distance between 2 adjacent beams of 16 mm.

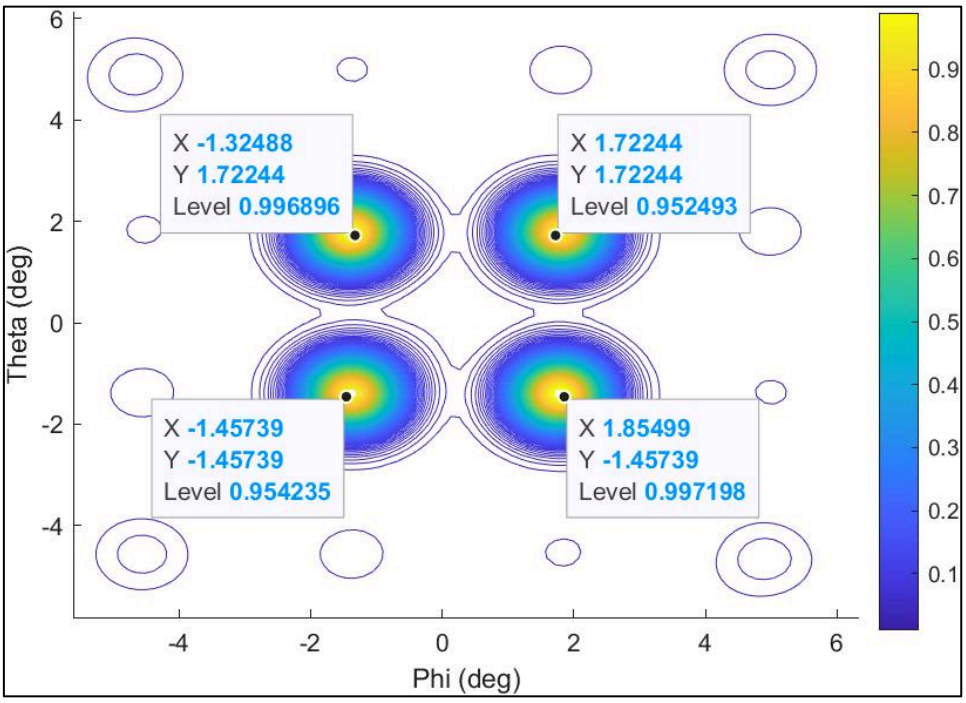

Figure 3-7. Far-field profile generated by the 2 x 2 phase grating

The far-field profile of this phase grating is shown in Figure 3-7. MATLAB's calculation shows that four beams are almost homogeneous. However, this code does not take into account the multi-reflection between the surface regions, and the shadowing. So we should perform 3D EM simulation for a more accurate simulation of the divider structure and the output beam patterns.

3.3.3 Simulation of THz source

A good knowledge on the beam characteristics of the THz source is necessary for the design of the quasi-optical system. We have then first studied the output beam of the AMC at 1.3 THz. According to the documentation of the VDI AMC S235 [39], beam is emitted by a diagonal WR0.65 horn, which works at a frequency range of 1100-1700 GHz. For the simulation, we constructed this horn with the exact dimensions found in the datasheet. After that, a 3D EM software (e.g. FEKO) is used to simulate the emission of this horn. Then we compare the results with that provided by the manufacturer.

The horn and its simulated far-field are shown in Figure 3-8.

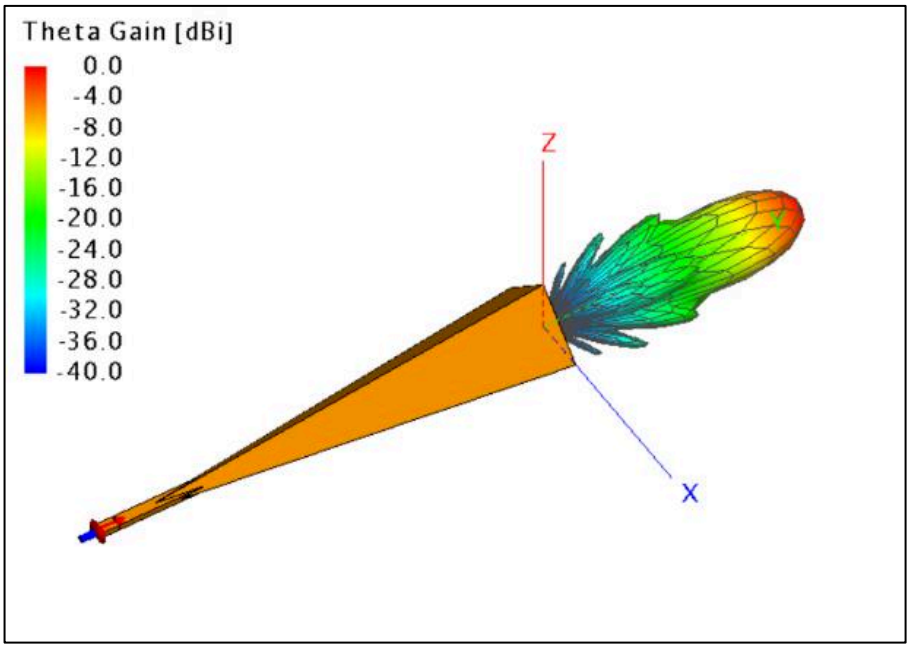

(a)

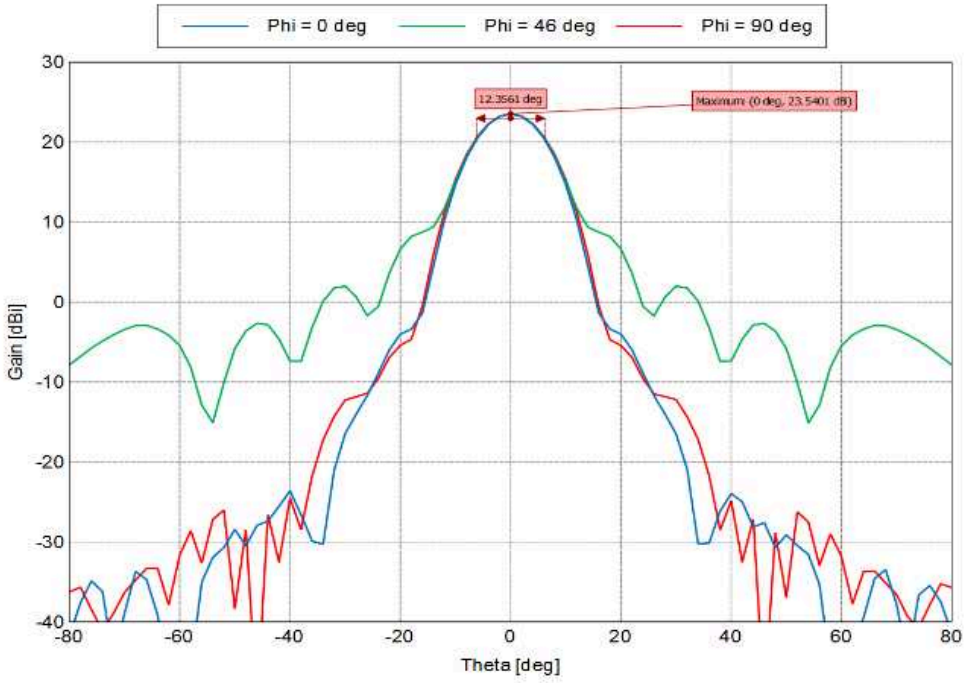

(b)

Figure 3-8. a) Simulated horn and its far-field. b) Profiles of the far-field.

Intuitively, the result in Figure 3-8 shows a good Gaussian beam shape in the far-field of theta gain (in dBi). The far-field gain of theta (in dB) at $\varphi = 0°, 46°$, and 90 ° overlapped when θ in the range of (-17 °;17 °).

We compared the simulated parameters with the ones provided by the manufacturer. In both cases, the full 3-dB beamwidth is between 11 ° and 12 °, and the gain is between 24 dBi and 25 dBi. Moreover, the simulated beam waist is 0.4 mm and is the same as shown in the datasheet. This proves that this horn model can be used as a THz source for further quasi-optical simulations.

3.3.4 Simulation of the THz source beam after the elliptical mirror

3.3.4.1 Calculation of the elliptical mirror

The Gaussian beam emitted by the horn needs to be focused on the output plane. To do it, we use an elliptical mirror—a part of the ellipsoid surface. The attractive property that makes it valuable is: the input beam from its first focal point, when coming to its surface, will focus on its second focal point.

To ensure the efficiency of the coupling between the horn and the mirror, we need to ensure that [43]:

- Input beam (Gaussian beam from horn) has the radius of curvature $R_{in} = R_1$.
- Output beam (Beam reflected by the elliptical mirror) has a radius of curvature $R_{out} = R_2$.

where R_1 and R_2 are the distances from two focal points F_1 and F_2, to a point on the surface of the elliptical mirror, respectively.

To meet as far as possible the conditions $R_{in} = R_1$ and $R_{out} = R_2$, and the requirement of the mixer array testbench, we find out the distance R_1 = 70 mm, R_2 = 400 mm.

Moreover, to have higher reflected power, lower distortion [43], and also for better alignment, we choose the incident angle of the input beam θ_i = 22.5 °.

These parameters: R_{in}, R_{out}, and θ_i are enough to determine an elliptical mirror, as illustrated in Figure 3-9. A and B are two focal points, C is a point staying in the surface of the elliptical mirror. The magnification of the elliptical mirror is estimated:

$$M = \frac{BD}{AD} = \frac{\omega_{out}}{\omega_0} \approx 7 \qquad \textit{Equation 41}$$

with ω_0= 0.4 mm, so the ω_{out}= 2.8 mm.

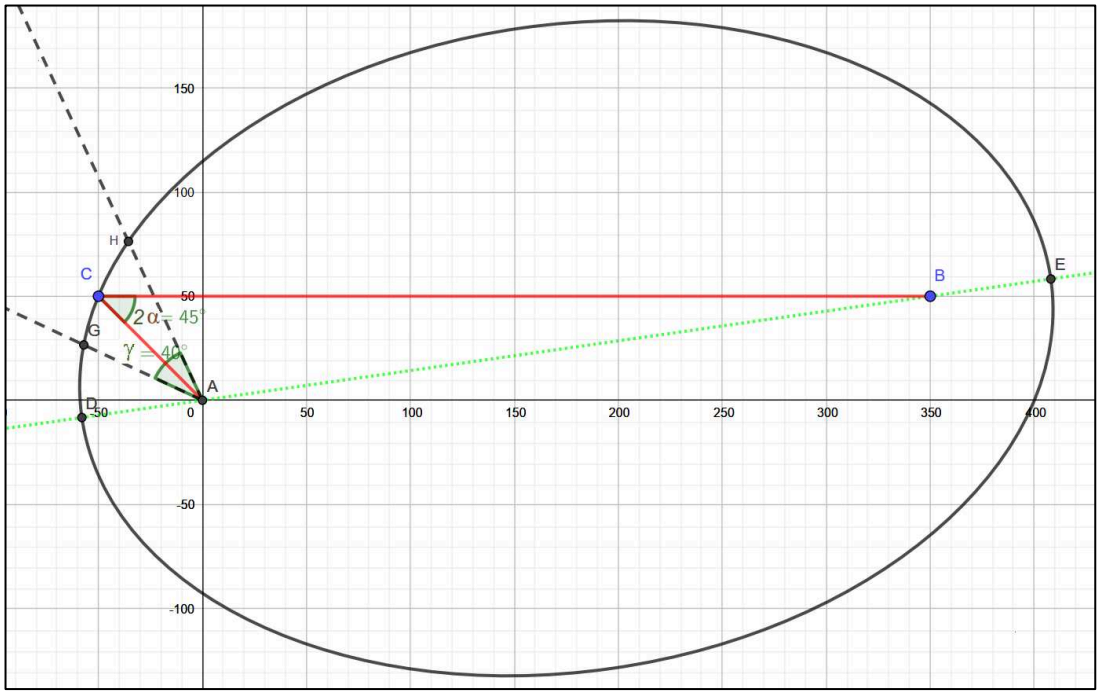

Figure 3-9. Schematic of the elliptical mirror.

The size of a mirror is also determined to ensure that it covers almost all energy from the horn. In our case, the mirror covers an area that is limited by the curve passing through points G, C and H in Figure 3-9. This area covers horn's radiation at the total angle of 40 °, which is large enough according to Figure 3-8.

3.3.4.2 Simulation of the THz source beam after the elliptical mirror

This section presents the simulated characteristics of the input beam reflected by the elliptical mirror at the location of the output plane. The optical path is shown in Figure 3-10. The THz beam is captured at a distance of 410 mm from the centre of the elliptical mirror.

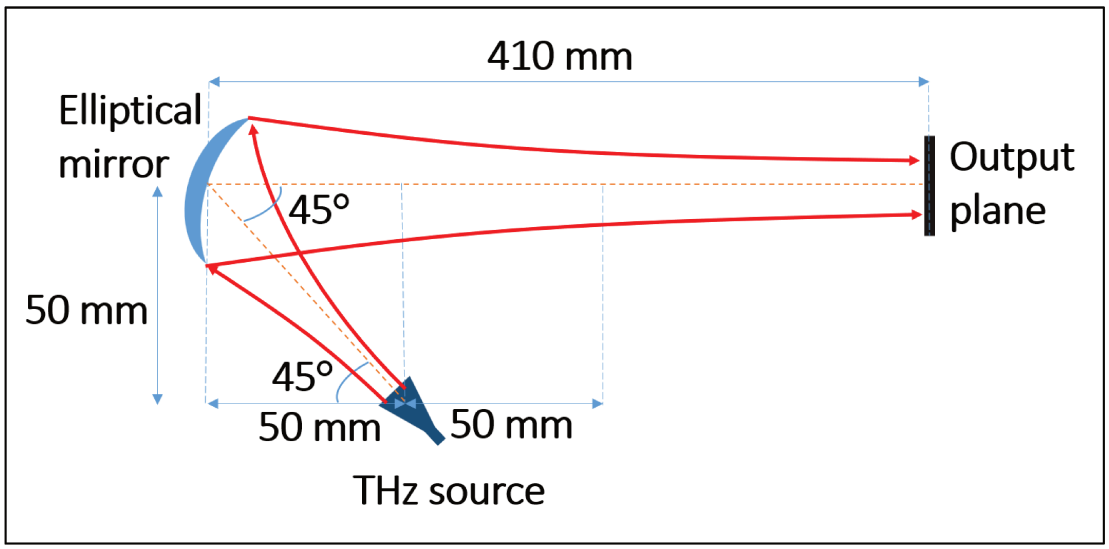

Figure 3-10. Quasi-optical setup to simulate the Gaussian input beam after the elliptical mirror

The beam pattern captured at the output plane is shown in Figure 3-11. The radius of this output beam is 2.99 mm at a distance of 410 mm. Meanwhile, the radius of the output beam at the distance of 400 mm is 2.73 mm, which is close to our estimation (2.8 mm) in Section 3.3.4.1.

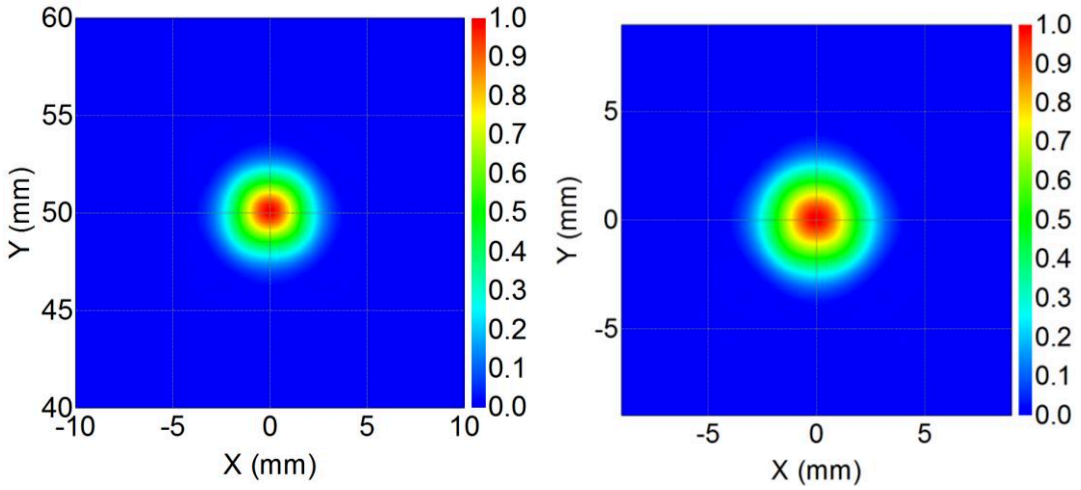

(a) (b)

Figure 3-11. Normalized intensity of the simulated beam pattern captured at the output plane. a) Distance 400 mm from the elliptical mirror. b) Distance 410 mm from the elliptical mirror.

This output beam is fitted with the two-dimensional (2D) Gaussian function which is given by

$$f(x,y) = Aexp(-2(a(x-x_0)^2 + 2b(x-x_0)(y-y_0) + c(y-y_0)^2)) \qquad \textit{Equation 42}$$

with

$$a = \frac{cos^2\theta}{\omega_1^2} + \frac{sin^2\theta}{\omega_2^2},\ b = -\frac{sin2\theta}{2\omega_1^2} + \frac{sin2\theta}{2\omega_2^2},\ c = -\frac{sin^2\theta}{\omega_1^2} + \frac{cos^2\theta}{\omega_2^2} \qquad \textit{Equation 43}$$

where A is amplitude, $(x_0; y_0)$ is the coordinate of the highest intensity point, ω_1 and ω_2 are two radius (semi-major and semi-minor axes) of the 2D Gaussian pattern.

The beam profile along the X-axis and Y-axis with the Gaussian fit are shown in Figure 3-12. We see that the simulated input beam after the elliptical mirror follows the Gaussian distribution.

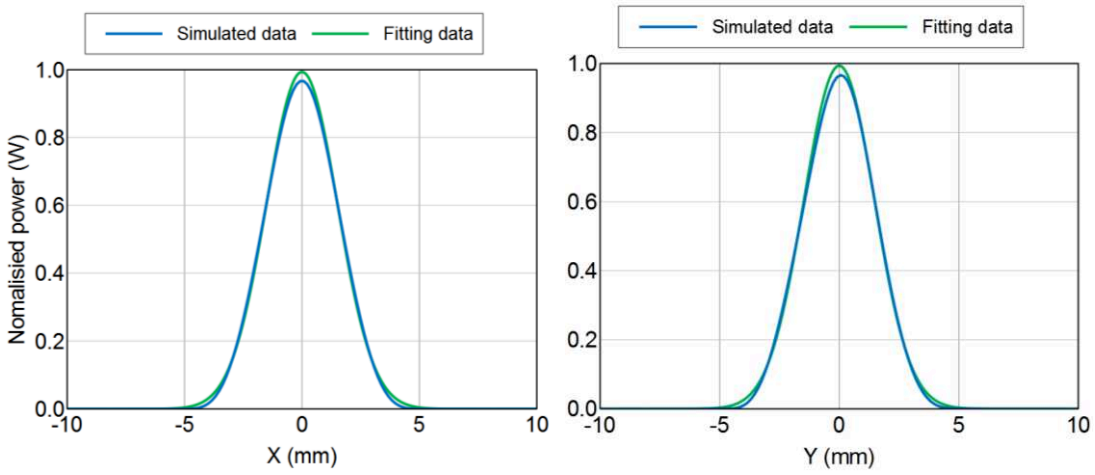

(a) (b)

Figure 3-12. Beam profile of the simulated input beam and its 2D Gaussian fit. a) Along X-axis. b) Along Y-axis.

3.3.5 Simulation of the output pattern of the phase grating

This section presents the simulation results of the phase grating inserted in the LO feeding system described in Figure 3-4.

The Gaussian beam emitted by the horn and reflected by the elliptical mirror reaches the phase grating with the angle of $\alpha = 22.5°$ and is divided into four beams. These beams are simulated at the output plane perpendicular to the optical axis, with the distance from the center of the phase grating of 310 mm (corresponding to the optical length from the elliptical mirror of 410 mm).

The simulated beam pattern at a distance of 410 mm from the elliptical mirror is shown in Figure 3-13 with the number of each pixel indicated in the same figure.

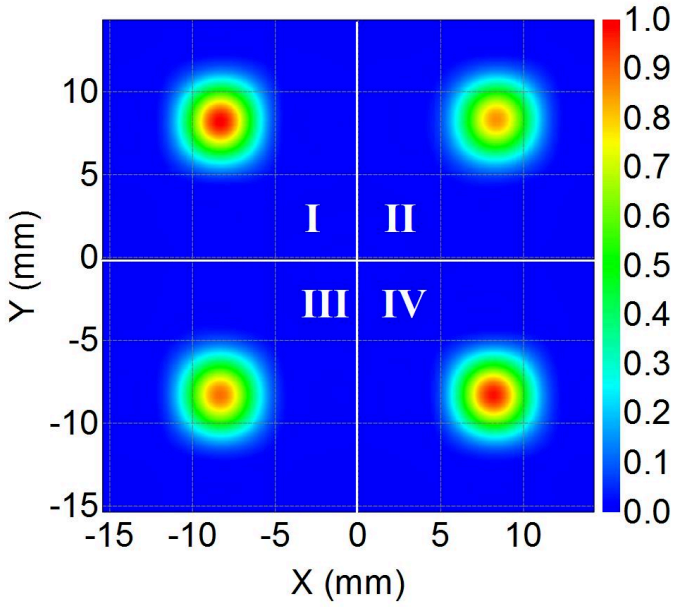

(a)

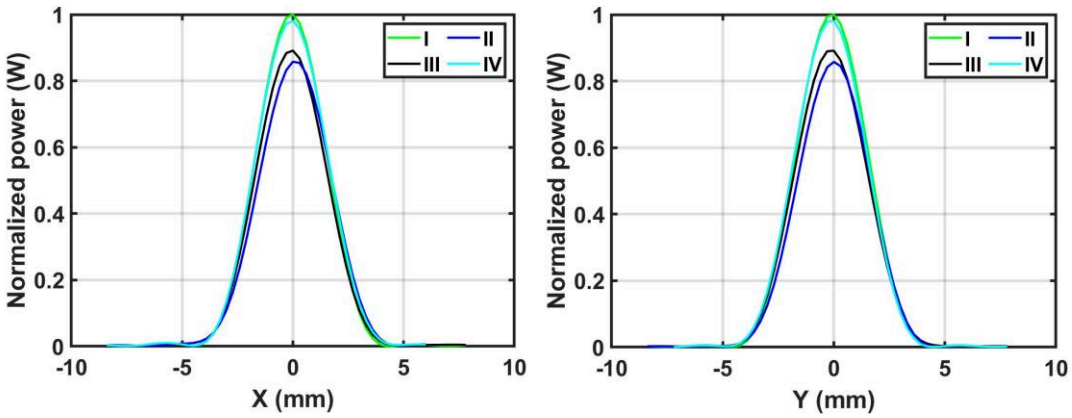

(b1) (b2)

Figure 3-13. Simulated beam pattern after the phase grating (at a distance of 410 mm from the elliptical mirror); a) 2D pattern. b1) Beam profile along X-axis. b2) beam profile along Y-axis.

According to the simulation results, the distance between 2 adjacent pixels is 16.5 mm at a distance 410 mm far from the phase grating, as expected. As shown in Figure 3-13, there is a variation between the highest amplitudes of

the four simulated pixels. Each pixel contains between 18.2 % to 20.3 % of the power of the incident beam. The total efficiency of 4 pixels is around 78 %.

Each simulated pixel is then fit to the 2D Gaussian function. The simulated and fitted beam profiles along X-axis are shown in Figure 3-14. We can see that the simulated beam pattern is very close to Gaussian distribution.

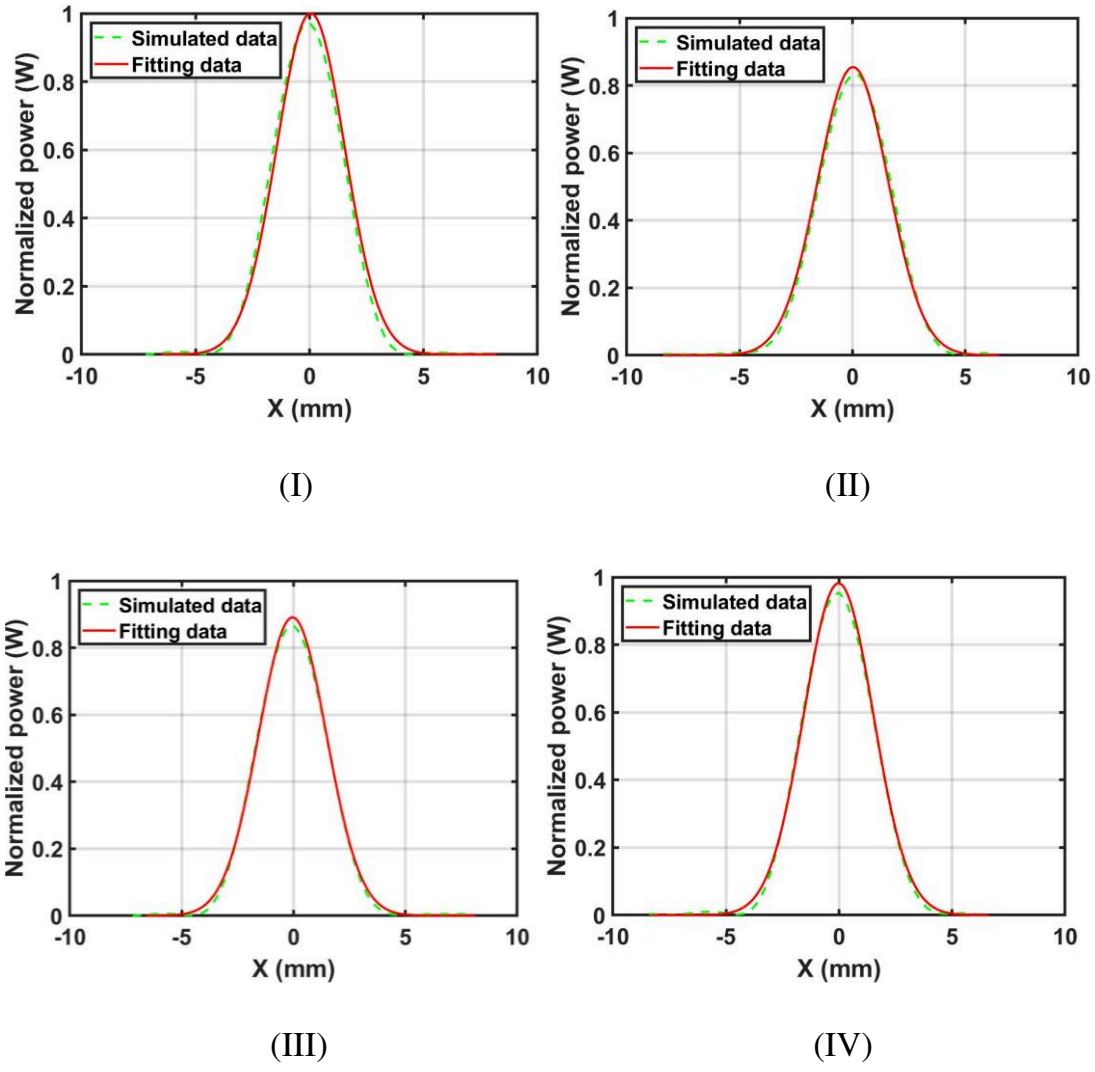

Figure 3-14. Measurement and fitting of the beam profile cut through the highest intensity point of pixel I, II, III, and IV along the X-axis at a distance 310 mm far away from phase grating (or 410 mm from elliptical mirror).

3.3.6 Investigation of the factors that can affect output beams

During the simulation, we noticed that several factors can affect the efficiency of the output beams, the homogeneity and the distance between 2 adjacent pixels. In this section, the factors which can affect the characteristics of the output beams are analysed by the 3D EM simulation.

3.3.6.1 Influence of the phase grating size

This task studies the effect of the phase grating size on the output pattern. Our phase grating is initially designed with the size of 40 mm x 43 mm (in MATLAB calculation). For practical reasons relating to the manufacturing, this size is reduced to 20 mm x 21.6 mm, which is four times smaller.

At first, we investigate how much energy flows through two window sizes: 20.0 mm x 21.6 mm and 40 mm x 43 mm, where we will put the phase grating later. The setup of the quasi-optical system containing a horn and an elliptical mirror is shown in Figure 3-15a. The distance from the centre of the elliptical mirror to the centre of the windows is 100 mm.

The normalised input beam power (in dB) over the sizes 40 mm x 43 mm is shown in Figure 3-15b. The black square represents the window size of 20.0 mm x 21.6 mm. Though the smaller size occupies a large part of the energy, the power still leaks around the square. The smaller window receives an amount of energy equal to 87 % integrated intensity over the plane. Conversely, 99.9 % of integrated intensity goes through the bigger window (i.e., 40 mm x 43 mm). So, 300 % bigger size goes with 13 % higher integrated intensity.

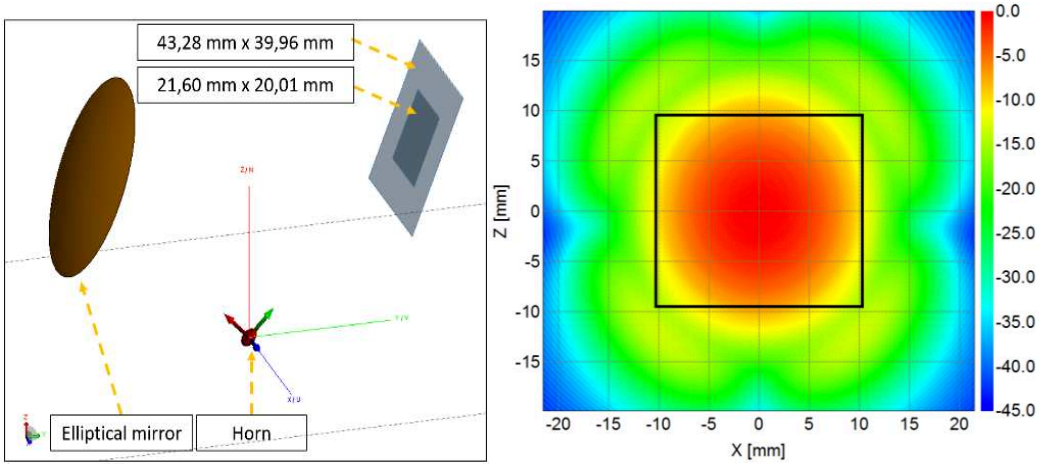

(a) (b)

Figure 3-15. a) Quasi-optical coupling system containing horn and elliptical mirror. b) Power distribution over the window with 40.0 mm x 43.0 mm. The black window shows the power distribution inside the size 20 mm x 21.6 mm

After that, two phase gratings (20 mm x 21.6 mm and 40 mm x 43 mm) are alternately imported to FEKO to study the effect of the phase grating size on the output beams. Each simulation is performed at a distance of 300 mm from the phase grating to the output plane (or 400 mm from the elliptical mirror to the output plane). The setup for this simulation (Figure 3-16) is similar to

that shown in Figure 3-4 and Figure 3-5. The incident and reflected angle of the THz source are set to 22.5 °.

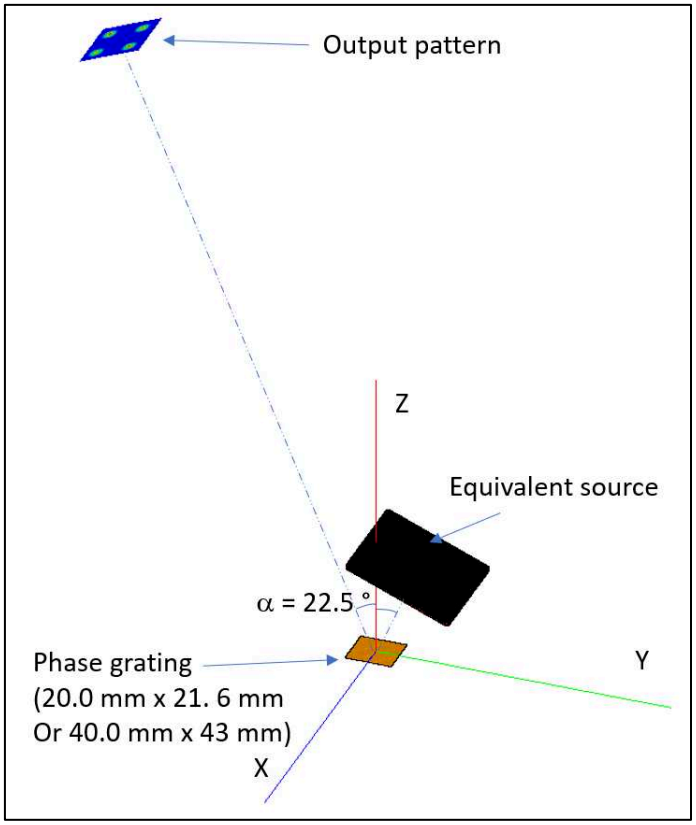

Figure 3-16. Setup of the quasi-optical system and the phase grating.

The efficiency of the phase grating is calculated by the division of the integrated intensity of four output beams over the one of the beam at the input of the grating. According to the simulation, it is 89 % with the graing size of 40 mm x 43 mm, being 12 % higher than the one with the size of 20 mm x 21.6 mm. This is shown in Figure 3-17, where the normalized intensity of the pixels in case of the size of 40 mm x 43 mm is consistently higher than the one of 20 mm x 21.6 mm.

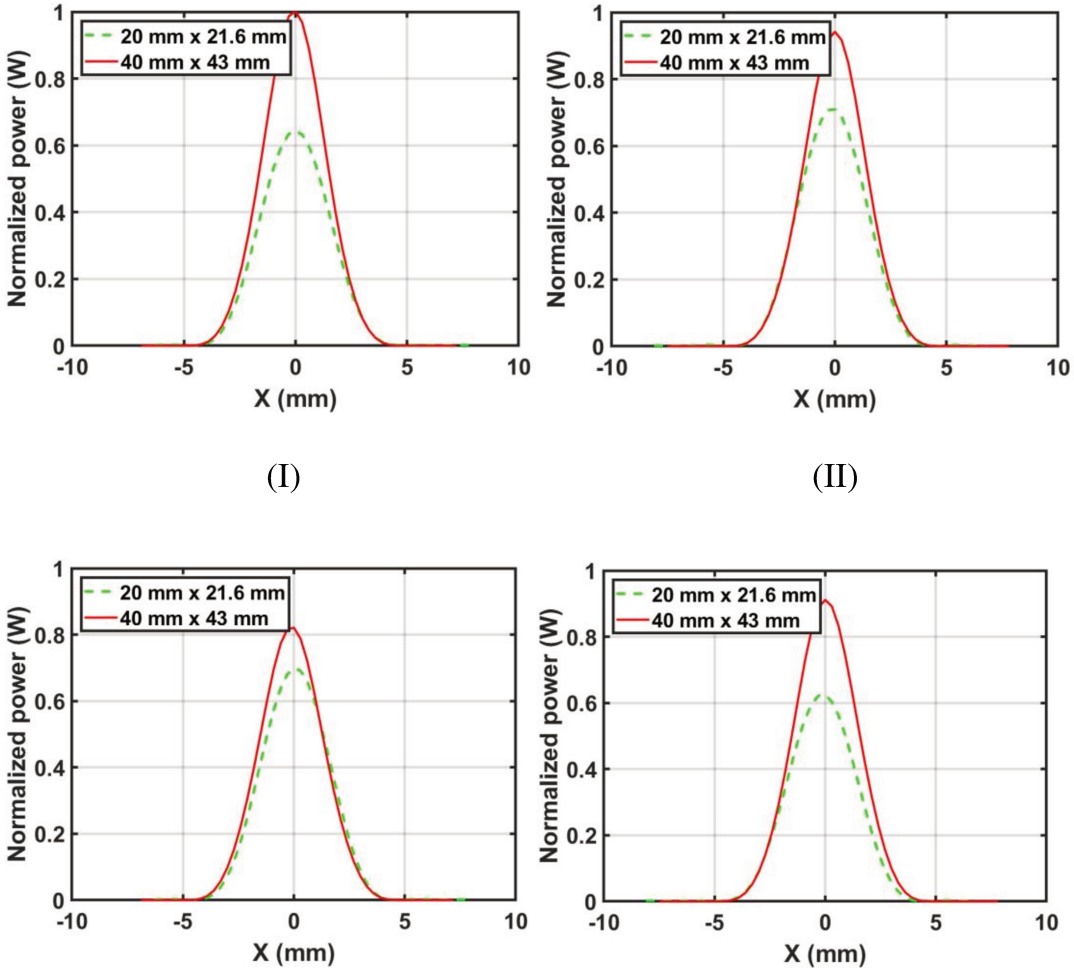

Figure 3-17. Beam profiles of pixel I, II, III, and IV with 2 different sizes of phase grating

Although the bigger size (i.e. 40 mm x 43 mm) shows an advantage (higher efficiency) over the smaller ones, we selected the size of 20 mm x 21.6 mm —to make the prototype—to save the time of simulation and fabrication. This smaller sample is used to test the correlation between simulation and measurement. Later on, we can move toward manufacturing the bigger size of the phase grating.

3.3.6.2 Influence of continuous and discretized profile of the phase grating

The surface geometry of the phase grating calculated by MATLAB contains 3D patterns with a height ranging from several to a hundred micrometers. The profile of the patterns is by default continuous, it seems not very easy with the milling machine to reproduce the whole structure with very high accuracy. We tried to replace the continuous profile to discretized one with a step of 10 μm for facilitating the manufacturing. In this part, we intend to find out the effect of this modification on the output beam pattern.

3D simulations are also performed to compare the output beams generated by two kinds of phase grating. Output beams are sampled at a distance of 300 mm far away from the phase grating.

The peaks of the output pixels generated from phase grating with continuous levels are slightly higher than those with stepped levels, but the beam shape remains the same, as shown in Figure 3-18.

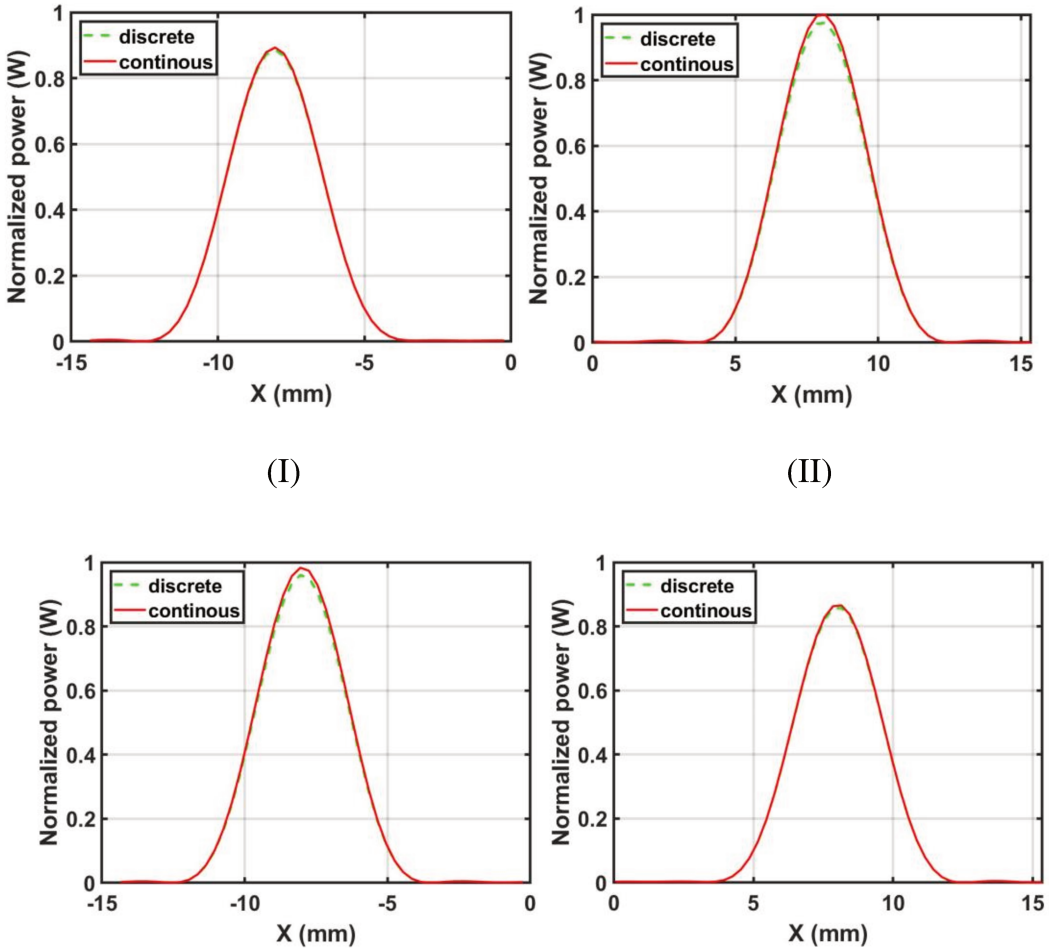

Figure 3-18. Beam profiles of pixel I, II, III, IV of the phase grating with discretized and continuous profile.

The efficiency of the continuous profile phase grating is only about 2 % higher than the stepped one, while the radius of each pixel is still conserved. Meanwhile, the simulation time of the phase grating with continuous profile is longer than the stepped one. Moreover, the stepped surface is easier to manufacture. So, it would be worth using the stepped profile for further simulation and fabrication.

3.3.6.3 Influence of the orientation of the phase grating

The phase grating's surface contains several vertical edges, as seen Figure 3-6. These structures can prevent the beam from shining on several parts of the surface at specific angles. This is why we investigate the influence of the orientation of the phase grating on the output beams.

The setup of the quasi-optical system is similar to the one shown in Figure 3-16. The phase grating is rotated around the z-axis with a step of 90 ° anti-clockwise. There are four positions: 0 °, 90 °, 180 °, and 270 °. The distance from the phase grating to the output plane is 300 mm.

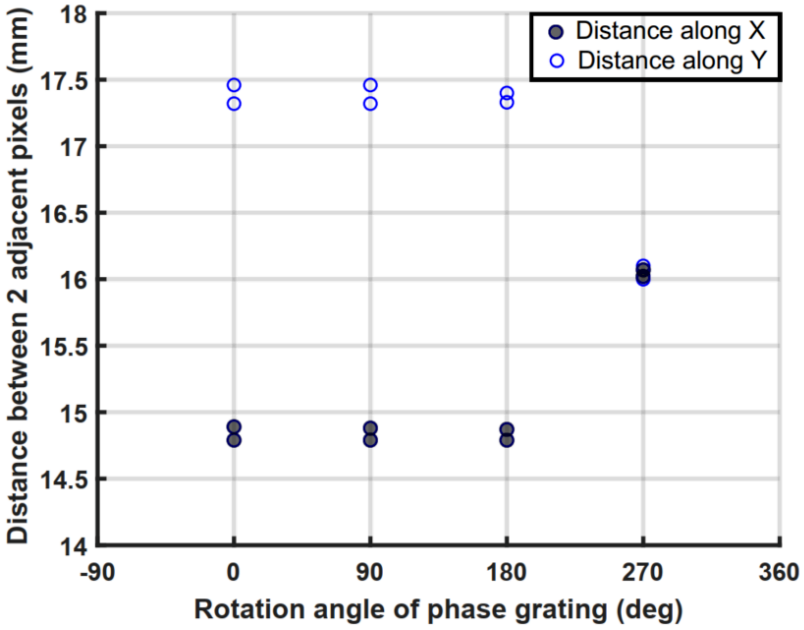

(a)

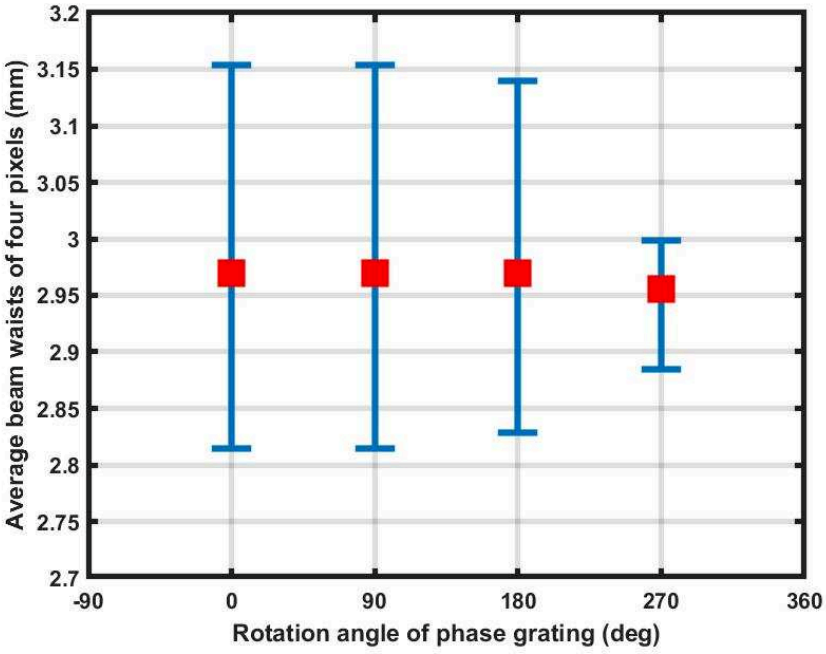

(b)

Figure 3-19. Influence of the orientation of the phase grating to the output beams. a) Distance between 2 adjacent pixels (mm). b) Average radius of four pixels at each rotation (with its variation range).

Figure 3-19a shows the distance between 2 adjacent pixels. Each rotation angle of the phase grating gives us four distances, where the distances along the X-axis are illustrated in black dots, and the distances along the Y-axis are illustrated in blue dots. Although four rotations of the phase grating all generate 4 pixels with a similar average distance between 2 adjacent pixels (16.0 ± 0.1 mm), only in the case of 270 °, four distances along X- and Y-axis are very close giving an array in a square form. In other cases (e.g. 0 °, 90 °, 180 °), the distances along Y-axis are always longer than the distance along X-axis.

The average radius of four output pixels (and its variation) at each rotation are shown in Figure 3-19b. The red dots show the average radius of the output beam pattern at each rotation. The error bars show the minimum and maximum simulated radius in each case. The rotation at 270 ° again gives us the lowest fluctuation of the radius of four pixels. The radius of the output pixels, in this case, stays around 2.95 mm.

Although the output beams at four rotation angles give the same efficiency (77 ± 1 %), the rotation of 270 ° of the phase grating provides the most homogeneous sub-beams in terms of variation of radius and distance between 2 adjacent pixels. Indeed, it proves that the phase grating's orientation can affect the output beams because several parts of the grating surface may be shadowed under the radiation from the THz source at certain rotation angles.

3.3.6.4 Influence of the incident angles of THz source

Our phase grating is designed when the incident angle of the THz source is set to 22.5 °. We would like to study the output pattern if the incident angle is slightly changed, to represent the case if the phase grating is misaligned in the experiment setup. In our case, we choose the angle at 15 °, 17.5 °, 20 °, 22.5 °, 25 °, 27.5 °, and 30 °. It should be noted that, in this case, the surface of the phase grating is permanently fixed. The setup is similar to that shown in

Figure 3-16, except for the incident angle α which is changed. Figure 3-20 shows the output beam pattern and beam profile of 4 pixels in 3 different cases: 15 °, 22.5 °, and 30 °, captured at a distance of 300 mm far away from the phase grating.

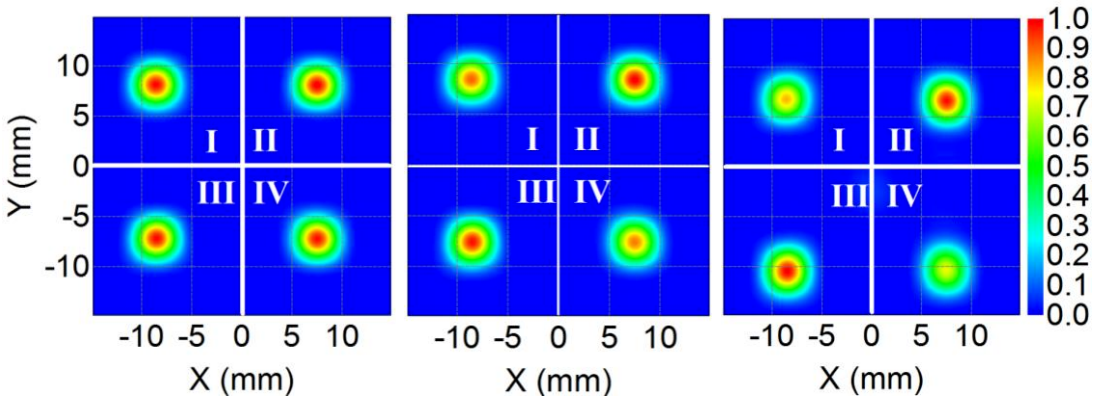

15 ° 22.5 ° 30 °

(a)

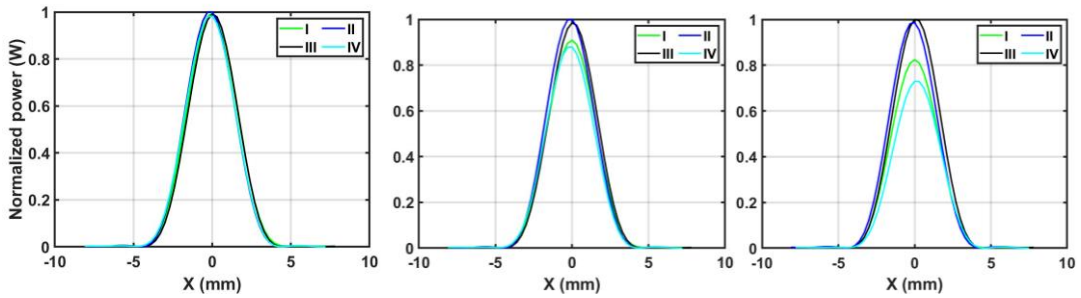

15 ° 22.5 ° 30 °

(b)

Figure 3-20. a) Output patterns at the distance of 300 mm from the phase grating when the incident angles are 15 °, 22.5 °, and 30 °. b) Beam profile of 4 pixels along the X-axis.

From Figure 3-20a, intuitively, when the incident angle changes, the output beams still keep the Gaussian shape, but the intensities of four beams vary, especially when we look at the changing of the normalised intensities of the incident angle (15 °), the power profiles of 4 pixels along the X-axis almost overlap. In comparison, with the broadest simulated angle (30 °), we can see a considerable difference in the amplitude of fourpixels. The smaller incident (or reflected) angle leads to the higher homogeneity of 4 beams. This is also shown in Figure 3-21a, where the efficiency of 4 output pixels at each input angle are illustrated in the circle, with the scale in left Y-axis. The lowest angle (15 °) of incident beam gives us the most homogenous efficiency of four pixels. Thus, the wider the angles, the higher the dispersion in terms of the efficiency of each pixel.

The total efficiency of 4 output pixels also decreases from 77.8 % to 73.4 % (shown by the red diamond symbol in Figure 3-21a with the scale shown on the right Y-axis) when the incident angle increases from 15 ° to 30 °.

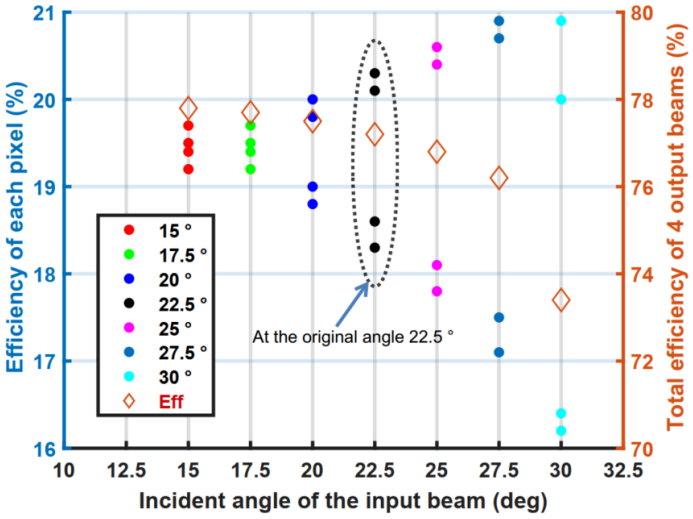

(a)

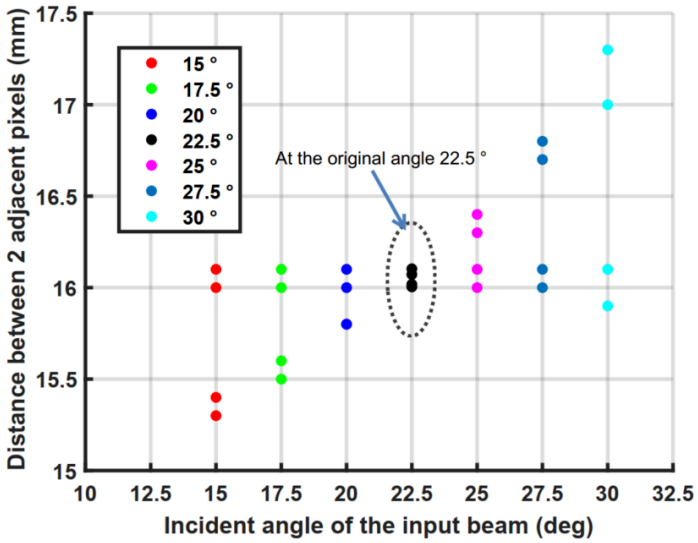

(b)

Figure 3-21. a) Total efficiency (diamond symbol with the scale on the right Y-axis) and efficiency of each output pixel (circle symbol with the scale on the left Y-axis). b) Distance between 2 adjacent beams at each incident angle.

The changing of incident angle also affects the distance between 2 adjacent beams, as shown in Figure 3-21b. When the angle gradually

increases or decreases from the nominal value of 22.5°, the variation of the distances gradually increases.

Therefore, a slight change in the incident angle can notably affect the average distance between 2 adjacent pixels and the efficiency homogeneity of four pixels, while still keeping the shape and radius of each pixel. Thus, we should be careful when setting up the experiment.

3.4 Mechanical design and fabrication

As presented in previous sections, the 2 x 2 beam phase grating surface is generated by the program MATLAB. For the manufacturing, we estimated the influence of machining tools. The surface geometry is first modified to adapt to the size of the milling cutter with a diameter of 0.1 mm and we fund that the divider efficiency is reduced around 4 %. Then to facilitate the machining, the grating structure has been discretized into 12 levels with a step of 10 µm along the axis perpendicular to the surface of the grating as shown in Figure 3-22. This structure has been simulated and analysed in the section 3.3.6.2.

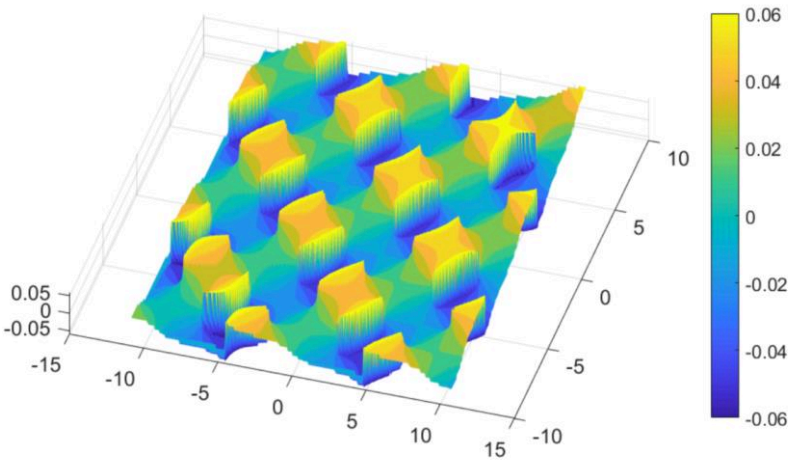

Figure 3-22. Discrete phase grating surface generated by the MATLAB program.

This surface geometry is used for final fabrication. The size of this grating is 20.0 mm x 21.6 mm, with the length on the Y being longer than the one on the X-axis because we consider the scaling of the oblique incident angle.

The phase grating is made of brass (an alloy of zinc and copper) and is surrounded by a circle with a diameter of 25 mm. A photograph of the manufactured prototype is shown in Figure 3-23.

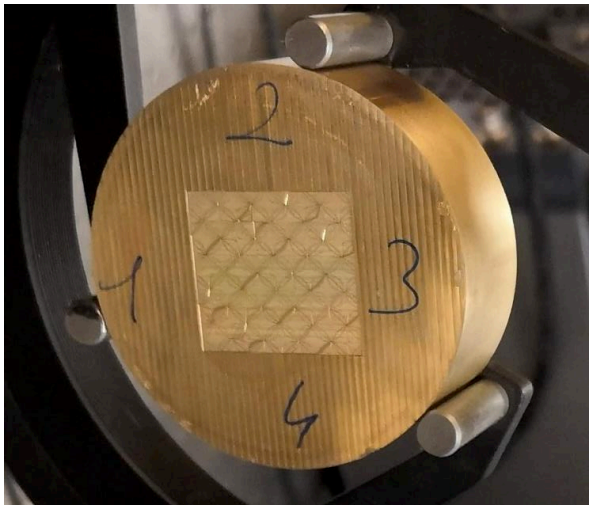

Figure 3-23. Fabricated phase grating.

3.5 Measurement of the beam divider and analysis

3.5.1 Experimental setup

The experiment setup to characterize the LO feeding system with the phase grating prototype is presented in Figure 3-24. The optical schema corresponding to the test setup is shown previously in Figure 3-4.

A Keysight RF signal generator is used to generate a signal at a few GHz with a power of 10 dBm which is multiplied up to 1.3 THz by the VDI AMC. The THz signal radiates through the horn of the AMC and reaches the phase grating after being reflected by the elliptical mirror. A QMC pyroelectric detector [51] is mounted in a 3-axis motion system with linear stages — which is monitored by a software written in Python — to capture the beam pattern at different positions of the optical path.

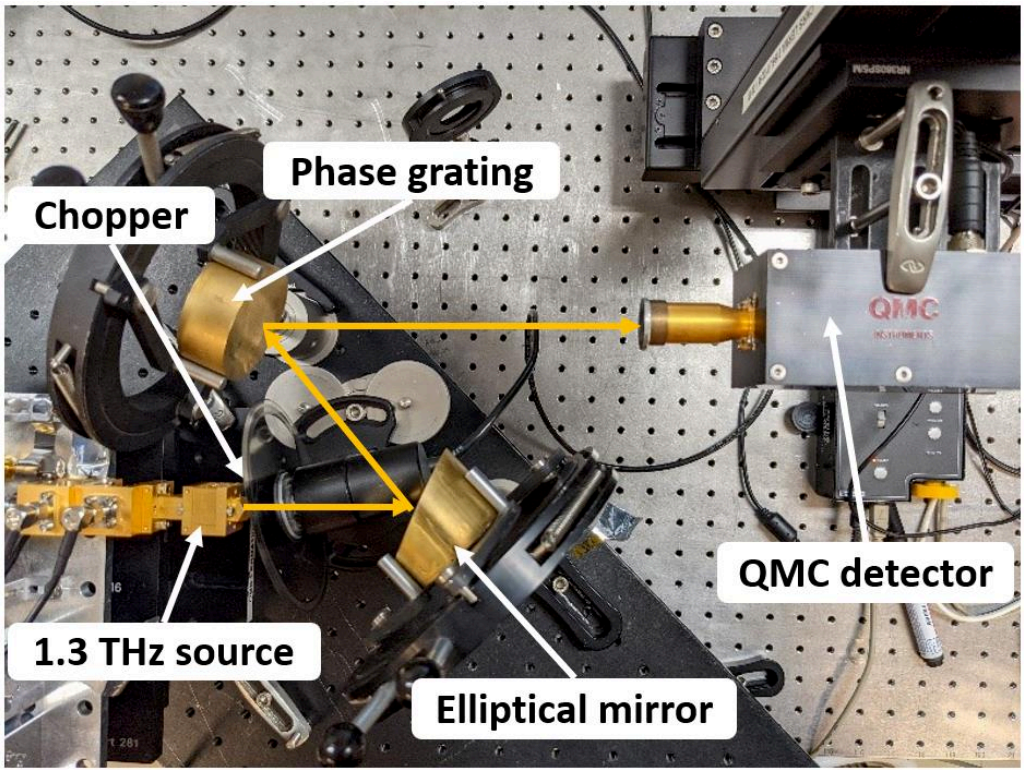

Figure 3-24. Quasi-optical system with the phase grating.

The measurements were performed in two steps. First, the QMC detector is placed at the location of the phase grating to measure the THz beam at the input of the divider. In a second step, the phase grating is inserted for the characterization of the LO feeding system as described by the optical schema (Figure 3-4), in particular of the beam properties around the output plane, or where will be installed the mixer array.

3.5.2 Beam pattern at the input of the phase grating

The measured pattern, together with the 2D Gaussian fit and the simulated pattern of the beam at the input of the phase grating are illustrated in Figure 3-25.

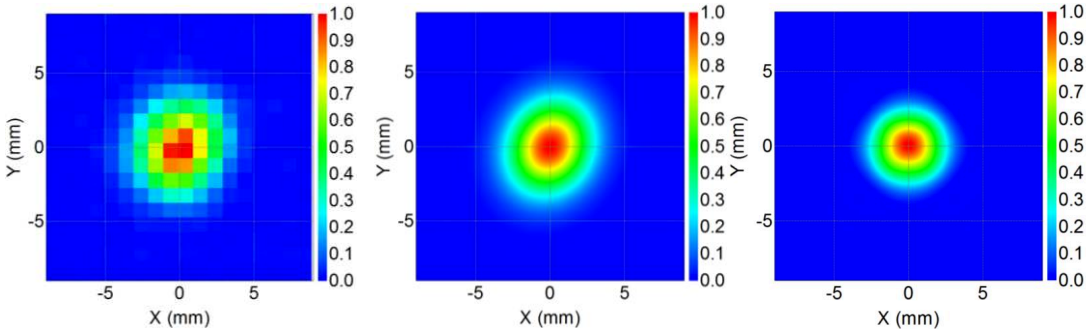

(a) (b) (c)

Figure 3-25. a) Measured beam pattern. b) 2D-Gaussian fit of the measured beam pattern. c) Simulated beam pattern. All of them are captured at a distance of 310 mm away from phase grating.

The beam profiles cutting through the highest intensity points of the normalised powers of the measured beam and the fitted Gaussian beam are shown in Figure 3-26.

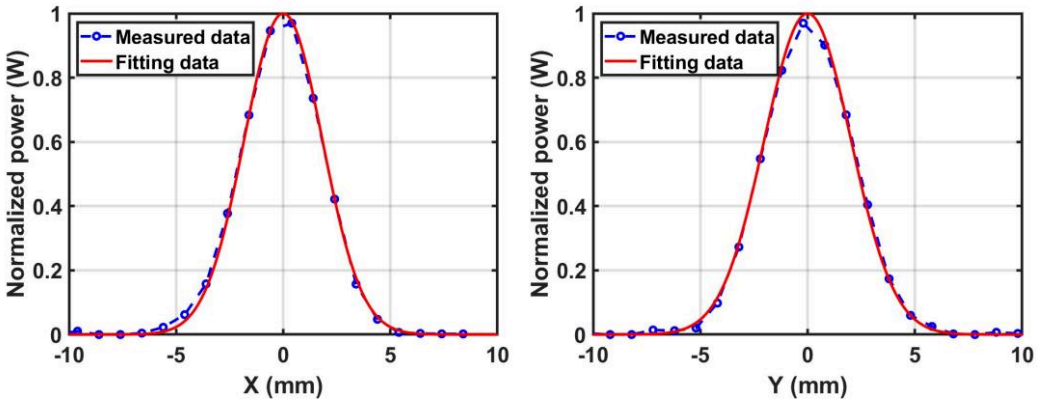

(a) (b)

Figure 3-26. Beam profiles of the measured pattern (dot-dash blue) and the 2D Gaussian fit of the measured pattern (solid red). a) Along the X-axis. b) Along the Y-axis

The measured beam profile looks similar to its 2D-Gaussian beam fit in Figure 3-26, both along the X- and Y-axis. Therefore, this fit is used to characterise the properties of the output pattern (e.g., the radius of the pixels, the efficiency).

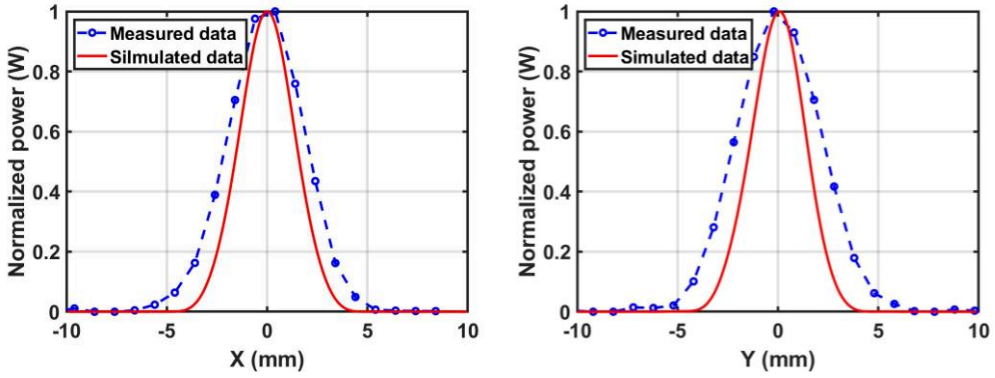

(a) (b)

Figure 3-27. Beam profiles of the measured pattern, 2D Gaussian fit of the measured pattern, and the simulated beam along the X- and Y-axis. a) Along X-axis. b) Along Y-axis

As we can see in Figure 3-25, the patterns of the measured output beams (not fitted and fitted) are larger than the simulated ones. This is confirmed in Figure 3-27. Indeed, the average of ω_1 and ω_2 in the simulated case is 3.0 mm, while the one in the measured cases is 4.0 mm. One of the possibilities causing the enlargement of the radius may be the large size of the pinhole of the pyroelectric detector (6 mm in diameter).

3.5.3 Influence of the aperture diameter of the Winston horn on the measurements

The measured beam waist is always larger than the simulated one, as seen in section 3.5.2. To understand the reason, we analyzed the effect of the receiver horn aperture on the measured beam width. As shown in Figure 3-24, a Winston horn [52] is used by the QMC detector to collect the radiation power and focus it on the sensor located at the end of the horn. This amount of energy will heat up the pyroelectric sensor which will generate a corresponding voltage. We think that the aperture diameter of the horn could have an effect on the amount of collected power and therefore on the response of the sensor.

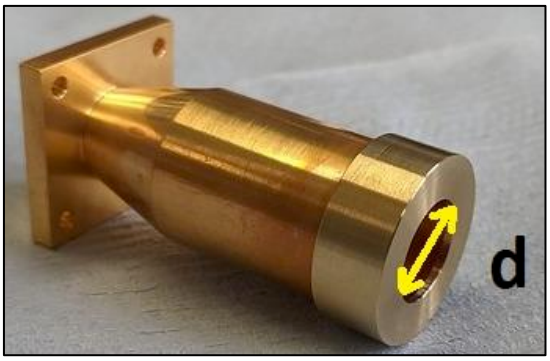

(a)

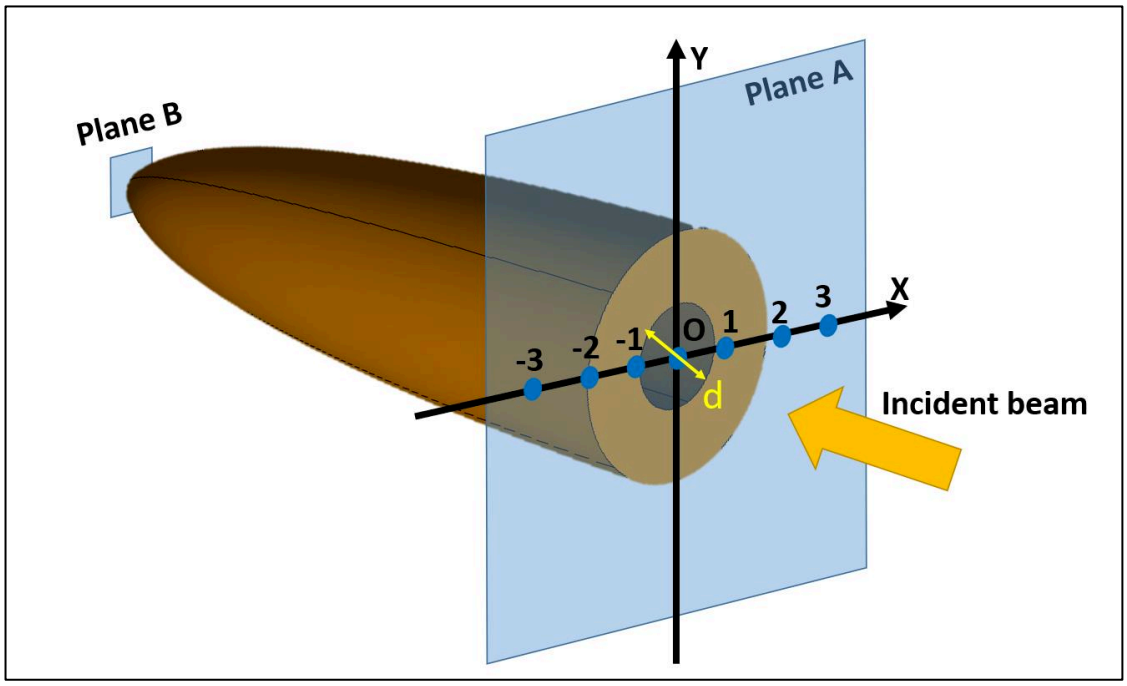

(b)

Figure 3-28. a) Winston horn of the QMC detector. b) Simulated Winston horn.

We simulated the THz source beam reflected by the elliptical mirror (the schema is shown in Figure 3-10) and seen by the Winston horn placed at the output plane. Figure 3-28b presents the simulated Winston horn which has similar dimensions to the one used in the measurement (Figure 3-28a). In the simulation, the aperture diameter d of the horn is varied between 2 mm, 6 mm (the aperture we used in the experiment), and 14.38 mm.

In Figure 3-28b, two planes should be distinguished: planes A and B. They are all perpendicular to the optical axis. Plane A is the plane where is the input of the horn, the distance from this plane to the elliptical mirror is 410 mm. Plane B is the plane at the bottom of the Winston horn where the measurement sensor is placed.

To simulate the beam pattern measurement, this horn is moved from the optical axis along the X-axis. At each position, we simulated the EM wave intensity distribution in the plane B formed by the incident rays travelling inside the horn. The amount of radiation power received by the horn and absorbed by the sensor can be represented by the integral of the wave intensity in this plane.

Figure 3-29 depicts the EM wave intensity distribution in the plane B for the horn with different aperture diameter and placed at different positions along the X-axis.

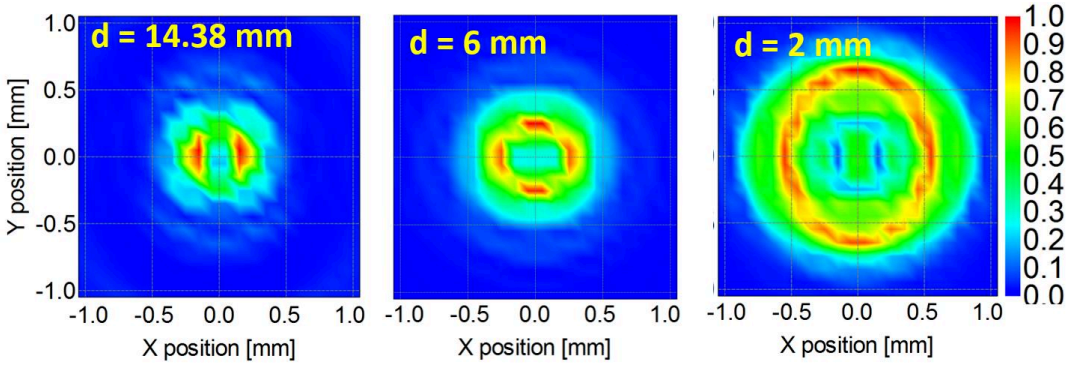

(a)

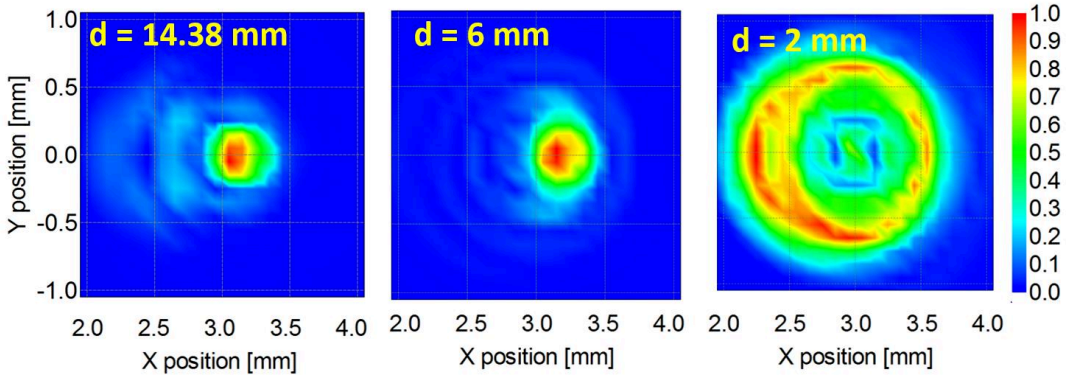

(b)

Figure 3-29. Simulated wave intensity distribution at the bottom of the Winston horn (plane B). a) Horn is placed on the optical axis and with different apertures. (b) Horn is shifted from the optical axis by 3 mm along the X-axis with different apertures.

As we can see in Figure 3-29, the power distribution at the bottom of the Winston horn varies with the aperture diameter and the position of the horn along the X-axis.

Indeed, as shown in Figure 3-30, a larger aperture of the Winston horn collects more energy than the smaller one. For example, in the case of the horn on the optical axis, the integrated power collected by the 6 mm aperture horn is nearly five times bigger than the one collected by the 2 mm aperture horn.

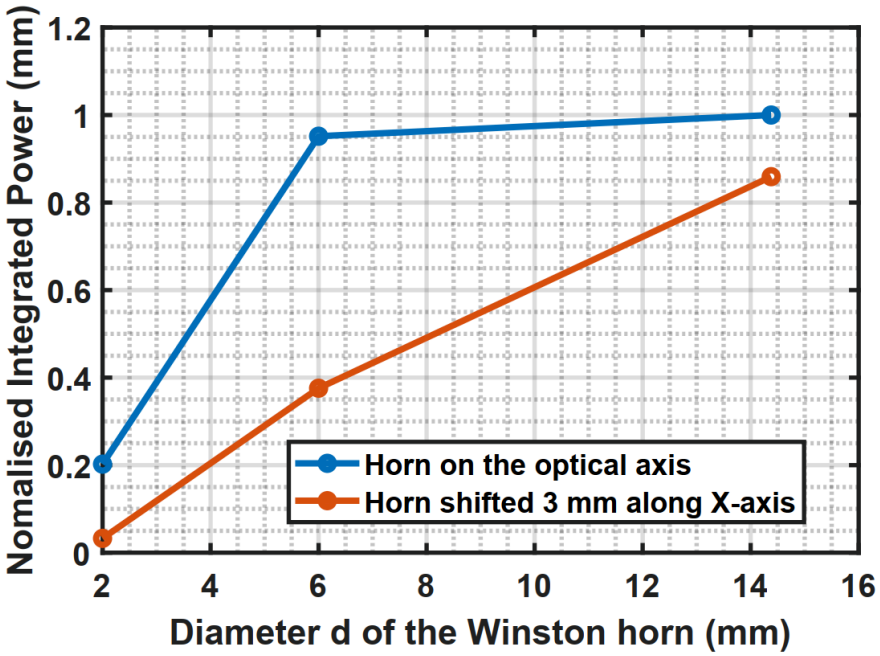

Figure 3-30. Normalised integrated power at each shifting point

To get the beam pattern of the source as seen by the sensor in the plane B, the integrated wave intensity at the bottom of the horn at each position and for different aperture of the horn is calculated and fitted with the Gaussian function. Figure 3-31 illustrates the simulated or measured beam profiles of the THz source. The markers are the simulated or measured points and the solid curves are the Gaussian function fitting.

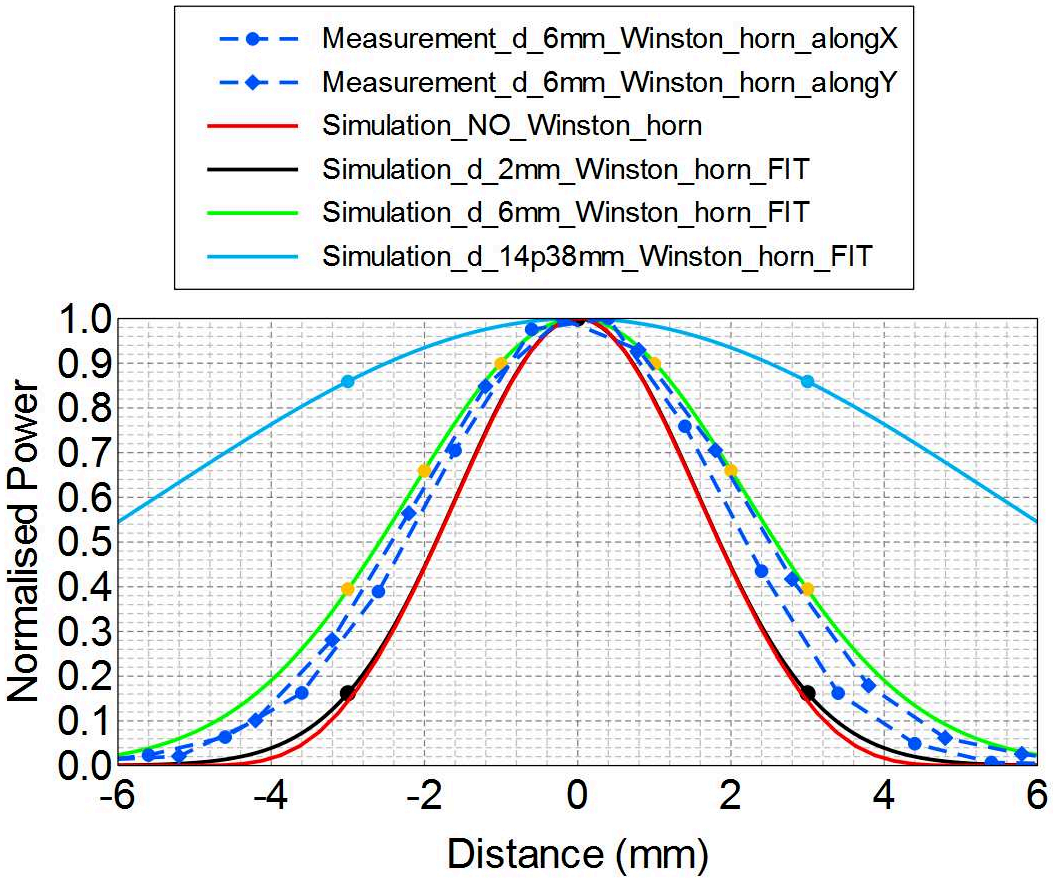

Figure 3-31. Beam profiles of the THz source beam after the elliptical mirror (on the plane A). Makers are measured or simulated points.

The radius of the beam profile simulated with the Winston horn is always larger than the one without the horn. Moreover, the larger the aperture diameter of the horn, the larger the radius of the beam profile. Indeed, the simulated beam waist radius are 3.1 mm, 4.4 mm, and 10.9 mm in case the input diameters of the Winston horn are 2 mm, 6 mm, and 14.38 mm, respectively.

The beam waist of the simulated beam profile with a 6 mm aperture horn is slightly larger than the one measured with the same aperture: 4.4 mm compared to 4.0 mm. It is closer to the measurement result compared to the simulation done without the horn where the calculated beam waist is 3.0 mm.

The radius of the simulated beam profile using a 2 mm aperture Winston horn seems very close to the simulated one without horn, indicating that the use of a Winston horn with an aperture diameter smaller than 2 mm may help to reduce the influence of the horn on the measurement result.

In conclusion, we proved by simulation that the Winston horn's aperture diameter can strongly affect the measured beam pattern. In particular, the beam width of the radiation power collected by the horn can increase with the horn's aperture diameter.

3.5.4 Beam pattern at the output of the phase grating

3.5.4.1 Unwanted output signal

After measuring the beam characteristics at the location of the phase grating, the QMC detector is replaced by the grating and is moved to the output plane (mixer array plane) of the system as shown in Figure 3-24.

A phenomenon we met at the beginning of the experiment is that except the expected four divided beams, a relatively high intensity cloud appears at the centre of the 2D beam pattern measured by the QMC detector (as shown in Figure 3-32a).

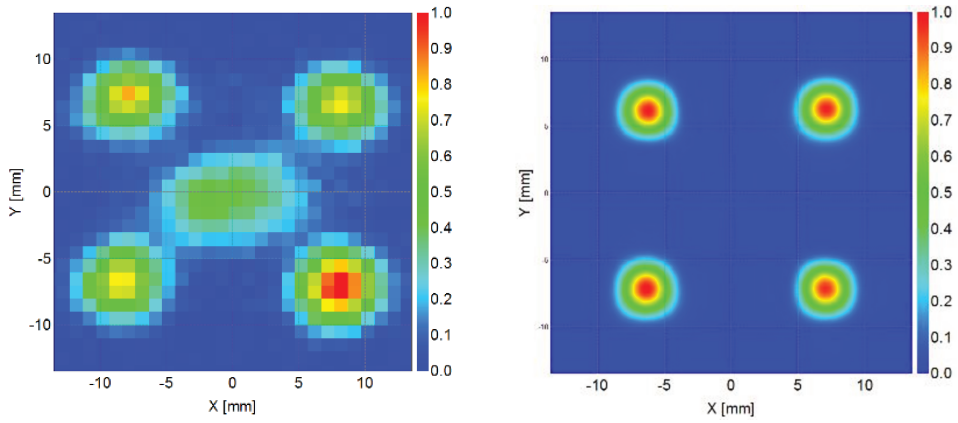

(a) (b)

Figure 3-32. a) Measured output beam pattern, where the central beam appears. b) Simulated output beam pattern without the central beam.

This is abnormal because there should be no signal power in the central part as given by the simulation (Figure 3-32b). I doubt that the circle part around the phase grating—which helps to mount the phase grating into the holder—could cause this problem. To prove that, the phase grating with its surrounding circle part is simulated, as shown in Figure 3-33a. The simulation result is shown in Figure 3-33b.

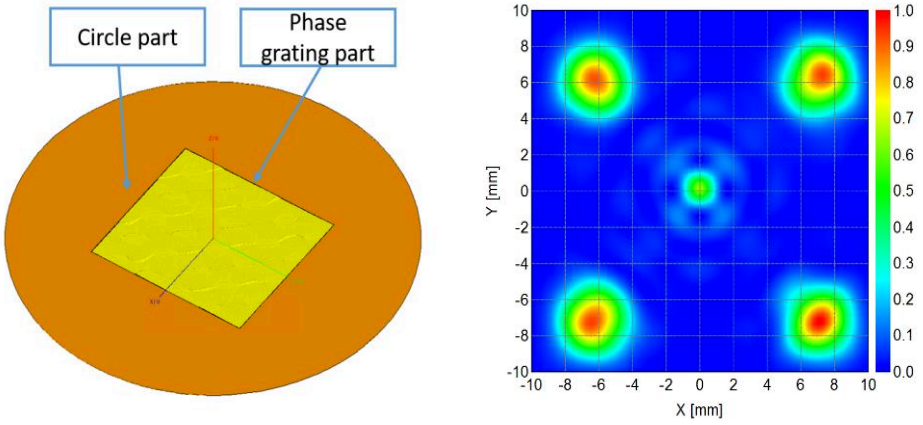

(a) (b)

Figure 3-33. a) Model of a phase grating with the circle part. b) Simulated beam pattern with the appearance of the central beam.

The simulation shows the similar appearance of signal power in the centre part as in the measurement. To check that, we covered the circle part of phase grating by a THz absorber, as shown in Figure 3-34a. The measured output beams from the covered phase grating are shown in Figure 3-34b. The signal power at the centre of four pixels no longer exists, confirming my simulation in Figure 3-33. The fact that we can reproduce the unexpected measurement problem by simulation, demonstrates the availability of our 3D simulation model.

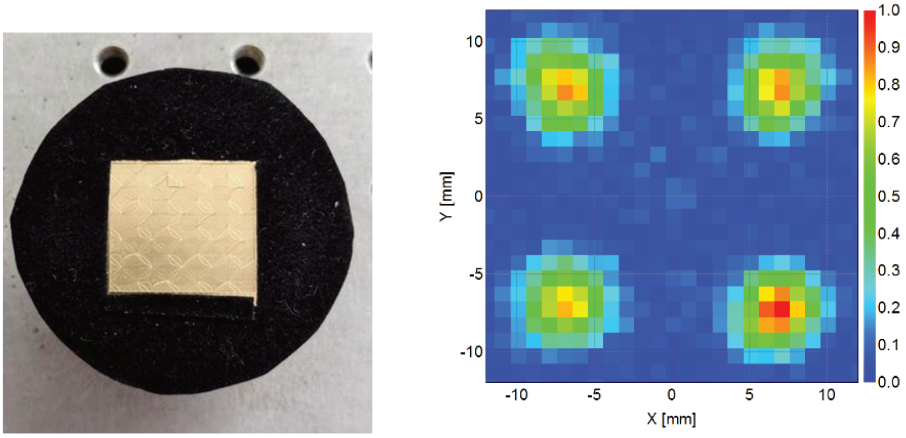

(a) (b)

Figure 3-34. a) Fabricated phase grating with the absorber (the size of phase grating is 20 mm x 21.6 mm). b) Measured output beam of the phase grating with the absorber.

So, we should be careful when fabricating the phase grating with the metal part around. It should be minimised or be covered with the THz absorber to avoid unexpected power distribution. For this study, we keep the absorber in all measurements.

3.5.4.2 Measured 4 output beams and comparison with the simulation

The output pattern is measured at a distance of 310 mm far away from the phase grating. The normalised power of the measured pattern, the 2D Gaussian fit of the measured pattern, and the simulated pattern are illustrated in Figure 3-35.

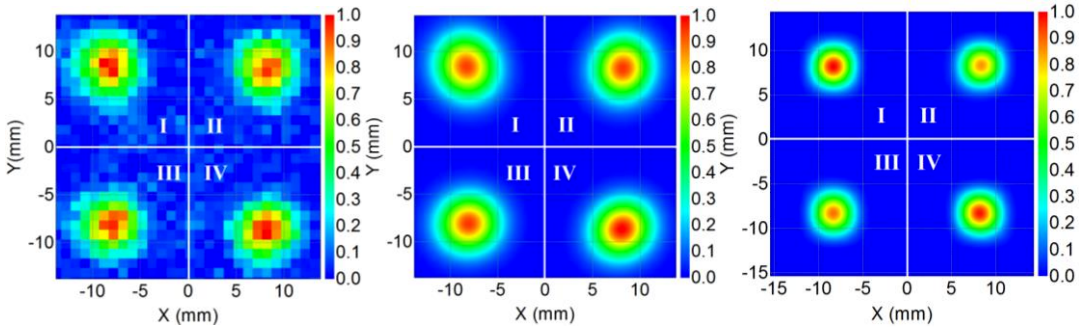

(a) (b) (c)

Figure 3-35. a) Measured beam pattern. b) 2D Gaussian fits of the measured beam pattern. c) Simulated beam pattern. All of them are captured at a distance of 310 mm away from phase grating.

First, the measured data is fitted with the 2D Gaussian function to check if the measured beam is close to Gaussian beam. The beam profile of the measurement and the fitting of each pixel cut through the highest intensity points are compared along the X- and Y-axis.

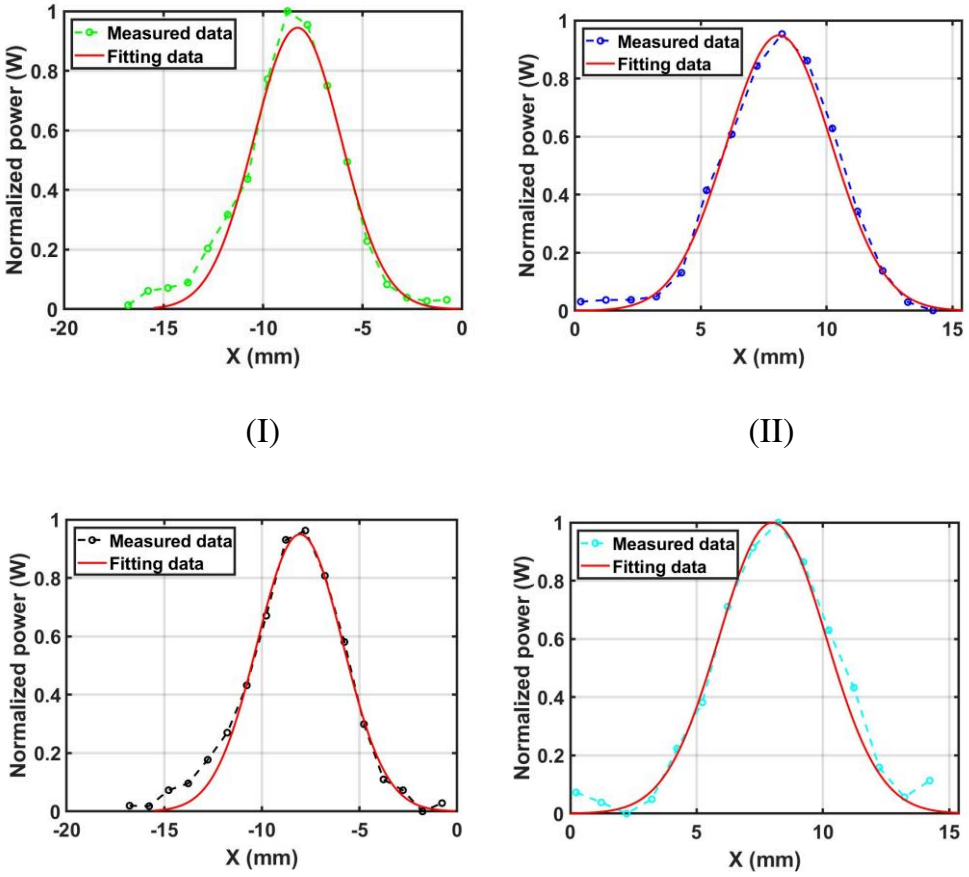

Figure 3-36. Measurement and fitting of the beam profile cut through the highest intensity point of pixel I, II, III, and IV along X-axis

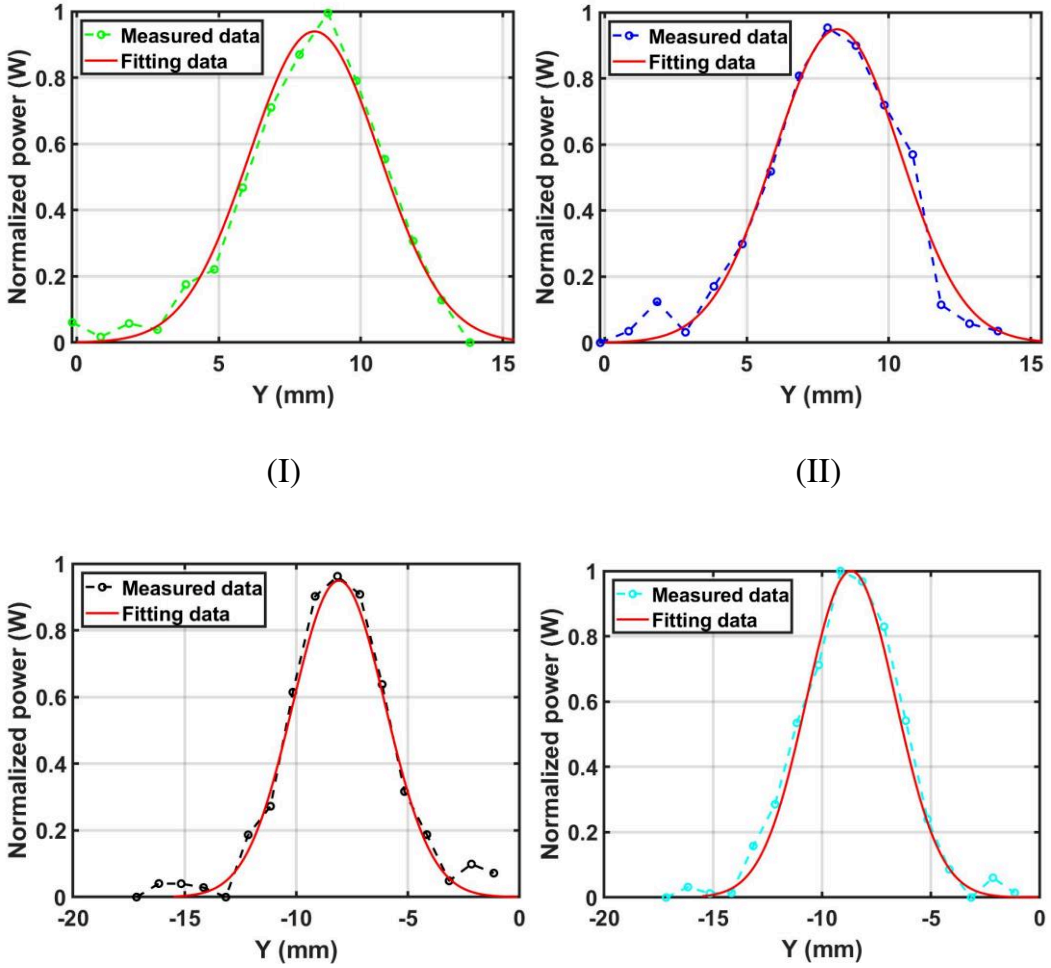

Figure 3-37. Measurement and fitting of the beam profile cut through the highest intensity point of pixel I, II, III, and IV along the Y axis

Intuitively, as shown in Figure 3-35 to Figure 3-37, the measured beam profile is close to the Gaussian fit for all 4 pixels, both along the X-axis and Y-axis, permitting us to use the fit data to further characterise and compare the properties of the output beam patterns of 4 pixels.

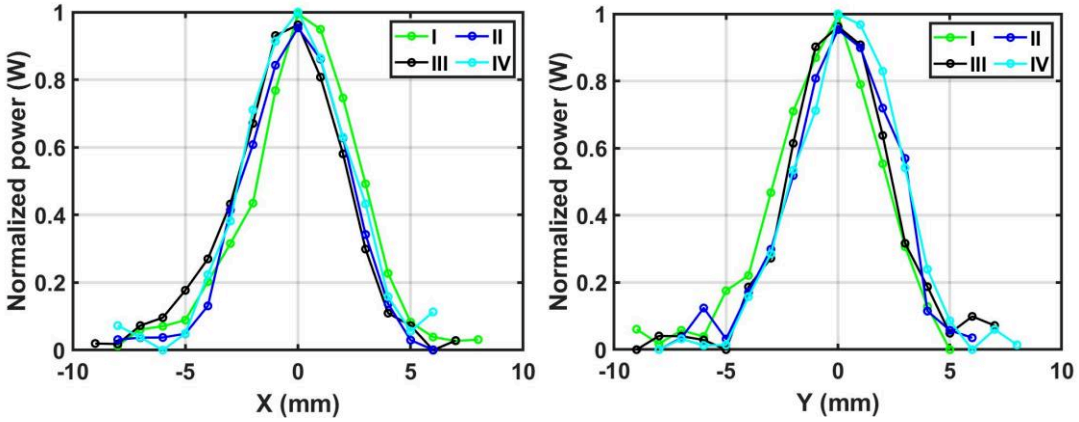

(a1) (a2)

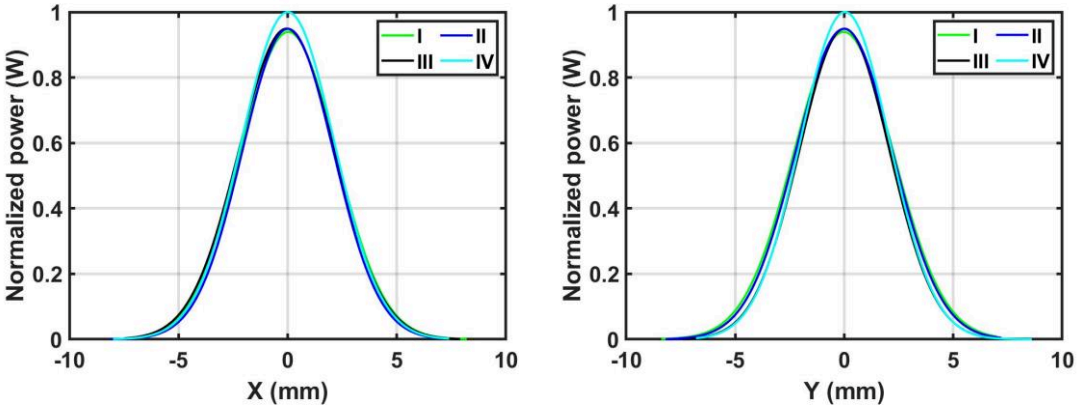

(b1) (b2)

Figure 3-38. Beam profile of 4 output beams along the X- and Y-axis at a distance of 310 mm far away from phase grating.

a1) Measured data along the X-axis. a2) Measured data along the Y-axis.

b1) Fitting data along the X-axis. b2) Fitting data along the Y-axis.

In Figure 3-38, the measured beam profiles of 4 pixels are relatively homogeneous along X- and Y- axis, with only a little bit difference in the highest intensity (6 %). The fitting data also shows that each pixel's radius along the X- and Y-axis overlaps. Each pixel takes 17.5 - 19 % input power.

The average radius of four measured beams is 4.2 mm (with the values varying from 4 mm to 4.7 mm). This value is larger than the simulation one without taking into account of the Winston horn (3.1 mm). As mentioned in section 3.5.3, we demonstrated by simulation that the Winston horn's input diameter can affect the beam waist size of the output beam pattern. Therefore, if we consider the effect of the 6 mm diameter Winston horn, the average radius of 4 beams in simulation should be 4.4 mm (calculated by simple linear estimation based on section 3.5.3), which is close to the measurement one (4.2 mm).

Then, the measurement data and the fitting data of the measurement at the same distance (310 mm far away from the phase grating) are compared to the calculated data of a Gaussian beam with a beam waist radius of 4.4 mm. The normalised beam profiles, obtained by the measurement, the Gaussian fitting and the calculation, cutting through the highest amplitudes of four pixels along the X- axis are shown in Figure 3-39. It shows a good agreement between measurement and simulation in terms of Gaussian shape and beam waist radius.

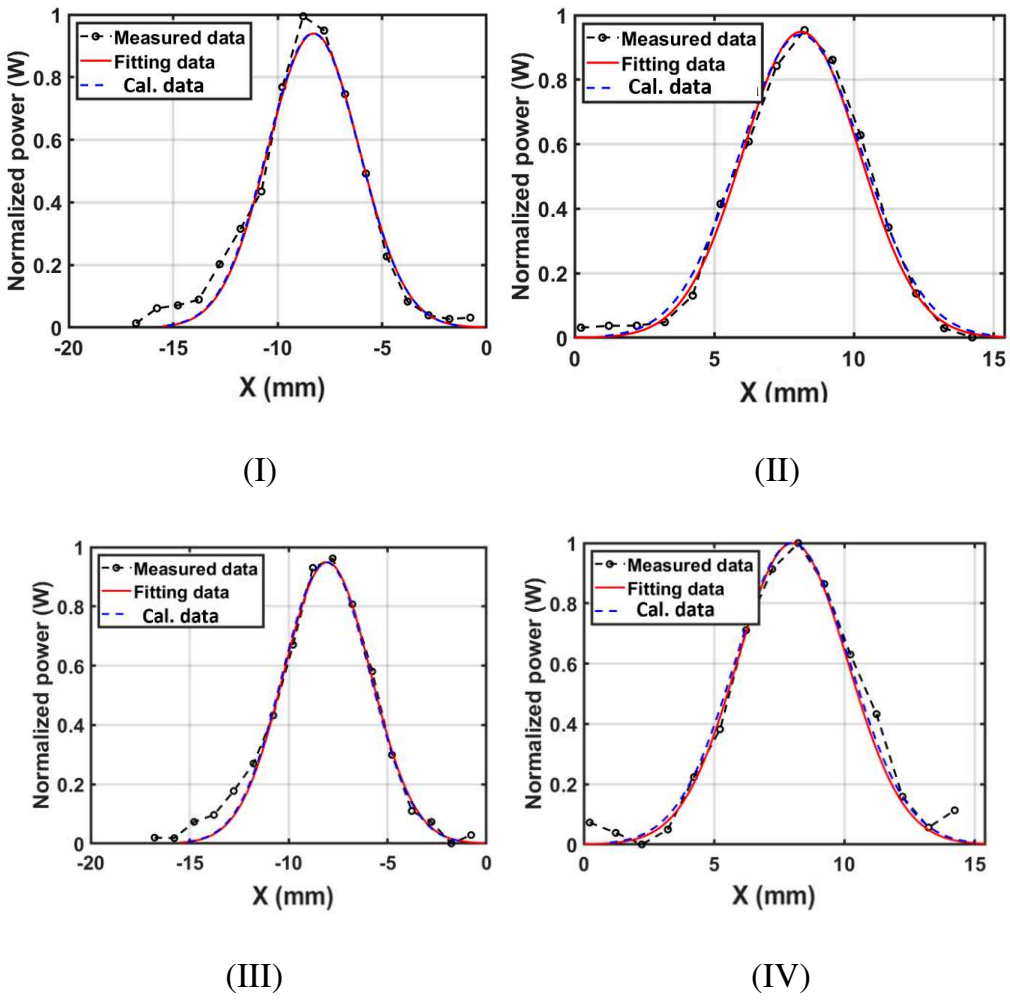

Figure 3-39. Measured and simulated beam profiles together with the 2D Gaussian fits of the measurement of 4 pixels (I, II, III, and IV) along the X - axis

In conclusion, the measurements of the output beams fit well with the simulations. The measured beams have Gaussian shapes with good homogeneity. The efficiency of fabricated phase grating is 72 %, which is comparable to previous studies [36][53][54]. This result drops 6 % compared to the simulation. The average distance between two adjacent pixels is 16.8 mm in measurement, which is very close to the simulated one (16.5 mm). The average radius of pixels in measurement is 4.2 mm, which is close to the simulation (4.4 mm) when considering the Winston horn's effect.

3.6 Global phase gratings with higher number of output pixels

The MATLAB code to design Global phase grating was developed previously in our lab based on the algorithm shown in Figure 3-3 [37], [55]. Based on that, I have improved it. First, an interface is added, so we can quickly choose and change the input parameters. Then we can generate phase grating with an arbitrary number of output pixels, with the total number of pixels smaller than sixteen. The distances between 2 adjacent pixels can also be chosen arbitrarily.

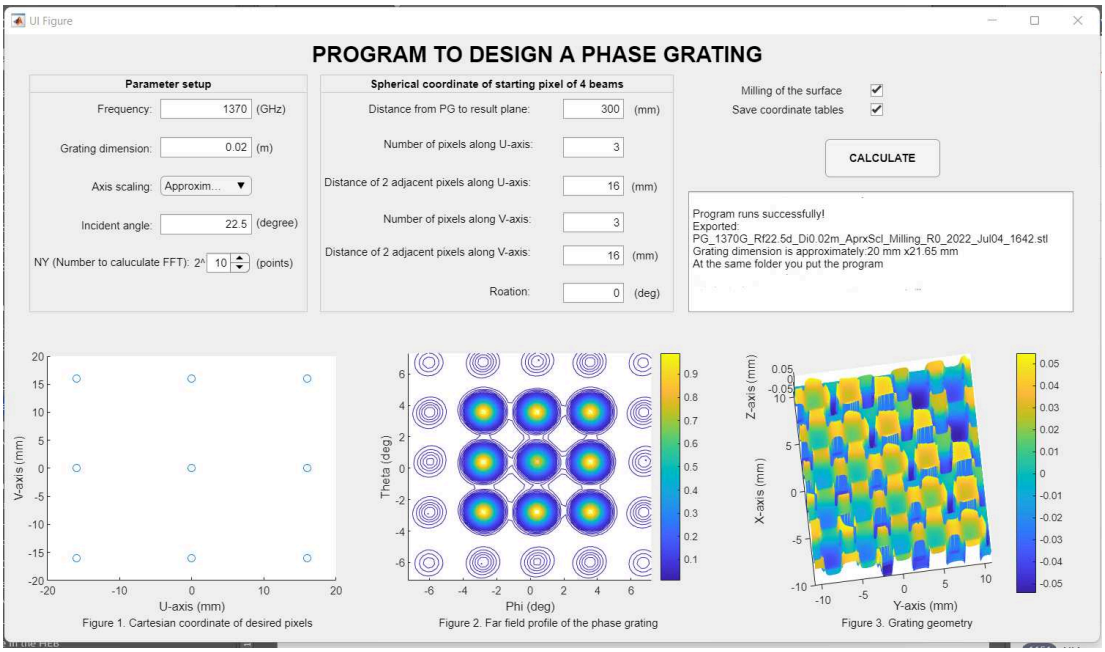

Figure 3-40. Program to calculate the surface of phase grating

Using the interface in Figure 3-40, several phase gratings are calculated. I show the phase grating of 2 x 4 (Figure 3-41) and 3 x 3 beam phase grating (Figure 3-42) working at 1370 GHz. The distance between two adjacent pixels is 16 mm. The phase grating size is 20 mm x 21.6 mm. The setup used in the simulation is the same as in Figure 3-16.

Figure 3-41 shows the surface and output beam pattern of the 2 x 4 beam phase grating.

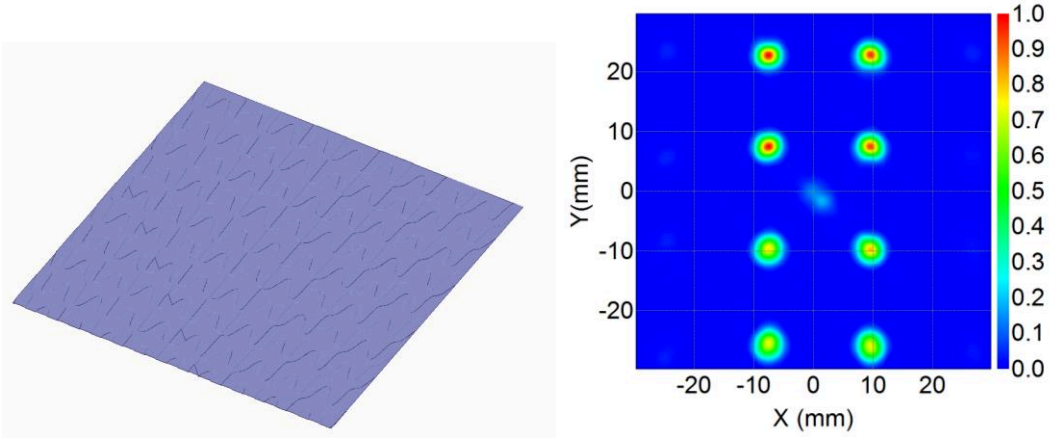

(a) (b)

Figure 3-41. Surface which can generate 2 x 4 pixels at 1.3 THz. a) Phase grating's surface with a size of 20 mm x 21.6 mm. b) Normalised intensity of the output pattern at the plane 400 mm far away from the phase grating.

The output beams in Figure 3-41b have Gaussian beam shapes. The ratio between minimum and maximum intensity of the highest amplitude point of 8 pixels is 73.1 %.

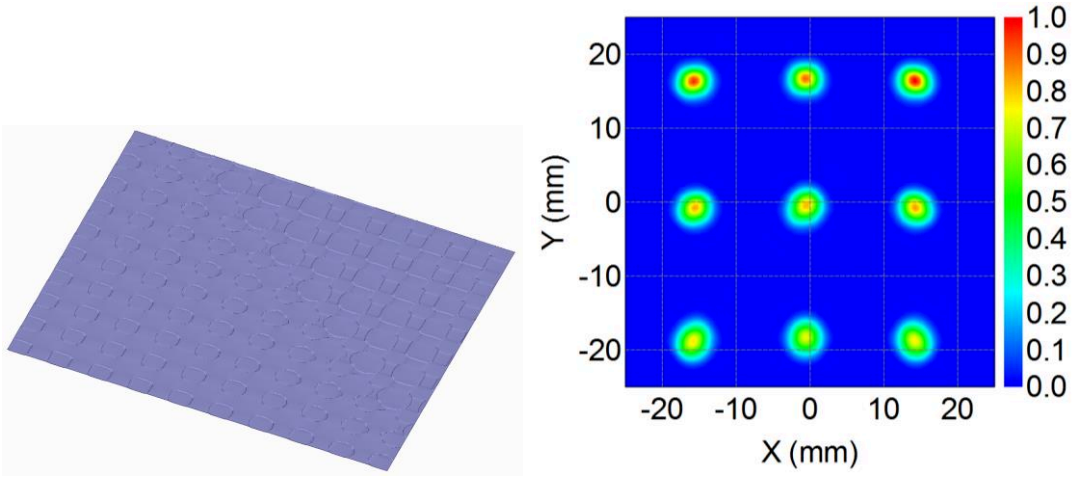

(a) (b)

Figure 3-42. Surface which can generate 3 x 3 pixels at 1.3 THz. a) The phase grating's surface with a size of 20 mm x 21.6 mm. b) Normalised intensity of the output pattern at the plane 400 mm far away from the phase grating.

The phase grating in Figure 3-42a can generate 3 x 3 beams with Gaussian beam shape. The ratio between minimum and maximum intensity of the highest amplitude point of 9 pixels is 74.0 %.

Chapter 4. Investigation of HEB mixer IF impedance

4.1 Introduction

As discussed in Chapter 1, the IF impedance is an essential parameter for the development of HEB mixers. From a theoretical perspective, knowing the IF impedance of HEB mixer can contribute to a deeper understanding of its working principle, and help to calibrate and improve its physical model. From a practical perspective, we can build an impedance matching circuit between HEB and LNA of the IF subsystem if their impedances are all identified. This circuit can help avoid mismatching from the output of the HEB to the input of the LNA to reduce the noise temperature and enlarge the IF bandwidth as much as possible. This circuit can also substitute the isolator between HEB mixer and LNA commonly used to avoid the mismatching, makes easier the integration of a receiver system for the building of multi-pixel receivers.

Several groups have tried to characterize the NbN HEB's IF impedance at the operating points (with optimal LO pumping level and DC bias) so far [22], [25], [26], [56], [57]. However, each way has advantages and disadvantages, which will be explained in section 4.3.1. The crucial challenges are to find the appropriate calibration process and accurate standards for, finally, getting the actual HEB mixer's IF impedance at the cryogenic temperature while we perform the measurement at the input of the cryostat. Between HEB mixer and the connector of the cryostat, there are cryostat cable, bias T, IF circuitry inside the mixer block. All these components significantly contribute to the measurement results. We can measure the cryostat cable and

bias T without difficulties at room temperature, but it is much more challenging to get their accurate characteristics at low temperature (around 4 K). Meanwhile, it is not easy to measure separately the IF circuitry inside the HEB block.

Throughout this chapter, we will present a specific approach that we adopted to extract the impedance of HEB mixer under its operating conditions.

4.2 HEB mixer block and its 3D IF circuitry model

Our goal is to establish a trusting 3D model of HEB block to better understand the HEB's IF circuitry. This model will be used to simulate the properties of the IF circuitry because it is not possible to measure it directly.

4.2.1 HEB mixer block

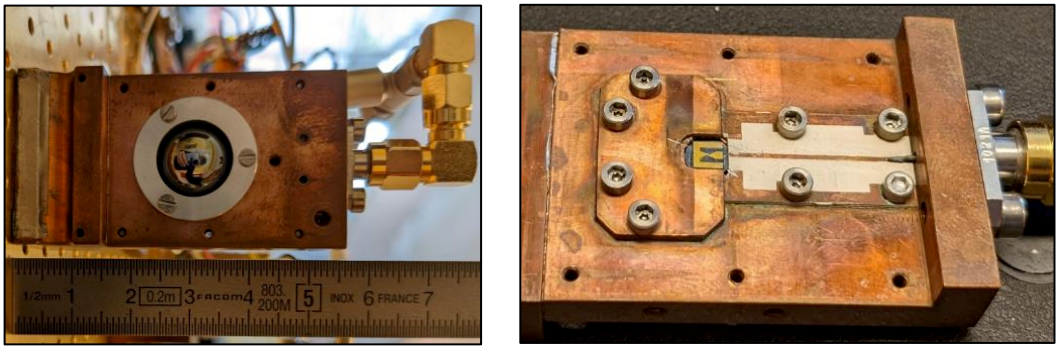

(a) (b)

Figure 4-1. HEB mixer block. a) External view. b) Inside of the block.

The external view of the mixer block is shown in Figure 4-1a, and its inside is shown in Figure 4-1b. This block contains a silicon lens to focus the LO and RF signal to a planar antenna connected to the HEB. The lens has a radius of 6.35 mm, and is fixed to the metal structure. HEB is glued at the back of the Si lens. Both substrate of HEB and lens are made from Si to avoid reflections

between them. The output of the HEB is connected to the microstrip line of the IF circuit by wirebonds. The microstrip line is made from RT/Duroid 6010LM material [58], with the dielectric constant $\varepsilon_r = 10.2$. The thickness of the dielectric is 0.635 mm, and the thickness of metal cladding is 18 µm.

The HEB mixer used in this work is shown in Figure 4-2. The microbridge is made from NbN and has a thickness of around 5 nm deposited on a silicon substrate. The size of the NbN bridge is 0.2 µm long x 2.2 µm wide.

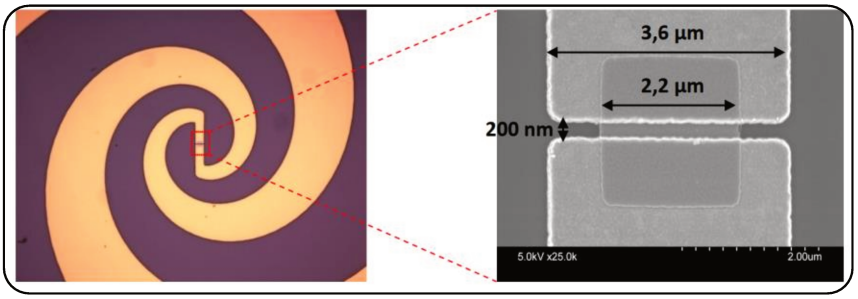

(a) (b)

Figure 4-2. a) HEB and its spiral antenna fabricated in our lab. b) SEM image of an HEB.

The RF and LO signals are coupled to the HEB mixer by the antenna [16]. Several kinds of antennas can be used, for instance, log-spiral, dipole, slot, bow-tie, and log-periodic. Each type of antenna has different bandwidths, impedances, and cross-polarization. Figure 4-2 shows a photograph of the log-spiral antenna with the NbN HEB used in our experiments. This antenna can couple both linear and circular polarization radiations. It can work at a wide frequency range from 100 GHz - 1400 GHz [16].

4.2.2 IF circuitry model at room temperature

4.2.2.1 IF circuitry model of the testblock

To construct a 3D model of the HEB block, we have built a special test block similar to the mixer block, then measured and simulated its reflection coefficient. Figure 4-3a shows this test block terminated with a resistor. The reason we use the testblock is that we can quickly change the component soldered at the end of the microstrip line. We can also easily measure its reflection coefficient at room temperature to check the simulation model. The resistors with different values (50 Ω and 20 Ω) have been used, and connected to the microstrip line by wirebonds. Then, a 3D model is constructed (Figure 4-3b), including all the concerned elements such as resistor, wirebond, microstrip line, via hole, and space. The simulation of this 3D model is performed with the software FEKO [40].

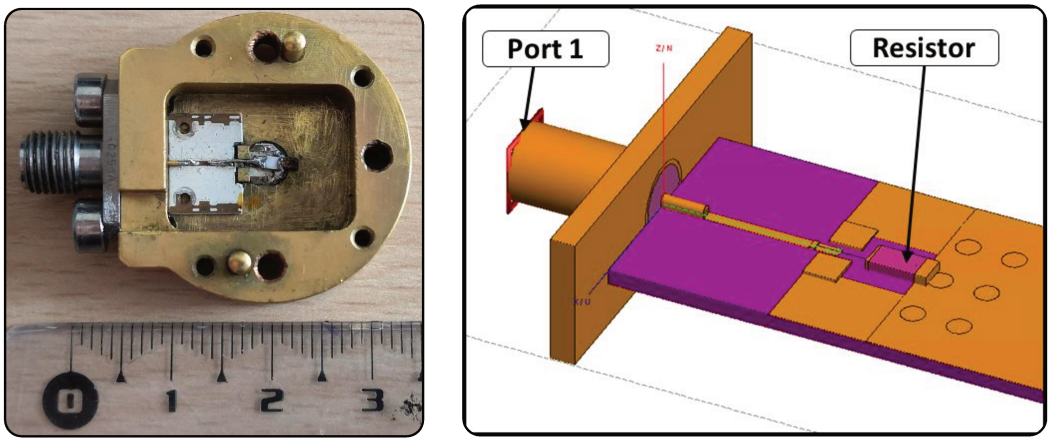

(a) (b)

Figure 4-3. a) Photograph of the testblock terminated by a resistor. b) Testblock model.

S-parameter measurement is performed with a vector network analyzer (VNA). The impedance of the test block is calculated by

$$Z_{Load} = Z_0 \frac{1 + S_{11}(\omega)}{1 - S_{11}(\omega)} \qquad \textit{Equation 44}$$

with $S_{11}(\omega)$ is the reflection coefficient, $Z_0 = 50\ \Omega$.

The measured and simulated impedance of the testblock are shown in Figure 4-4 (terminated with a 50 Ω resistor) and Figure 4-5 (terminated with a 20 Ω resistor).

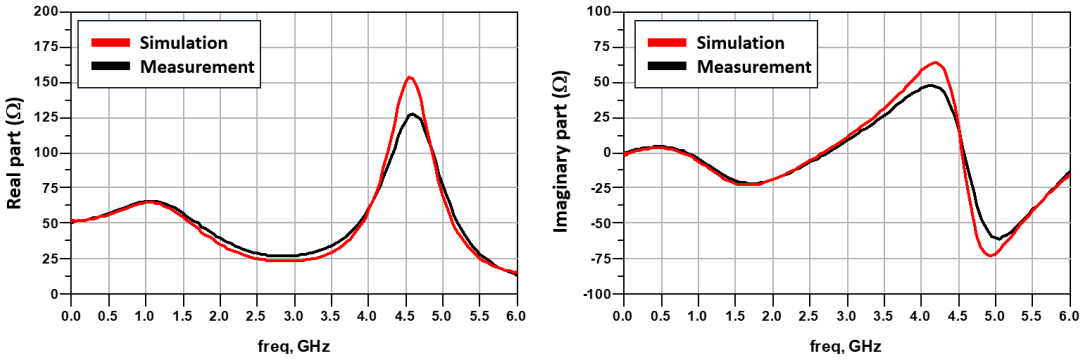

(a) (b)

Figure 4-4. Measured and simulated impedance at the SMA connector of the testblock with 50 Ohm resistor at room temperature. a) Real part. b) Imaginary part.

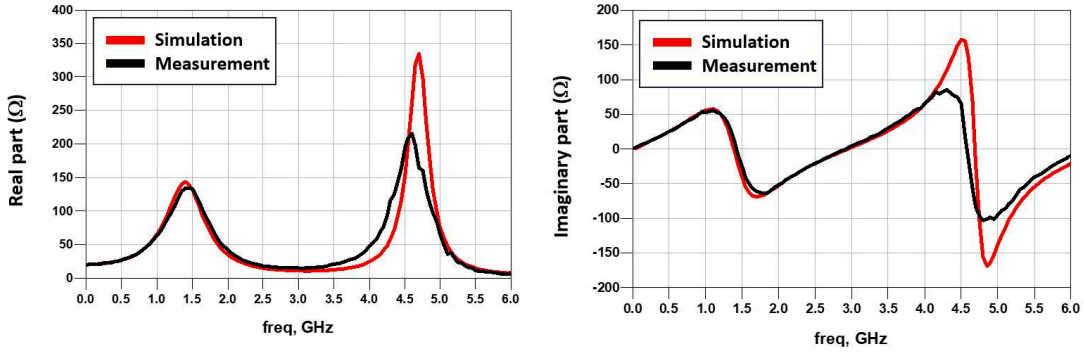

(a) (b)

Figure 4-5. Measured and simulated impedance at the SMA connector of the testblock with 20 Ohm resistor at room temperature. a) Real part. b) Imaginary part.

In both cases (50 Ω and 20 Ω terminated resistors), the measured and simulated impedance (real and imaginary parts) almost overlap over the frequency range from 0 to 3.5 GHz. After 3.5 GHz, although the simulated

impedances still have the similar shape as the measured one, the values do not overlap. This can be explained by the characteristics of the resistors. In the simulation, we set the resistor with constant real values. Meanwhile, the kind of resistor we used in the experiment is not calibrated in high frequencies and it contains parasitic inductance and conductance. When the frequency is higher than 3.5 GHz, these inductance and conductance could be big enough to affect the measurement and cause the difference with the simulation [59]. Therefore the testblock model can be accepted as a reference to build the actual model of the HEB block.

4.2.2.2 IF circuitry model of the HEB block

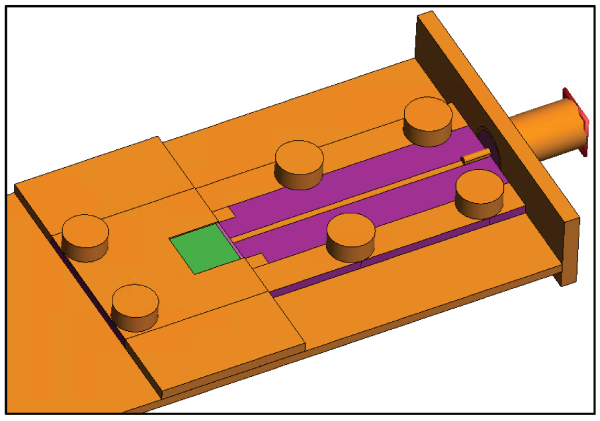

Figure 4-6. 3D EM model of the HEB block.

Using the knowledge obtained from testblock, the 3D EM model of the IF circuitry of the HEB block is built (Figure 4-6), mimicking the fabricated circuit (Figure 4-1). This model will be used to investigate the behaviour of the HEB block, and get the 2-port S-parameter of the IF circuit located between the SMA and the ending of the microstrip line.

4.3 Measurements and extraction of the reflection coefficient of HEB mixer

4.3.1 Calibration planes

To be able to characterize the HEB's IF impedance with accuracy, a good calibration process is essential. Figure 4-7 shows the possible reference planes for the calibration:

- Ref. plane 1 at the input of the cryostat.
- Ref. plane 2 at the beginning of the IF circuitry (or the SMA connector of the mixer block).
- Ref. plane 3 at the ending of the microstrip line (at the beginning of the wirebond connected to HEB).
- Ref. plane 4 at the level of the HEB bridge.

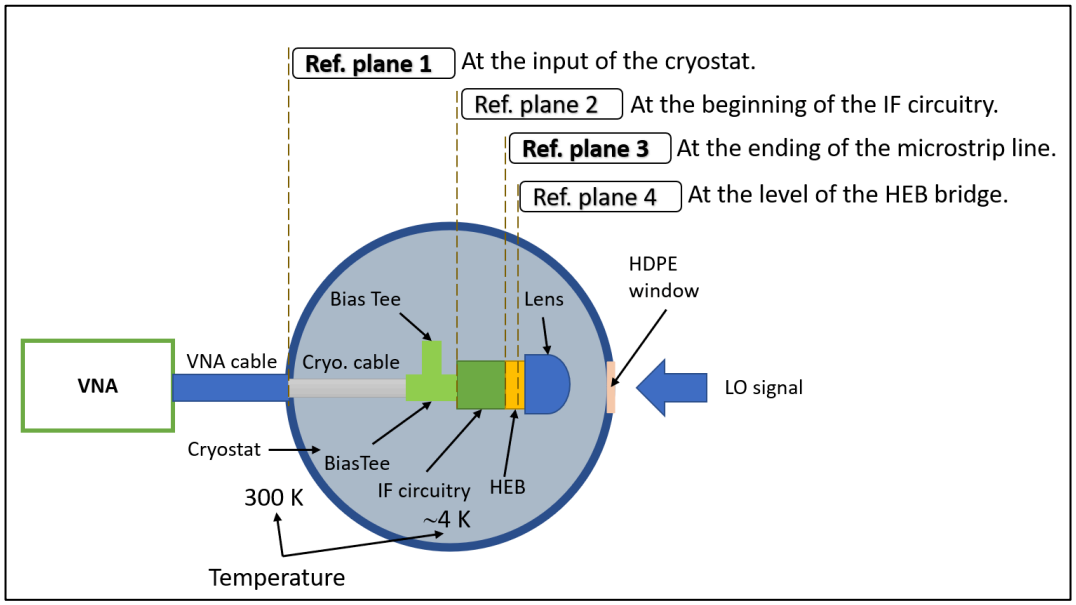

Figure 4-7. Reference planes for the measurement of the reflection coefficient of the HEB mixer at cryogenic temperature.

In the papers of J. W. Kooi [26], [29], they calibrated at the input of the cryostat (Ref. plane 1). The 3D IF circuit is simulated. Bias T is supposed

not to change its properties over the temperature range. The de-embedded technique is used to get the impedance of the HEB at Ref. plane 3. However, it should be noted that, in his method, the bias T—which usually includes capacitor and inductor—could change its properties along with the changing of temperature.

F. Rodriguez-Morales's group [22], [57], [60], [61] did calibration at the end of the bias T at the cryogenic temperature—right before the IF circuitry (Ref. plane 2). This calibration is done thanks to Open, Short, Load standards of the calibration kit after using three cooling cycles. Then, a model of the IF circuitry was built with the help of a 3D EM software. Finally, the de-embedded technique is used to obtain the impedance of HEB. In this case, the results depend strongly on the reliability and accuracy of the calibration standards, in particular at low temperature.

In [62], they did the calibration at the level of the HEB bridge (at Ref. plane 4), when they used HEB as the calibration standards. The calibration is done by using one-port three-term error model, which requires three measured reflection coefficients of 3 known standards (Open/Short/Load in this case) [63]–[65]. The Short and Load standards are achieved using the properties of the HEB at cryogenic temperature, without LO pump: HEB will work as a Short standard with zero bias voltage, as a Load standard with a high bias voltage. The Open standard, however, is achieved by destroying the HEB (by very high bias current) at the end of the measurement. The paper in [66] has the same idea, but they used an already dead HEB for the Open standard, and another HEB which has an impedance close to 50 Ω (47 Ω) as a Load standard. However, we did not adopt this method since we aimed to find a way that does not require destroying the HEB.

After considering different methods and possibilities, we decided to extract the impedance of the HEB mixer at the end of the microstrip (Ref. plane 3). To do it, we combine the measurements and simulations, using the

one-port three-term error model [63]–[65] and the 3D EM model of the IF circuitry of the HEB block.

4.3.2 One-port three-term error model

As shown in Figure 4-7, we want to get the HEB's impedance at the ending of the microstrip line (Ref. plane 3) while we only can do the measurements at the input of cryostat (Ref. plane 1). So to obtain the characteristics at plane 3, we need to remove the contribution of all components between plane 1 and plane 3. This can be done by different calibration/extraction process. For our reflection coefficient measurement, we have chosen the One-port three-term error model as illustrated by Figure 4-8. This model can be used to characterize the systematic errors between two planes, and mathematically remove these errors to give us the actual reflection coefficient at the DUT plane ($S_{11}(\omega)$) [67], [68].

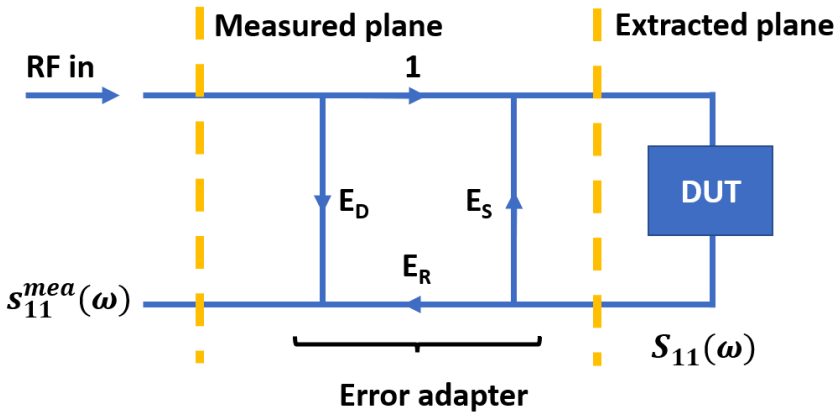

Figure 4-8. One-port three-term error model.

One-port error model contains three terms [63]–[65]:

- $E_D(\omega)$: Directivity error term caused by the incomplete separation of the incident signal from the reflected signal.
- $E_R(\omega)$: Reflection tracking term caused by the difference in the frequency response between the test and reference signal path.

- $E_S(\omega)$: Source match term caused by the mismatching between the source and the input of the DUT.

From 3 measured reflection coefficients $S_{11}^{meas}(\omega)$ (measured values which are denoted as M_1, M_2, M_3) of 3 known reflection coefficients of 3 standards $S_{11}(\omega)$ (actual values which are denoted as A1, A2, A3), we can resolve three error terms[64], [65]:

$$E_D(\omega) = \frac{M_1(M_2 - M_3)A_2A_3 + M_2(M_3 - M_1)A_3A_1 + M_3(M_1 - M_2)A_1A_2}{(M_1 - M_2)A_1A_2 + (M_2 - M_3)A_2A_3 + (M_3 - M_1)A_3A_1} \quad \textit{Equation 45}$$

$$E_R(\omega) = \frac{(M_1 - M_2)(M_2 - M_3)(M_3 - M_1)(A_1 - A_2)(A_2 - A_3)(A_3 - A_1)}{[(M_1 - M_2)A_1A_2 + (M_2 - M_3)A_2A_3 + (M_3 - M_1)A_3A_1]^2}$$

$$E_S(\omega) = \frac{M_1(A_2 - A_3) + M_2(A_3 - A_1) + M_3(A_1 - A_2)}{(M_1 - M_2)A_1A_2 + (M_2 - M_3)A_2A_3 + (M_3 - M_1)A_3A_1}$$

Three standards can be Open, Short, and Match as in a standard calibration kit in VNA or any three independent and known loads.

After having the three error terms, the actual reflection coefficient $S_{11}(\omega)$ can be de-embedded from the measured $S_{11}^{meas}(\omega)$:

$$S_{11}(\omega) = \frac{S_{11}^{meas}(\omega) - E_D(\omega)}{E_R(\omega) + E_S(\omega)[S_{11}^{meas}(\omega) - E_D(\omega)]} \quad \textit{Equation 46}$$

Finally, the value of the load impedance is calculated by Equation 47

$$Z_{Load} = Z_0 \frac{1 + S_{11}(\omega)}{1 - S_{11}(\omega)} \quad \textit{Equation 47}$$

with $Z_0 = 50\ \Omega$.

4.3.3 Calibration standards for the HEB block's measurement

Using three measurements with three known and independent standards (e.g., Short, Open, and Load), we can establish the one-port three-term model to remove the errors caused by the components from the input of the cryostat

to the end of the microstrip inside the mixer block. From that, we can obtain the actual impedance of the HEB mixer.

The wirebond connections in the case of three standards are shown in Figure 4-9. Open is made by removing the wires that connect the end of the microstrip line to the HEB chip, Short is created by connecting the end of the microstrip line to the ground, and Load is done by connecting microstrip line to the HEB by wirebond.

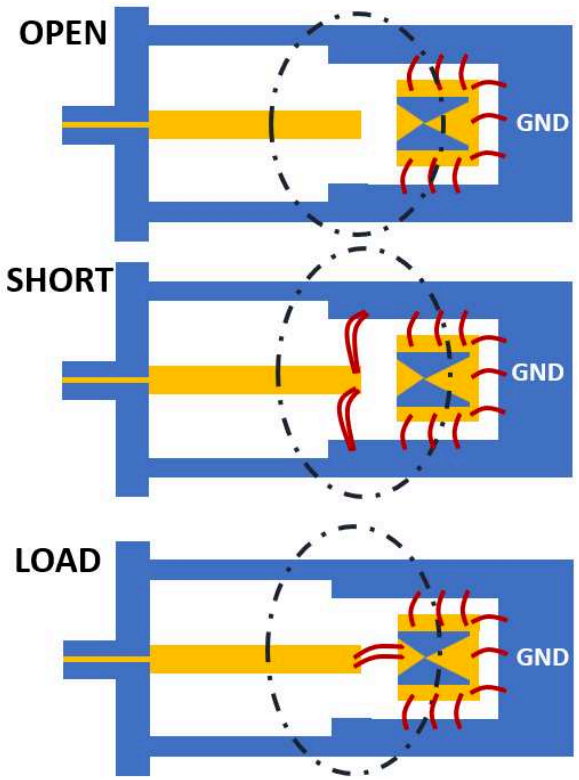

Figure 4-9. Wirebond connections in case of three standards.

To extract the impedance of the DUT using one-port three-term error model in section 4.3.2, several studies in [64], [66] set the values of reflection coefficients of the standards as ideal values (e.g. $A_{Open} = 1, A_{Short} = -1$). We did several tests at room temperature and realized that it was not exact since S11 of Open and Short can vary along with the frequency. Thus, the reflection coefficients Open and Short are extracted, by combining measurements at room temperature

and IF circuitry simulation. Open and Short are measured at the SMA of the HEB block. The 2-port S-parameter file from the SMA to the end of the microstrip is obtained by the simulation of the 3D IF circuitry model shown in Figure 4-6b. A software [69] is used to mathematically remove the parts from the SMA to the end of the microstrip from the measurements results, to obtain the reflection coefficients of Open and Short references. These extracted Open and Short parameters will be used for the HEB's impedance measurement.

The reflection coefficient of the Load standard is obtained by the measurement of the HEB at cryogenic temperature. HEB is considered as a pure resistance at high bias voltage (~10 mV), with no LO pump. The reflection coefficient of the Load can be calculated by

$$A_{Load} = \frac{Z_{Load} - Z_0}{Z_{Load} + Z_0} \qquad \textit{Equation 48}$$

where Z_0 equals to 50 Ω, is the characteristic impedance of the testing instruments.

To perform three measurements for deducing HEB's impedance from one-port three-term error model, we need three cooling down cycles with different configurations of the HEB mixer block as shown in Figure 4-9. The HEB block is mounted inside the cryostat and cooled down to around 4 K. The reflection coefficients are measured at the input of the cryostat. Three error terms ($E_D(\omega)$, $E_R(\omega)$, $E_S(\omega)$) are then deduced using Equation 45 and they will be used to extract the HEB's IF impedance under its working conditions.

4.3.4 Measurement and extraction results

This section presents the testbench used to measure HEB's reflection coefficients and the measurement results.

4.3.4.1 Experimental setup

HEB block needs to be cooled down to the temperature below the critical temperature to bring it to the mixing condition. We use a cooling system with pulse tube technology, which has very low vibration compared to piston technology [70].

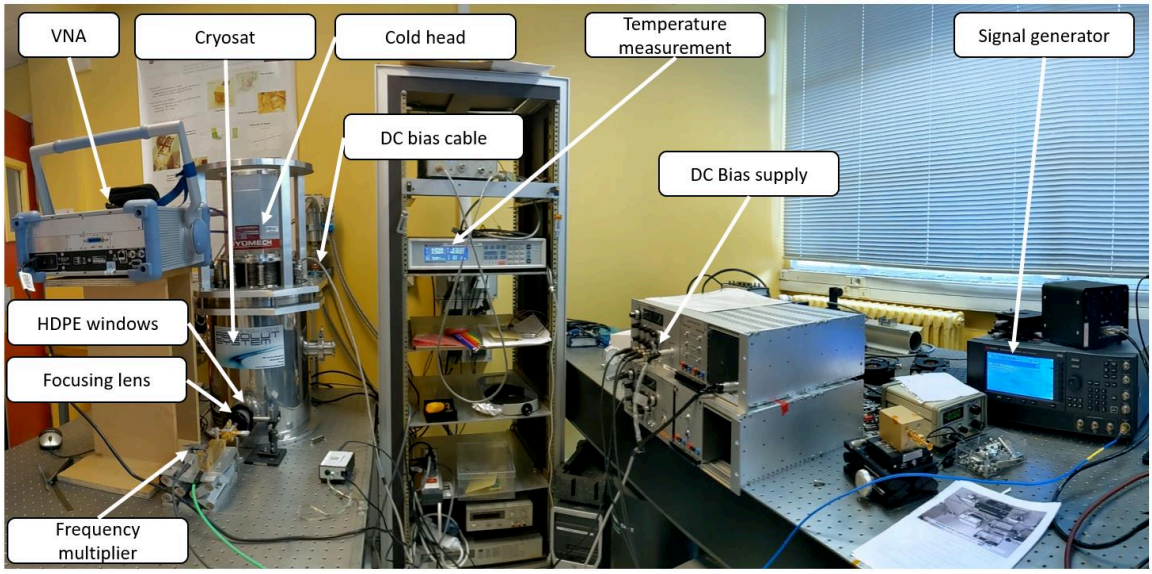

(a)

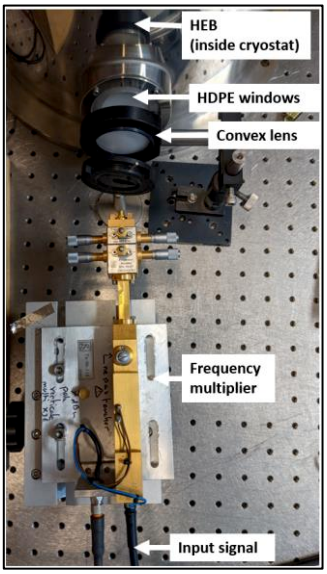

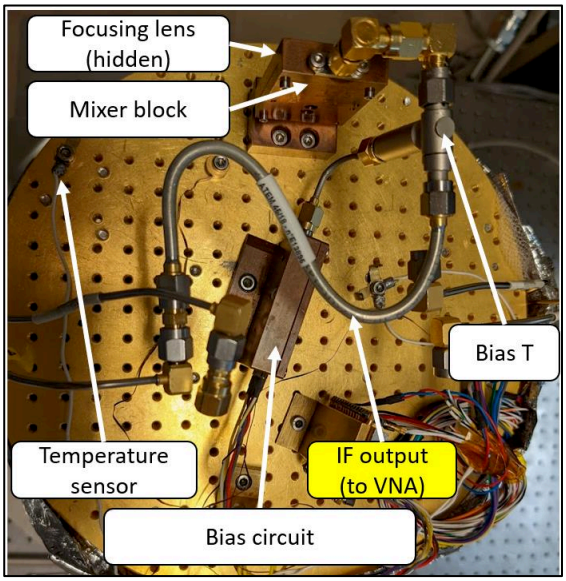

(b) (c)

Figure 4-10. a) Testbench to measure the HEB's IF reflection coefficient.

b) Zoom-in to the input part to inject a LO signal. c) Components mounted on the cold plate inside the cryostat.

The setup is shown in Figure 4-10. This experiment was conducted in the case HEB mixer is pumped by a LO source and biased by a DC voltage. The

signal generator generates a signal at 16-18 GHz which is multiplied up to around 600 GHz thanks to the frequency multipliers. This signal is then focused by a convex lens and passes through the high-density polyethylene (HDPE) window (as shown in Figure 4-10b), going inside the cryostat. The LO ray reaches the HEB thanks to the Si lens mounted on the mixer block. This signal is then absorbed by the HEB at a power level of a few hundred nW. The HEB is biased by a DC bias supply through a bias circuit inside the cryostat. The HEB mixer, under the effect of LO signal and DC bias, is brought to its mixing state. A microwave power provided by a VNA [71] is injected into HEB, and the reflected coefficient of the HEB is measured. A computer is used to record the I-V curve.

HEB is a very sensitive device. A small change of input power can affect its superconducting state and change the I-V characteristic. So, the VNA power must be small enough to be able to measure the reflection coefficient of the HEB without affecting its working condition, but also big enough to avoid a too much noisy measurement. After doing several tests, the power is set to -55 dBm (around 3 nW). 64 averaged measurements are applied to increase the signal-to-noise ratio.

4.3.4.2 Measurement and extraction results

The measured I-V characteristics at different LO pumping levels are shown in Figure 4-11.

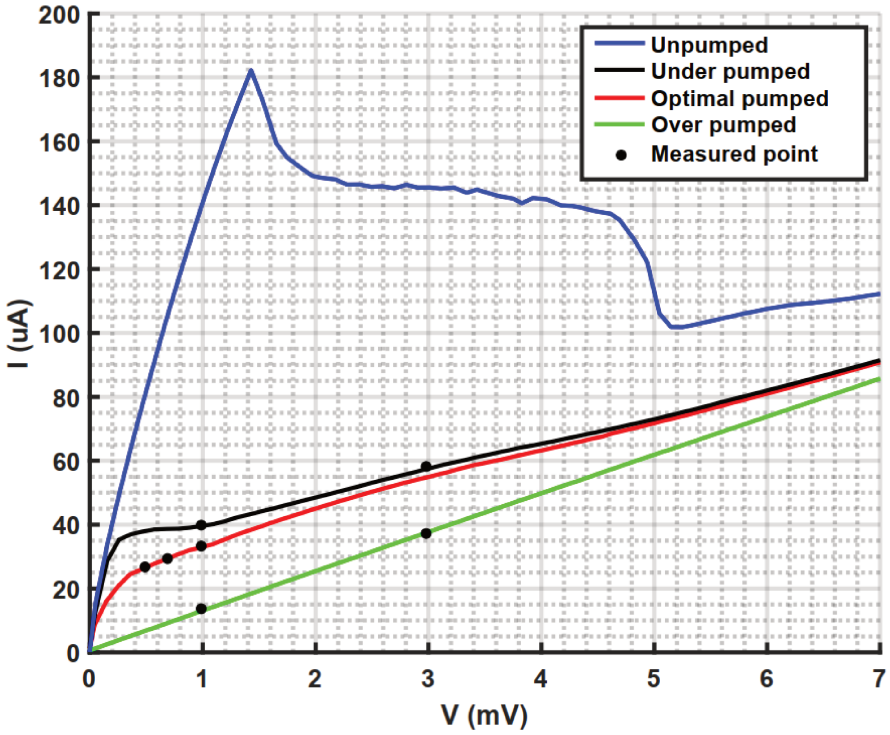

Figure 4-11. I-V curves of the HEB at different LO pumping levels. Black circles show the points where we measured the HEB's reflection coefficients.

The recorded I-V curves correspond to four states of the mixer depending on the LO pumping level: Unpumped, Under pumped, Optimally pumped, and Over pumped. Black circles show the points where we measured the HEB's reflection coefficients.

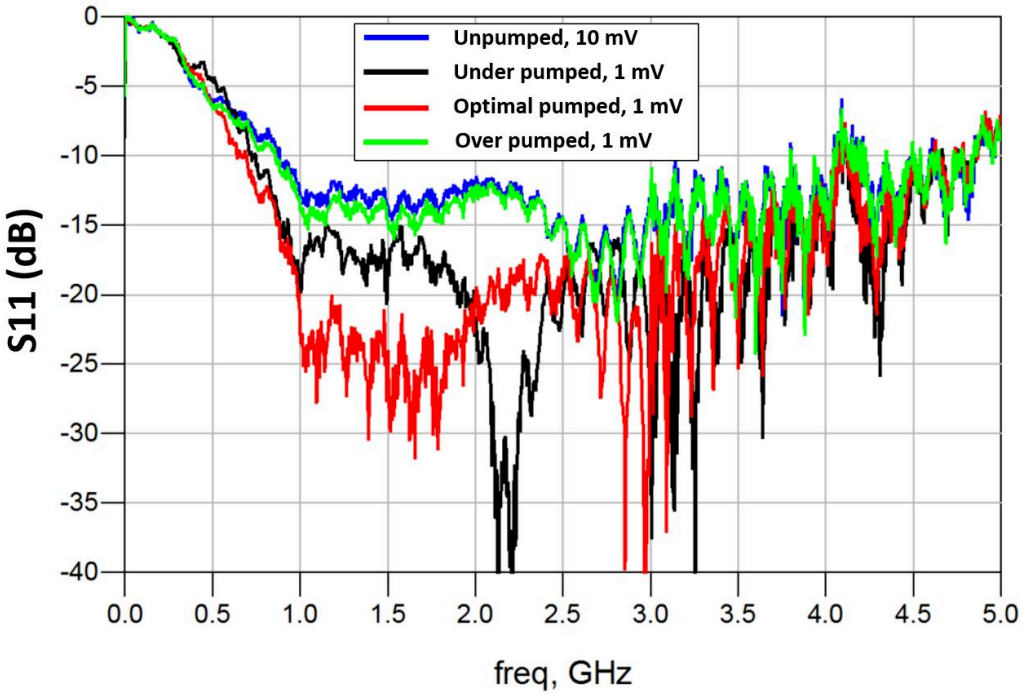

Figure 4-12. Measured reflection coefficients of the HEB block (calibrated at the input of the cryostat) at different bias voltages and LO pumping levels.

Figure 4-12 shows the magnitude of the reflection coefficients (S11) at different pumping levels measured at the input of the cryostat (Ref. plane 1 in Figure 4-7). Actually, the very high DC bias (e.g. 10 mV) in case of unpumped can saturate HEB in the same way as the over pumped level, according to the NSGR model presented in section 2.4.1. Thus, these two S11s in Figure 4-12 almost overlap. In both cases, HEB can be considered as a pure resistor with constant values over the frequency range. We use its DC resistance value at this frequency range as Load standard (e.g. 81.3 Ohms at unpumped LO and 10 mV DC bias).

From these measured data, we extracted the impedance of the HEB at the ending of the microstrip line (Ref. plane 3 in Figure 4-7) by using the one-port three-term model presented in section 4.3.2. The reflection coefficients of the HEB at the ending of the microstrip line is extracted by applying Equation 46, and its impedance is calculated using Equation 47.

Figure 4-13 to Figure 4-15 show the extracted reflection coefficients and impedances of the HEB mixer at different pumping levels and biases.

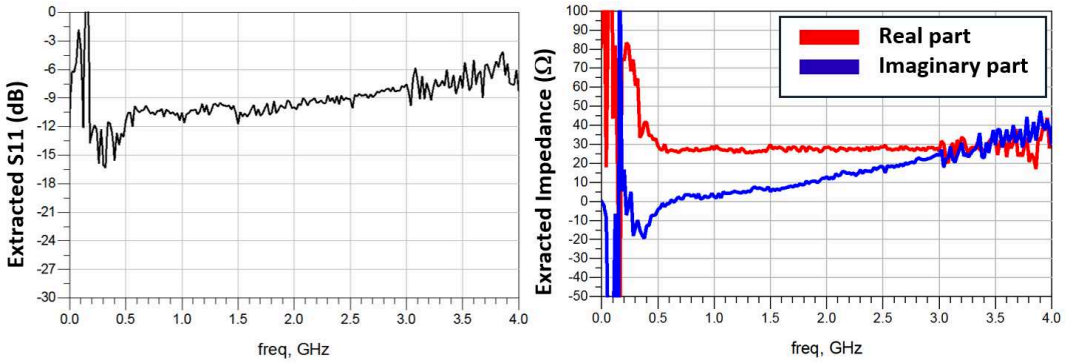

(a) (b)

Figure 4-13. Extracted S11 (a) and impedance (b) of the HEB at the ending of microstrip line, at optimal pumped level and 0.5 mV DC bias.

Figure 4-13 illustrates the extracted mixer's reflection coefficient and impedance with an optimal LO pumping level and a bias voltage of 0.5 mV. The real part impedance reaches the highest value of 85 Ω at a frequency around 0.25 GHz. Then it decreases quickly to about 28 Ω at 0.5 GHz, and keeps almost constant (with a small fluctuation) up to 3.5 GHz. Meanwhile, the imaginary part has its minimum value of around - 20 Ω at 0.4 GHz. After that, the imaginary part increases from - 20 Ω to around 0 Ω at the frequency range 0.4 – 0.5 GHz, and then linearly rises from 0 Ω to around 40 Ω when the frequency increases from 1 GHz to 4 GHz.

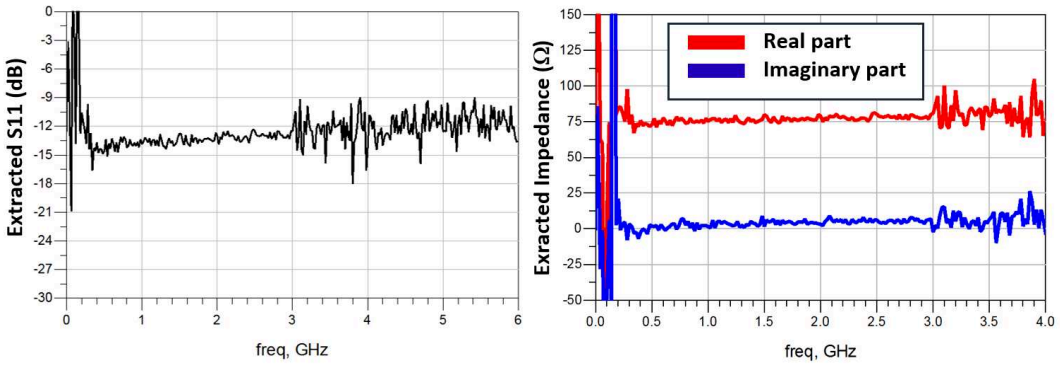

(a) (b)

Figure 4-14. Extracted S11 (a) and impedance (b) of the HEB at the end of the microstrip line, at over pumped level and 3 mV DC bias.

Figure 4-14 gives extracted mixer's reflection coefficient and impedance in case of over pumped, 3 mV. The real part is around 80 Ω, while the imaginary part is around 0 Ω over the frequency range from 0.5 GHz to 3.5 GHz. HEB, in this case, works similar to a pure resistor as we expected.

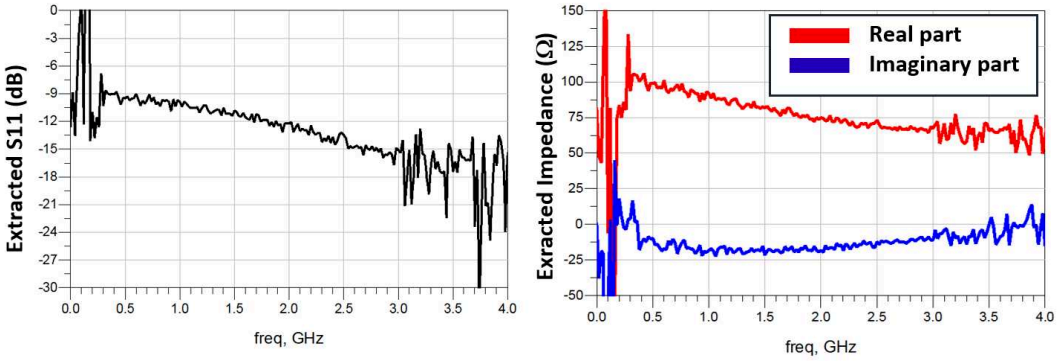

(a) (b)

Figure 4-15. Extracted S11 (a) and impedance (b) of the HEB at the end of the microstrip line, at under pumped level and 3 mV DC bias.

Figure 4-15 shows extracted mixer's reflection coefficient and impedance at the under pumped level (between unpumped and optimally pumped).

At this level, impedance of the HEB is no longer constant, but varies over the frequency range.

The extracted impedances of the HEB have been fitted with the calculated one using NSGR model in section 2.4.1. Here I show a case of under pumped level in Figure 4-16. This extracted impedance shows good agreements with the calculated one, in both terms of real and imaginary parts. Indeed, two real parts in Figure 4-16a almost overlap from 0.3 GHz to 4 GHz. In Figure 4-16b, the extracted imaginary part also follows the calculated curve over the frequency range (0.3 – 2 GHz), with a little difference at a higher frequency (from 2.5 GHz).

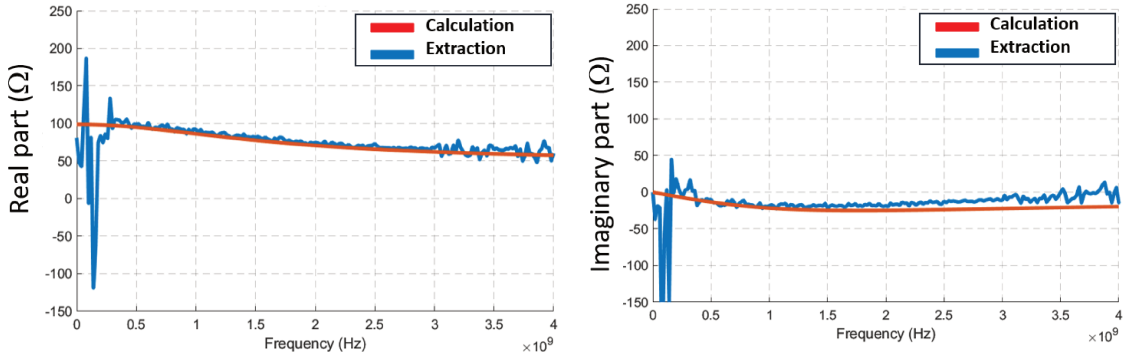

(a) (b)

Figure 4-16. Extracted vs calculated impedance of the HEB mixer in case of Underpump, 3 mV bias. a) Real parts. b) Imaginary parts

Chapter 5. Conclusion and perspectives

This thesis project is part of the development of THz heterodyne array receivers undertaken at LERMA. The work during this thesis has been focused on two main aspects:

(1) LO feeding system for a 2 x 2 receiver array working at 1.3 THz.

(2) IF impedance of the HEB mixer under its working conditions.

The LO feeding system is based on a reflective phase grating according to the concept of Global Phase Grating developed at LERMA. The system is designed to split efficiently the LO source into four beams and then focus them on four pixels of a mixer array.

The basic element of this system is the phase grating of which the surface geometry is created by a specific calculation code. I have modelled and simulated the whole system including a phase grating, a THz source antenna and a focusing mirror with the help of the full wave electromagnetic solver FEKO. Different parameters of the designed system have been analyzed and their influences on the beam propagation have been simulated. In particular, we have simulated the influence of the grating's size and profile type on the efficiency of the beam division. We found that we can reduce the grating's size and replace the initial continuous profile by discretisized one without decreasing significantly the efficiency. This result has allowed us to adopt a faster and easier way for the manufacturing. We have also simulated the effects of the changing of incident angle and of grating's rotation on the output beam patterns.

The manufactured phase grating prototype was mounted in the quasi-optical system and the beam pattern measurement has been performed at

different locations of the system. The 1.3 THz signal is provided by an amplifier multiplier chain. At the beginning of the measurement, we got systematically an unwanted output beam located in the centre of four expected beams. The 3D electromagnetic simulation revealed the possible reason due to reflections of the edge area of the fabricated phase grating. This was confirmed by the experiment. The unwanted output beam was suppressed by using a THz absorber on the phase grating.

The measured result shows a good agreement with the simulated one. The four output beams follow the Gaussian distribution and each beam contains between 17.5-19 % of the input power, indicating a good homogeneity. The measured global efficiency (calculated as the ratio of the total power of four output beams on the power of the input beam) is 72 % which is relatively close to the simulated one (78 %). The measured average distance between two adjacent pixels is 16.8 mm which is also close to the simulated one (16.5 mm). The average radius of 4 pixels in measurement is 4.2 mm, which is comparable with the simulated result (4.4 mm) if we consider the effect of the 6 mm diameter of Winston horn in the simulation.

After performing the simulation and the measurement, I worked on the existing homemade calculation code to create the geometry of Global phase grating. A graphical interface and an additional function have been introduced to allow a greater number of pixels and arbitrary distances of 2 adjacent pixels. With the new version of the calculation code, phase gratings with 9 and 16 pixels at 1.3 THz have been designed.

The second part of my thesis is dedicated to the investigation of superconducting HEB mixer's IF impedance of which the knowledge can help to better understand HEB mixer's working principle.

HEB is a very sensitive device, it is challenging to characterize its IF impedance when it is biased and under LO radiation. I followed a specific procedure for measuring and extracting the HEB's IF impedance, by combining measurement and 3D EM simulation, using one-port three-term error model.

First, we have worked with a testblock which is very similar to the actual HEB block. This block is measured and modelled at room temperature. The measured and simulated result shows a good agreement. This experiment helped us to create a reliable 3D EM model of the HEB mixer block. Then the impedance of the HEB mixer at different LO levels and DC bias at cryogenic temperature is extracted using one-port three-term error model.

With the known HEB mixer IF impedance and that of the LNA, we can make a matching circuit between HEB and LNA in order to extract the IF output power with minimum loss and maximum bandwidth. Knowing the HEB's impedance can also help the amplifier's design.

The next objective will be integrating the LO feeding system and the IF matching circuit to build a compact 2 x 2 receiver array.

REFERENCES

[1] P. H. Siegel, “Terahertz Technology,” *IEEE Trans Microw Theory Tech*, vol. 50, no. 3, pp. 910–928, 2002, doi: 10.1109/22.989974.

[2] B. K. Tan, *Development of Coherent Detector Technologies for Sub-Millimetre Wave Astronomy Observations*. Springer, 2016. doi: 10.1007/978-3-319-19363-2.

[3] J. R. Tucker and M. J. Feldman, “Quantum detection at millimeter wavelengths,” *Rev Mod Phys*, vol. 57, no. 4, pp. 1055–1113, 1985, doi: 10.1103/RevModPhys.57.1055.

[4] K. I. Rudakov *et al.*, “THz range low-noise sis receivers for space and ground-based radio astronomy,” *Applied Sciences (Switzerland)*, vol. 11, no. 21, 2021, doi: 10.3390/app112110087.

[5] J. Faist, F. Capasso, D. L. Sivco, C. Sirtori, A. L. Hutchinson, and A. Y. Cho, “Quantum cascade laser,” *Science (1979)*, vol. 264, no. 5158, pp. 553–556, 1994, doi: 10.1126/science.264.5158.553.

[6] B. Wen and D. Ban, “High-temperature terahertz quantum cascade lasers,” *Prog Quantum Electron*, vol. 80, Nov. 2021, doi: 10.1016/J.PQUANTELEC.2021.100363.

[7] U. U. Graf, C. E. Honingh, K. Jacobs, and J. Stutzki, “Terahertz Heterodyne Array Receivers for Astronomy,” *J Infrared Millim Terahertz Waves*, vol. 36, no. 10, pp. 896–921, 2015, doi: 10.1007/s10762-015-0171-7.

[8] C. Groppi *et al.*, “SuperCam, a 64-pixel heterodyne imaging array for the 870 micron atmospheric window,” in *Astronomical Telescopes + Instrumentation*, 2006, vol. 1157. doi: 10.1109/MWSYM.2015.7166873.

[9] C. Kasemann *et al.*, “CHAMP + : a powerful array receiver for APEX,” *Millimeter and Submillimeter Detectors and Instrumentation for Astronomy III*, no. July, 2006, doi: 10.1117/12.670810.

[10] C. Risacher *et al.*, “The upGREAT Dual Frequency Heterodyne Arrays for SOFIA,” *Journal of Astronomical Instrumentation*, vol. 7, no. 4, pp. 1–16, 2018, doi: 10.1142/S2251171718400147.

[11] C. Risacher *et al.*, “The upGREAT 1.9 THz multi-pixel high resolution spectrometer for the SOFIA Observatory,” *Astron Astrophys*, vol. 595, pp. 1–7, 2016, doi: 10.1051/0004-6361/201629045.

[12] C. Walker *et al.*, “The Stratospheric THz Observatory (STO),” *Ground-based and Airborne Telescopes III*, vol. 7733, p. 77330N, 2010, doi: 10.1117/12.857765.

[13] M. Neric *et al.*, “IF system design for the Galactic/Extragalactic ULDB Spectroscopic Terahertz Observatory (GUSTO),” no. August 2018, p. 101, 2018, doi: 10.1117/12.2314096.

[14] W. F. M. Ganzevles, “A Quasi-Optical THz Mixer Based on a Nb Diffusion-Cooled Hot-Electron Bolometer,” 2002.

[15] A. D. Semenov, G. N. Gol’tsman, and R. Sobolewski, “Hot-electron effect in superconductors and its applications for radiation sensors,” *Supercond Sci Technol*, vol. 15, no. 4, pp. R1–R16, Mar. 2002, doi: 10.1088/0953-2048/15/4/201.

[16] M. Wei, “Investigation of Hot Electron Bolometer Mixers for Submillimeter Multi-pixel Receiver Applications,” 2010. Accessed: Jun. 05, 2022. [Online]. Available: http://www.theses.fr/2010PA066077

[17] H. Ekstrom, B. S. Karasik, E. L. Kollberg, and K. S. Yngvesson, “Conversion Gain and Noise of Niobium Superconducting Hot-

Electron-Mixers," *IEEE Trans Microw Theory Tech*, vol. 43, no. 4, pp. 938–947, 1995, doi: 10.1109/22.375258.

[18] D. E. Prober, "Superconducting terahertz mixer using a transition-edge microbolometer," *Appl Phys Lett*, vol. 62, no. 17, pp. 2119–2121, 1993, doi: 10.1063/1.109445.

[19] P. J. Burke, "High Frequency Electron Dynamics in Thin Film Superconductors and Applications to Fast, Sensitive THz Detectors," 1998.

[20] R. Nebosis, A. D. Semenov, Yu. P. Gousev, and K. F. Renk, "Rigorous Analysis of a Superconducting Hot-Electron Bolometer Mixer: Theory and Comparison with Experiment," *Softwaretechnik-trends*, p. 601, 1996.

[21] D. W. Floet, "Hotspot Mixing in THz Niobium superconducting hot electron bolometer mixers," Delft University of Technology, the Netherlands, 2001.

[22] F. Rodriguez-Morales, K. S. Yngvesson, and D. Gu, "Wideband IF-integrated terahertz HEB Mixers: Modeling and characterization," *IEEE Trans Microw Theory Tech*, vol. 58, no. 5 PART 1, pp. 1140–1150, May 2010, doi: 10.1109/TMTT.2010.2045566.

[23] F. Arams, C. Allen, B. Peyton, and E. Sard, "Millimeter mixing and detection in bulk InSb," *Proceedings of the IEEE*, vol. 54, no. 4, pp. 612–622, 1966, doi: 10.1109/PROC.1966.4781.

[24] E. M. Gershenzon *et al.*, "Millimeter and submillimeter range mixer based on electronic heating of superconducting films in the resistive state," *Sov. Phys. Superconductivity*, pp. 1582–1597, 1990.

[25] J. W. Kooi *et al.*, “IF Impedance and Mixer Gain of Hot-Electron Bolometers,” *J Appl Phys*, vol. 101, no. 4, 2007, doi: https://doi.org/10.1063/1.2400086.

[26] J. W. Kooi, J. J. A. Baselmans, J. R. Gao, P. Dieleman, and Z. Q. Yang, “IF Impedance and Mixer Gain of Phonon Cooled Hot-Electron Bolometers and the Perrin-Vanneste Two Temperature Model,” *16th International Symposium on Space Terahertz Technology, ISSTT 2005*, pp. 465–473, May 2005.

[27] A. I. Elant’ev and B. S. Karasik, “Effect of high frequency current on Nb superconductive film in the resistive state,” *Sov. J. Low Temp. Physics*, vol. 15, pp. 379–383, 1989.

[28] A. D. Semenov, R. S. Nebosis, M. A. Heusinger, and K. F. Renk, “Two-temperature model of nonequilibrium photoresponse of superconducting films to pulsed radiation,” *Physica C: Superconductivity and its applications*, vol. 235–240, no. PART 3, pp. 1971–1972, 1994, doi: 10.1016/0921-4534(94)92207-1.

[29] J. W. Kooi *et al.*, “IF impedance and mixer gain of hot electron bolometers,” *J Appl Phys*, vol. 101, no. 4, p. 44511, 2007, doi: 10.1063/1.2400086.

[30] H. F. Merkel, P. Khosropanah, S. Member, D. W. Floet, P. A. Yagoubov, and E. L. Kollberg, “Conversion Gain and Fluctuation Noise of Phonon-Cooled Hot-Electron Bolometers in Hot-Spot Regime,” *IEEE Trans Microw Theory Tech*, vol. 48, no. 4, pp. 690–699, 2000, doi: 10.1109/22.841961.

[31] M. Hajenius *et al.*, “Full characterization and analysis of a terahertz heterodyne receiver based on a NbN hot electron bolometer,” *J Appl Phys*, vol. 100, no. 7, 2006, doi: 10.1063/1.2354421.

[32] P. K. J.Baubert, H. Merkel, M.Salezl, “A hot-spot model for membrane-based HEB mixer,” *14th International Symposium on Space Terahertz Technology, ISSTT 2003*, pp. 393–404, 2003.

[33] J. Baubert, “Superconducting Hot Electron Bolometers on thin membranes for SHAHIRA,” l’Universite Paris 6, 2005.

[34] S. Cherednichenko, P. Yagoubov, K. Il’in, G. Gol, G. Gol’tsman, and E. Gershenzon, “Large bandwidth of NbN phonon-cooled hot-electron bolometer mixers on sapphire substrates,” *8th International Symposium on Space Terahertz Technology, ISSTT 1997*, pp. 245–257, 1997, doi: 10.1109/EUMA.1997.337922.

[35] S. Heyminck, U. U. Graf, R. Güsten, J. Stutzki, H. W. Hübers, and P. Hartogh, “GREAT: The SOFIA high-frequency heterodyne instrument,” *Astron Astrophys*, vol. 542, pp. 1–7, 2012, doi: 10.1051/0004-6361/201218811.

[36] B. Mirzaei *et al.*, “Prototype 4.7 THz array local oscillator for GUSTO,” *29th IEEE International Symposium on Space Terahertz Technology, ISSTT 2018*, pp. 28–33, 2018.

[37] F. Defrance *et al.*, “Structured Surface Design to Generate Any Beam Pattern at THz Frequencies,” *Conference EuCAP 2017*.

[38] F. Defrance *et al.*, “Structured surface reflector design for oblique incidence beam splitter at 610 GHz,” *Opt Express*, vol. 24, no. 18, pp. 20335–20345, 2016, doi: 10.1364/oe.24.020335.

[39] 2013. [Online]. Available: http://vadiodes.com/, “Virginia Diodes homepage”.

[40] A. FEKO, “1820 E Big Beaver Rd, Troy, Michigan, 48083, United States”.

[41] P. F. Goldsmith, “Quasi-Optical Techniques,” *Proceedings of the IEEE*, vol. 80, no. 11, pp. 1729–1747, 1992, doi: 10.1109/5.175252.

[42] G. S. Curran and J. A. Murphy, “An Introduction to the Quasi-Optical Design of the HIFI Instrument for the Herschel Space Observatory,” *The ITB Journal*, vol. 6, no. 1, 2005, doi: 10.21427/D7X45V.

[43] P. F. Goldsmith, *Quasioptical systems: Gaussian beam quasioptical propagation and applications*, Wiley-IEEE Press. 1998. Accessed: Jul. 04, 2022. [Online]. Available: https://ieeexplore.ieee.org/servlet/opac?bknumber=5264471

[44] R. Voelkel, “Diffractive optics,” *Advanced Optical Technologies*, vol. 10, no. 1, pp. 17–18, 2021, doi: https://doi.org/10.1515/aot-2021-0007.

[45] J. E. Harvey and R. N. Pfisterer, “Understanding diffraction grating behavior: including conical diffraction and Rayleigh anomalies from transmission gratings,” *Optical Engineering*, vol. 58, no. 08, p. 1, 2019, doi: 10.1117/1.oe.58.8.087105.

[46] H. Dammann and K. Görtler, “High-efficiency in-line multiple imaging by means of multiple phase holograms,” *Opt Commun*, vol. 3, no. 5, pp. 312–315, Jul. 1971, doi: 10.1016/0030-4018(71)90095-2.

[47] H. Dammann and E. Klotz, “Coherent optical generation and inspection of two-dimensional periodic structures,” *Opt Acta (Lond)*, vol. 24, no. 4, pp. 505–515, 1977, doi: 10.1080/713819570.

[48] J. Jahns, M. M. Downs, M. E. Prise, N. Streibi, and S. J. Walker, “Dammann gratings for laser beam shaping,” *Optical Engineering*, vol. 28, no. 12, pp. 1267–1275, 1989, doi: https://doi.org/10.1117/12.7977142.

[49] U. U. Graf and S. Heyminck, “Fourier gratings as submillimeter beam splitters,” *IEEE Trans Antennas Propag*, vol. 49, no. 4, pp. 542–546, 2001, doi: 10.1109/8.923313.

[50] Altair FEKO, “FEKO User Manual”, [Online]. Available: https://www.altairuniversity.com/wp-content/uploads/2015/03/UserManual.pdf

[51] QMC instruments, “QMC detector.” http://www.terahertz.co.uk/index.php?option=com_content&view=article&id=236&Itemid=530 (accessed Apr. 22, 2021).

[52] QMC instruments, “Winston cones.” http://www.qmcinstruments.co.uk/winston-cones (accessed Aug. 26, 2022).

[53] J. R. Silva, B. Mirzaei, Y. C. Luo, D. J. Hayton, J. R. Gao, and C. Groppi, “Demonstration and Stabilization of a 2x4 HEB Array Receiver at 1.4 THz Based on a Fourier Phase Grating Local Oscillator,” *28th International Symposium on Space Terahertz Technology, ISSTT 2017*, 2017.

[54] B. Mirzaei *et al.*, “Efficiency of multi-beam Fourier phase gratings at 1.4 THz,” *Opt. Express*, vol. 25, no. 6, pp. 6581–6588, Mar. 2017, doi: 10.1364/OE.25.006581.

[55] F. Defrance, “Instrumentation of a 2 . 6 THz heterodyne receiver,” Instrumentation and Methods for Astrophysic [astro-ph.IM]. Université Pierre et Marie Curie - Paris VI, 2016.

[56] R. D. Higgins and J. W. Kooi, “Electrical standing waves in the HIFI HEB mixer amplifier chain,” in *Terahertz Technology and Applications II*, Feb. 2009, vol. 7215, p. 72150L. doi: 10.1117/12.811127.

[57] F. Rodriguez-Morales and K. S. Yngvesson, “Impedance and Bandwidth Characterization of NbN Hot Electron Bolometric Mixers,” *14th International Symposium on Space Terahertz Technology, ISSTT 2003*, 2003.

[58] Roger, “RT/Duroid 6010LM.” https://rogerscorp.com/-/media/project/rogerscorp/documents/advanced-electronics-solutions/english/data-sheets/rt-duroid-6006-6010lm-laminate-data-sheet.pdf

[59] V. Beyschlag, “Resistors in Microwave Applications,” *Application note*, 2013, Accessed: Jul. 04, 2022. [Online]. Available: https://www.vishay.com/docs/28871/resistorsmicrowaveapp.pdf

[60] F. Rodriguez-Morales *et al.*, “Optimal Coupling of NbN HEB THz Mixers to Cryogenic HEMT IF Low-Noise Amplifiers,” *17th International Symposium on Space Terahertz Technology, ISSTT 2006*, 2006.

[61] F. Rodriguez-Morales *et al.*, “Highly Packaged HEB Receivers Using Three-Dimensional Integration,” *18th International Symposium on Space Terahertz Technology, ISSTT 2007*, 2007, [Online]. Available: https://www.researchgate.net/publication/254400936

[62] D. Meledin *et al.*, “Study of the IF bandwidth of NbN HEB mixers based on crystalline quartz substrate with an MgO buffer layer,” *IEEE Transactions on Applied Superconductivity*, vol. 13, no. 2, pp. 164–167, Jun. 2003, doi: 10.1109/TASC.2003.813671.

[63] A. Technologies, “De-embedding and Embedding S-Parameter Networks Using a Vector Network Analyzer,” *Agilent*, pp. 1–24, 2008.

[64] M. Scheffler and M. Dressel, “Broadband microwave spectroscopy in Corbino geometry for temperatures down to 1.7 K,” *Review of Scientific Instruments*, vol. 76, no. 7, 2005, doi: 10.1063/1.1947881.

[65] H. Kitano, T. Ohashi, and A. Maeda, “Broadband method for precise microwave spectroscopy of superconducting thin films near the critical temperature,” *Review of Scientific Instruments*, vol. 79, no. 7, 2008, doi: 10.1063/1.2954957.

[66] S. Bevilacqua, E. Novoselov, S. Cherednichenko, H. Shibata, and Y. Tokura, “Wideband MgB2 Hot-Electron Bolometer Mixers: IF Impedance Characterisation and Modeling,” *IEEE Transactions on Applied Superconductivity*, vol. 26, no. 3, pp. 1–5, Apr. 2016, doi: 10.1109/TASC.2016.2537746.

[67] R. F. Bauer and P. Penfield, “De-Embedding and Unterminating,” *IEEE Trans Microw Theory Tech*, vol. 22, no. 3, pp. 282–288, 1974, doi: 10.1109/TMTT.1974.1128212.

[68] D. M. Pozar, *Microwave engineering*. Fourth edition. Hoboken, NJ : Wiley, [2012] ©2012, 2012. [Online]. Available: https://search.library.wisc.edu/catalog/9910153599402121

[69] P. A. D. S. (ADS), “PathWave Advanced Design System (ADS),” *1400 Fountaingrove Parkway Santa Rosa, CA 95403-1738*.

[70] Cryocoolers cryomech PT405, “https://www.cryomech.com/products/pt405/”.

[71] R. & S. Z. 13, “https://www.rohde-schwarz.com/”.

CONFERENCE

1. **H. D. Do**, G. Gay, Y. Delorme, “Development of a 2 x 2 reflective phase grating beam divider for heterodyne array receiver at 1.3 THz,” *URSI AT-AP-RASC 2022*, Spain, June 2022.

RÉSUMÉ

Les fréquences THz contiennent beaucoup d'informations utiles pour révéler la formation de la galaxie et l'évolution des étoiles. Pour détecter le spectre avec une sensibilité élevée et une très haute résolution, nous devons utiliser un récepteur hétérodyne. Pour les fréquences supérieures à 1 THz, le mélangeur à bolomètre à électrons chauds (HEB) est le meilleur candidat car il a la sensibilité la plus élevée parmi d'autres types de mélangeurs et théoriquement aucune limite de fréquence supérieure. L'une des demandes urgentes pour les futurs télescopes nécessitant des mélangeurs HEB est la construction de réseaux de récepteurs dans le but d'améliorer la cohérence des données acquises et d'augmenter la vitesse de cartographie. Il n'y a actuellement que quelques réseaux de récepteurs avec un petit nombre de pixels fonctionnant au-dessus de 1 THz. Ainsi, cela nécessite encore beaucoup d'investigation.

Cette thèse se concentre sur deux aspects principaux. Le premier consiste à étudier l'élément de distribution de l'oscillateur local (OL) pour le réseau de mélangeurs en utilisant un réseau de phase global. Le deuxième est de caractériser l'impédance en fréquence intermédiaire (FI) du mélangeur HEB dans ses conditions de travail.

Le premier aspect vise à trouver un moyen efficace de diviser un faisceau OL à quatre faisceaux secondaires pour alimenter une matrice de mélangeur à 1,3 THz. J'ai d'abord simulé et mesuré un diviseur à quatre faisceaux, puis analysé ces données et conclu les travaux de conception. La simulation et la mesure montrent un bon accord.

Le deuxième aspect vise à mieux comprendre le mécanisme physique du HEB afin de préparer l'intégration du circuit FI pour la construction du réseau de mélangeurs. Ce travail est réalisé par la combinaison de mesure et de simulation électromagnétique tridimensionnelle du bloc HEB. J'ai extrait l'impédance FI du mélangeur HEB à différents points de polarisation et différents niveaux de pompage OL à température cryogénique.

MOTS CLÉS

THz, mélangeur HEB, réseau de récepteur hétérodyne, réseau de phase, impédance FI

ABSTRACT

THz frequencies contain a lot of helpful information to reveal the formation of the galaxy and the evolution of the stars. To detect the spectral with high sensitivity and very high resolution, we need to use a heterodyne receiver. For the frequencies above 1 THz, the hot-electron-bolometer (HEB) mixer is the best candidate since it has the highest sensitivity among other kinds of mixers and theoretically no upper-frequency limit. One of the urgent demands for future telescopes requiring HEB mixers is building array receivers with the aim of improving the consistency of acquired data and increasing the mapping speed. There are currently only a few receiver arrays with a small number of pixels working above 1 THz. Thus, it still requires a lot of investigation.

This thesis focuses on two main aspects. The first is to investigate the local oscillator (LO) distribution element for the receiver array using the global phase grating. The second is to study the intermediate frequency (IF) impedance of the HEB mixer under its working conditions.

The first aspect aims to find an efficient way to divide the one single beam of the LO source to four sub-beams to feed a mixer array at 1.3 THz. I first simulated and measured a four-beam phase grating, then analyzed these data and concluded the design work. The simulation and measurement show a good agreement.

The second aspect aims to better understand the physical mechanism of the HEB and to prepare the integration of the IF circuit for the miniaturization of the current receiver. This work is done by the combination between measurements and three-dimensional electromagnetic simulation of the HEB block. I extracted the IF impedance of the HEB mixer at different bias points and local oscillator pumping levels at cryogenic temperature.

KEYWORDS

THz, HEB mixer, heterodyne array receivers, phase grating, IF impedance.